NUMERICAL MODELING AND EXPERIMENTAL ANALYSIS OF RESIDUAL STRESSES AND MICROSTRUCTURAL DEVELOPMENT DURING LASER-BASED MANUFACTURING PROCESSES

by
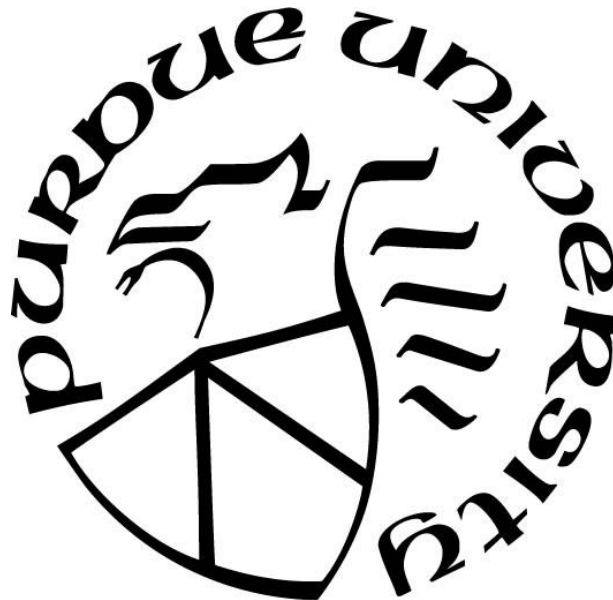
Neil S. Bailey

A Dissertation

Submitted to the Faculty of Purdue University

In Partial Fulfillment of the Requirements for the degree of

Doctor of Philosophy

School of Mechanical Engineering

West Lafayette, Indiana

August 2020

THE PURDUE UNIVERSITY GRADUATE SCHOOL
STATEMENT OF COMMITTEE APPROVAL

Dr. Yung C. Shin, Chair
    School of Mechanical Engineering

Dr. Benxin Wu
    School of Mechanical Engineering

Dr. Ganesh Subbarayan
    School of Mechanical Engineering

Dr. David Johnson
    School of Materials Engineering

Approved by:
    Dr. Nicole Key
        Head of the Graduate Program

To my patient and loving wife.

In the ways that matter, this is her work as much as mine.

ACKNOWLEDGMENTS

I'd like to acknowledge those who have been instrumental to this work. First, I'd like to thank my fellow students who helped me along the way and shared some of the tedium and excitement in equal measure.

Tyler Davis showed me the ropes and convinced me I could do it with a large family. He also introduced me to Linux. Phil Stevenson showed me FORTRAN and politeness. Caleb Harmon taught me how to prepare a sample. Hongtao Ding gave me the perspective to push through when I thought I wasn't enough. Kyung-Min Hong swapped some help and he made me some welds for free. Shunyu Liu and I helped each other with Phase Field.

Wenda Tan and I worked a lot together. He built most of the keyhole model while I only built the Fresnel absorption and multiple reflections subroutine. We also shared the CA-PF model. His quick progress and quick smile were both impressive. Chris Katinas took upon himself the tasks that I was struggling with most: thermal model simulations. He was instrumental in getting the data I needed to run my models. I could not have done it without him.

Next, I'd like to thank Dr. Shin. Through all of it, he has been a patient guide and source of wisdom that I was not always quick to follow. He taught me to take a longer look at problems and tackle them a piece at a time and to implement the right solution over the easy one. He is a model of perseverance.

I'd also like to thank my committee members that have given their time to understand, critique, and improve my work.

But most of all, I want to acknowledge my wife, Rachael. She has been with me every step of this long, winding road. We have helped each other through thick and thin. And I would be remiss if I didn't mention my children as well: Abigail, Juliet, Isaac, Luke, Nathan, and Matthew.

TABLE OF CONTENTS

LIST OF TABLES

LIST OF FIGURES

ABSTRACT

This study is focused on the prediction of residual stresses and microstructure development of steel and aluminum alloys during laser-based manufacturing processes by means of multi-physics numerical modeling.

A finite element model is developed to predict solid-state phase transformation, material hardness, and residual stresses produced during laser-based manufacturing processes such as laser hardening and laser additive manufacturing processes based on the predicted temperature and geometry from a free-surface tracking laser deposition model. The solid-state phase transformational model considers heating, cooling, and multiple laser track heating and cooling as well as multiple layer tempering effects. The residual stress model is applied to the laser hardening of 4140 steel and to laser direct deposition of H13 tool steel and includes the effects of thermal strain and solid-state phase transformational strain based on the resultant phase distributions. Predicted results, including material hardness and residual stresses, are validated with measured values.

Two dendrite growth predictive models are also developed to simulate microsegregation and dendrite growth during laser-based manufacturing processes that involve melting and solidification of multicomponent alloys such as laser welding and laser-based additive manufacturing processes. The first model uses the Phase Field method to predict dendrite growth and microsegregation in 2D and 3D. It is validated against simple 2D and 3D cases of single dendrite growth as well as 2D and 3D cases of multiple dendrite growth. It is then applied to laser welding of aluminum alloy Al 6061 and used to predict microstructure within a small domain.

The second model uses a novel technique by combining the Cellular Automata method and the Phase Field method to accurately predict solidification on a larger scale with the intent of modeling dendrite growth. The greater computational efficiency of the this model allows for the simulation of entire weld pools in 2D. The model is validated against an analytical model and results in the literature.

1. INTRODUCTION

1.1 Motivation

Laser-based manufacturing processes are becoming increasingly important in today's

manufacturing industry. From the first production laser built by Western Electric in 1965 to drill

holes in diamond dies (Adams and Butler, 1999) to modern fiber lasers used for cutting, welding,

additive manufacturing, and countless other applications (Okhotnikov, 2012), lasers have

become indispensable to many processes. Lasers are unparalleled in their ability to provide high

energy at a very small and precise location. This focused energy results in fast localized heating

and cooling, and very steep temperature gradients, which cause significant changes in resultant

microstructure and residual stresses.

There are many types of laser welding and laser-based additive manufacturing (AM) processes

commonly used in today's advanced manufacturing fields. However, fundamentally, the physical

phenomena that occur at the laser spot are very similar across laser welding and laser-based AM

processes. As the local material undergoes melting, solidification, and solid-state phase

transformation, dramatic changes can occur in the material properties of the part.

The traditional choice for understanding and predicting the changes in material properties of AM

processes is experimentation and measurement. However, the huge numbers and ranges of

experimental variables that affect material properties (not to mention the numbers of processes,

materials, and AM machines available) make this approach very time consuming and expensive.

Analytical solutions (Lipton et al., 1984, 1987; Kurz and Fisher, 1986; Kessler et al., 1988)

usually only deal with simple or ideal cases.

The alternative choice, physics-based numerical simulation, is a more desirable path (Shin et al., 2018). The foundation of predicting material properties is accurate prediction of the resultant microstructure, solid-state phase transformation, and residual stresses after an AM or laser welding process is performed.

Understanding dendrite growth during solidification of laser welding and laser-based AM processes is crucial for improving the microstructure and properties of welded/AM metals (Kou, 1987). Typical laser-based melting and solidification results in very fine grain size, columnar grains near the fusion boundary and equiaxed grains near the center of the weld pool. Accurate prediction of how these grains grow based on accurate temperature data provides a better understanding of this process and assists in achieving an optimal condition.

There are two commonly used numerical methods for modeling microstructure during solidification of AM processes: the Phase Field (PF) method, and the Cellular Automata (CA) method. The PF method is based on a set of partial differential equations and thermodynamic principles, in which the solid/liquid interface is considered to be diffuse and is defined by the continuous variation of the order parameter. CA models specialize in simulation of micro-scale dendrite growth as well as meso-scale grain growth. The strength of these models lies in their computational efficiency, but their accuracy is completely dependent on the accurate determination of growth velocity of the solid/liquid interface.

Steels are perhaps the most common material used in laser-based manufacturing processes. For most other materials, a steep temperature gradient from a laser results in tensile stresses near the surface (Solina et al., 1986; Peng and Ericsson, 1998). The high temperature and rapid cooling induced by the laser can, however, cause the steel's solid phase to transform to martensite within

the heat-affected zone (HAZ). Since the martensite phase in steels has a larger specific volume than the initial phases of pearlite and ferrite (Zhao et al., 2002; Jung et al., 2009), the phase transformation results in local expansion which can induce a strong compressive stress at the surface. This strong compressive surface stress increases fatigue strength and corrosion resistance while decreasing the surface cracking of the part (Kou, 2003).

However, the thermal strains and phase transformation-induced strains from laser-based manufacturing processes are complex and often hard to predict. Depending on heating and cooling cycles, local carbon content, part geometry, and laser operating parameters such as laser path and cross-hatching, the residual stresses can vary dramatically across the part, causing unexpected distortions to occur. Consequently, if the strains produced during laser-based manufacturing processes can be predicted via numerical modeling, these manufacturing processes can be designed with the end goal of inducing the value of the residual stresses to be beneficial to the part.

1.2   Literature Review

Many laser-based manufacturing processes experience local rapid melting and solidification including laser welding and laser-based additive manufacturing (AM) processes. During laser welding or laser-based AM processes, the weld pool experiences intense heat transfer, vigorous fluid flow, and complex laser absorption across a continually varying liquid/vapor interface. Establishing a numerical model that captures these physical phenomena has been the focus of many research groups (Fabbro and Chouf, 2000; Ki et al., 2001; Cho and Na, 2006; Rai et al., 2007; Pang et al., 2010; Svenungsson et al., 2015); this is a mature and continually developing field and has been addressed by others in the author's group (Tan et al., 2011b, 2013; Wen and

Shin, 2013; Katinas et al., 2018). Using a comprehensive physics-based numerical model that predicts the temperature field during laser-based melting and solidification processes is essential to the current work. However, the goal of the current work is to go beyond predicting heat transfer and fluid flow during the laser melting process to predicting resultant material properties.

1.2.1 Solid-State Phase Transformation in Steels

Temperature field, mechanical stress state, and microstructure are all strongly coupled together, each affecting the others. These effects are part of a phenomenon that has been termed metallo-thermo-mechanical coupling (Denis et al., 1999; Inoue, 2002), as schematically illustrated in Figure 1.1.
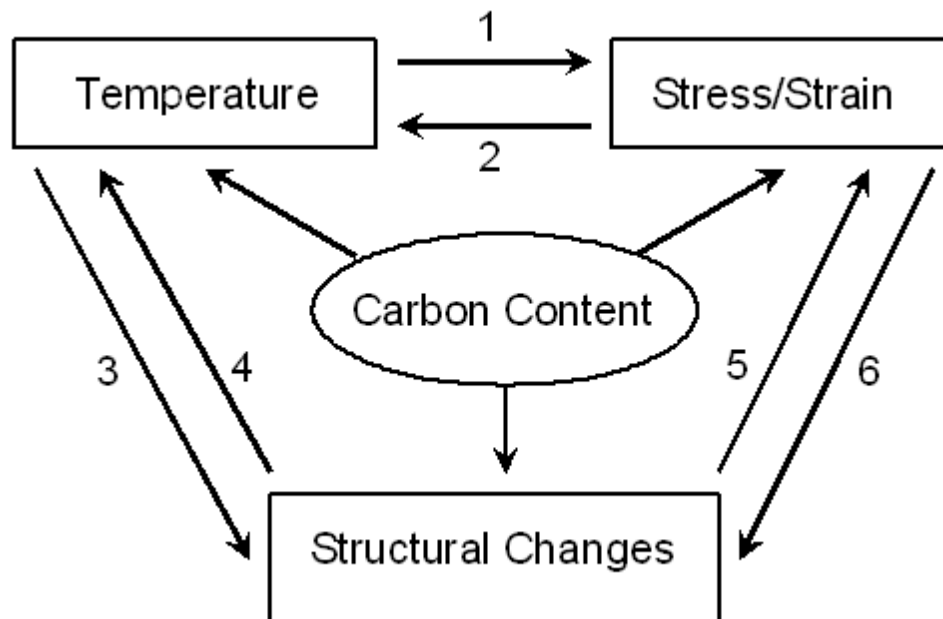
Figure 1.1: Metallo-thermo-mechanical coupling in processes involving phase transformation (Denis et al., 1999; Inoue, 2002).

Temperature fields affect the stress state through thermal strains caused by temperature gradients. This phenomenon is illustrated by arrow 1 in Figure 1.1. Temperature fields also affect

microstructural changes according to phase transformation kinetics, represented by arrow 3.
Microstructural changes, in turn, affect the stress state by causing dilatation strain, represented
by arrow 5. Reverse effects are also possible. Large strains can change the energy in the material,
slightly altering the temperature, as illustrated by arrow 2. Latent heat from solid-state phase
transformations can also alter the temperature field, represented by arrow 4. Large strains can
also assist in phase transformations, called strain-induced transformation, represented by arrow
6.

Additionally, chemical concentrations such as carbon content in low carbon steels will be
affected and in turn will influence all of these phenomena. Finally, localized melting of the
material and the subsequent solidification during laser-based manufacturing processes that
involve melting, such as laser welding and laser deposition, will have a strong effect on the
microstructure, and thus the material properties of the manufactured part.

Such extensive coupling of all these complex processes creates difficulties in numerical
modeling of laser-based manufacturing processes; ideally, all of these phenomena ought to be
solved simultaneously if all six coupling effects, carbon concentration, and melting and
solidification are to be considered. However, it is advantageous to first model the most
significant mechanisms in order to gain an understanding of a material's complex response to
laser-based manufacturing processes. These six mechanisms represented by the six arrows in
Figure 1.1 are not equally balanced, especially during laser-based manufacturing processes. For
example, temperature's effects on the microstructure is much more significant than the reverse
effect of latent heat of solid-state phase transformation. For laser-based manufacturing processes,
the most significant mechanisms affecting residual stress are thermal strains, thermally induced
solid-state phase transformations, and phase transformation-induced strains represented by

arrows 1, 3, and 5, respectively. In order to be able to predict residual stresses during laser-based manufacturing processes, all three of these mechanisms must first be accurately modeled. The other three reverse mechanisms are much less significant and may be neglected during numerical modeling.

Laser transformation hardening of steels is a surface enhancement process, similar to flame and induction hardening, but with a few distinct advantages. A high level of laser energy can be very precisely delivered to a small area of the workpiece. Since the heated region is so small, the bulk of the workpiece acts as a heat sink, causing rapid quenching. In this way, the heat-affected zone will become almost fully martensitic, producing a surface that can better withstand wear and corrosive environments while minimizing distortion. The phase transformation to martensite will also produce high compressive stresses, giving the workpiece better fatigue strength (Cerny et al., 1998; Peng and Ericsson, 1998).

Normalized steel consists of pearlite (P) and proeutectoid ferrite (α). As shown in Figure 1.2, when the material is locally heated by the laser to a temperature above the eutectic temperature, A1 (727 ℃), the pearlite colonies begin to transform to austenite (γ), while the proeutectoid ferrite remains unaffected. However, as the temperature increases further, carbon from newly formed austenite diffuses into the low carbon ferrite. If kept above T1 temperature for a sufficient time, the carbon distribution will become homogeneous. If the austenization temperature, T3, is exceeded, then any remaining ferrite will transform to austenite (Kou et al., 1983; Ashby and Easterling, 1984; Davis et al., 1986). High heating and cooling rates (as high as ~ 103 K/s) have been reported to be typical with the laser hardening process. This is due to the conduction of heat from the localized heated region into the bulk material (Skvarenina and Shin,

2006). If the subsequent cooling is fast enough, austenite is transformed almost exclusively to martensite. At lower cooling rates, the austenite will transform to both martensite and bainite.
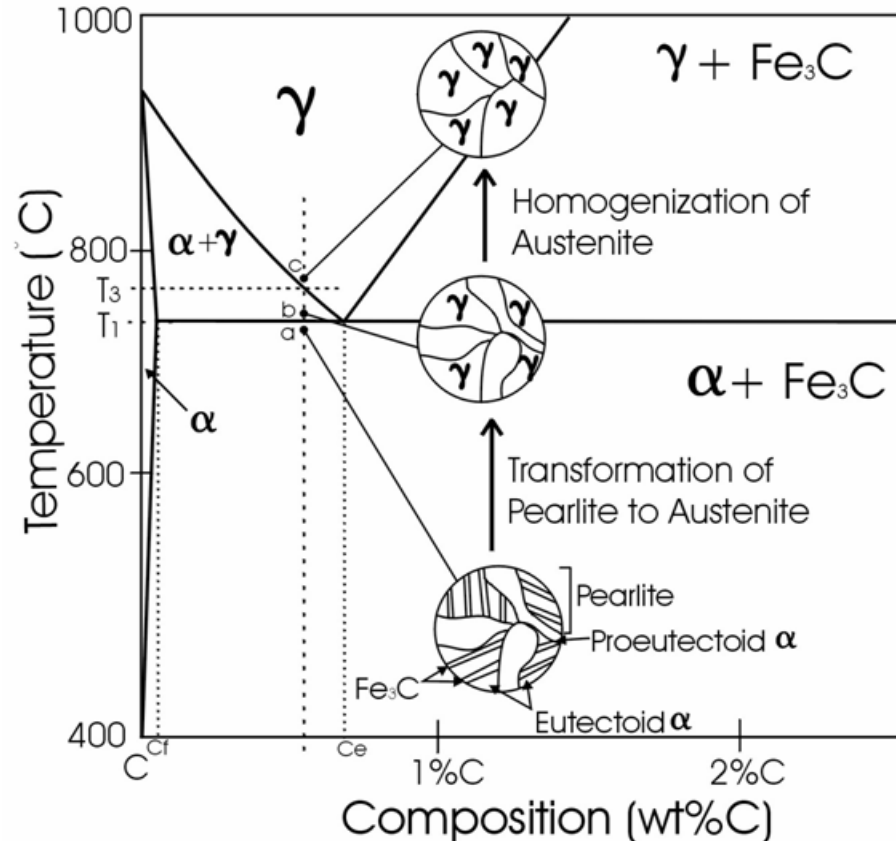
Figure 1.2: Microstructural changes in hypo-eutectoid steel during heating (Patwa and Shin, 2007).

Many researchers have presented analyses and predictive analytical models for laser transformation hardening in hypo-eutectoid steels. Ashby and Easterling (1984), using a two-dimensional analytical solution to calculate the temperature, proposed that the structural changes during heating are diffusion-controlled, and the extent of the change would depend on the total number of diffusive jumps in the cycle, measured in terms of the "kinetic strength" of the heat cycle. Austenite to martensite transformation during cooling was assumed to be independent of

diffusion but calculated by the quench rate of the cycle. They assumed that the quench rates for all heating cycles in the process were sufficient to convert all austenite to martensite when the austenite's carbon content was greater than 0.05 wt%, but this assumption is not valid for laser-based processes. Davis et al. (1986) considered complete austenization in their model by estimating the time that the workpiece must remain above A3 temperature for carbon diffusion to take place. Based on an analytical model, they presented a simple formula to predict the depth of laser hardening from operating parameters. Komanduri and Hou (2001, 2004) used a thermal analytical heat transfer model based on a moving heat source method to predict laser hardening of AISI 1036 steel. Hardened regions were determined by peak temperatures and temperature interaction times. Leung (2001) and Leung et al. (2007) developed a mathematical formulation to a 2D quasi-steady state laser hardening situation with a custom beam profile, but the simplified phase transformation was predicted by a constant phase-change temperature. Tobar et al. (2006) studied single-track laser transformation hardening of H13 steel using an analytical solution for a semi-infinite media followed by a finite element analysis through ANSYS, wherein the microstructural changes were calculated based on the Johnson–Mehl–Avrami and Koistinen–Marburger equations, but because they only studied the single-track case, tempering was not considered. Mioković et al. (2007) presented a systematic analysis on the effects of heating and cooling rates on the resultant phase formation using a pin type structure with laser heating on the top. A coupled heat conduction and phase transformation model with temperature dependent parameters was used to calculate the resultant phase transformation and hardness, but their analysis was only valid for a 1-D pin being heated from the top by a laser.

Analytical models are useful for ideal cases and quick calculations, but the required assumptions (i.e. semi-infinite domains, constant properties) are often too simplistic and prevent accurate

prediction for complex industrial parts. Therefore, many researchers have developed models using numerical methods to solve for the temperature field and solid phase transformation in two and three dimensions with specific geometry and boundary conditions. Kou et al. (1983) developed a three-dimensional finite difference heat flow model to obtain the temperature history in laser-hardened AISI 1018 steel. Phase transformation of pearlite and ferrite to austenite was discussed with the help of calculated peak temperatures. They predicted complete transformation of austenite to martensite based on the calculated cooling rates. However, the microstructure near the top surface of the workpiece that showed a small amount of ferrite led them to believe that the time allowed for carbon atoms to diffuse in austenite was still not sufficient. Ohmura et al. (1989), in addition to numerically solving the heat flow, also included carbon diffusion in austenite and solved Fick's Law of diffusion to obtain carbon concentration. During cooling, they assumed that if the cooling rate is higher than the critical cooling rate, the austenite transforms to martensite starting at $T_{m\text{-}start}$ (martensite start temperature), and if the cooling rate is lower than the critical cooling rate, the austenite is transformed to fine pearlite. Jacot and Rappaz (1999) developed a two-dimensional model for the heating cycle in laser hardening of hypo-eutectoid steels that combined all the steps: the dissolution of pearlite, the transformation of ferrite into austenite, the homogenization of carbon, and the grain growth of austenite. Their calculation for carbon diffusion starts at eutectoid temperature and stops when the domain is entirely austenite and the distribution of carbon satisfies a given homogenization criterion, but they did not consider the cooling cycle.

Costa et al. (2005) developed a method that uses finite element software ABAQUS to calculate heat transfer and phase transformation in a laser powder deposition system. Since cooling rate was not considered, the volume fraction of martensite was assumed to be 100%. Upon

subsequent heating from additional deposition tracks, martensite tempering was calculated based on peak temperature. Lusquinos et al. (2007) used ANSYS to predict temperature cycles in laser hardening of AISI 1045 and predicted the hardening depth based on peak temperature. Cooling and tempering were not considered. Patwa and Shin (2007) combined a 3D numerical model heat transfer model based on rotating cylindrical geometry with an analytical kinetic model describing pearlite dissolution, carbon redistribution in austenite and subsequent transformation to martensite to predict the solid phase transformation during laser hardening of steel on a lathe. This model, however, did not consider the cooling cycle or multi-track tempering. Skvarinina and Shin (2006) developed a 2D numerical kinetic model to more accurately predict the diffusion of carbon throughout the HAZ. When linked to the cylindrical thermal model of Patwa and Shin (2007), they were able to accurately predict 2D cross-sections of the hardness field for single-track cases. Lakhkar et al. (2008) expanded this 2D kinetic model to include the tempering effect on the microstructure caused by multiple passes of the laser and used this capability to maximize the distance between two tracks while maintaining a minimum hardness in the tempered region between the tracks. A model by Tani et al. (2007) predicts the 2D phase transformation and hardness profile after laser hardening using a finite difference method to calculate both the heat transfer and carbon diffusion. A digitized photomicrograph of the steel was used to simulate an initial microstructure. An expansion of the model (Tani et al., 2008) neglected the carbon homogenization and initial microstructure to allow for faster computation and an Avrami kinetic approach was used to include the effect of steel softening due to tempering phenomena, similar to the work of Lakhkar et al. (2008).

Although many of the models mentioned here have pieces of a comprehensive solid phase transformation model, all are missing at least one component (i.e. numerical solution, 3D

capabilities, accurate temperature prediction, cooling cycle, tempering effects). Based on the models developed by Patwa and Shin (2007), Skvarenina and Shin (2006), and Lakhkar et al. (2008), a comprehensive 3D solid phase transformation model is used by the author that considers heating, cooling, and tempering in steels for the purpose of calculating solid phase transformational stresses (Bailey et al., 2009).

1.2.2 Residual Stress Prediction

As discussed above, laser-based manufacturing processes cause large temperature gradients in the material, inducing large thermal strains that can result in strong tensile stresses at the surface of the part. In steels, fast heating and cooling rates typical of laser-based processes can produce strong compressive stresses near the surface due to the solid phase transformation physics of steel. Therefore, both thermal strains and solid phase transformation-induced strains must be well understood in order to predict residual stresses in laser-based manufacturing processes with steel.

Grigor'yants et al. (1987) used the X-ray diffraction method to measure residual stresses in pure iron and steel samples treated with a continuous CO_2 laser irradiation with varying power. Compressive stresses were observed when the material was taken through phase transformation to martensite, but tensile stresses were observed wherever significant residual austenite was found. Solina et al. (1986) and Peng and Ericsson (1998) have reported the effect of phase transformation on residual stress states. Both have shown that thermal residual stresses in laser hardening treatments are tensile while phase transformation-induced residual stresses (austenite to martensite) are compressive. The generation of residual stress depends not only on the temperature field to which it has been subjected, but also on the microstructural changes that have taken place.

Residual stress prediction during thermal processes has been an area of research over decades and the early attempts were focused on solid-state processes that did not include melting and solidification. In laser hardening of medium carbon steels, Yang and Na (1991) emphasized the large influence of transformational strain on the residual stress distribution. In their analytical model, the volume changes of austenite and martensite transformation was considered by thermal dilatation for which the equivalent linear thermal expansion coefficients were adopted and they calculated transformational strain in both uni-axial and multi-axial stress states. Transformational strain was shown to significantly influence the residual stresses in steels, and therefore cannot be neglected. Their formulation, however, did not consider the dependence of transformational strain on the yield stress of the material. Das et al. (1992) used a better formulation of transformational strain (presented by Oddy et a.(1989)) in conjunction with a finite element analysis using ABAQUS to predict residual stresses in quenching of steel cylinders. Similarly, Lacarac et al. (2002) compared residual stresses in steels with and without phase transformations. They developed a non-dimensional finite element approach for long bars of infinite length and determined the effect of non-dimensional parameters and non-dimensional metallurgical time on residual stresses and microstructure. As per their analysis, forgings that were quenched in water resulted in fully martensitic microstructures and developed strong residual stresses while forgings that cooled in air resulted in ferrite-pearlite microstructures with negligible residual stresses. Şimşir and Gür (2008) used commercial finite element software MSC-Marc to determine residual stresses in steel considering thermal and phase transformation-induced strains applied to quenching of a steel cylinder. The phase transformations were calculated using the Johnson–Mehl–Avrami-Kolmogorov kinematic model. The mechanical

model considered thermal strains, volumetric dilatational strains due to phase transformations, and transformation-induced plasticity strains.

Many laser-based manufacturing processes, however, involve local melting and solidification of the material and a comprehensive predictive model must account for the effects of melting and solidification. This requirement adds two additional levels of complexity: first, a numerical thermal model must be much more complex to simulate the behavior of the melt pool; and second, the residual stress model must account for the local loss of mechanical strength in the melt pool.

Many researchers have developed simple numerical thermal models using commercial software such as ANSYS, ABAQUS, or COMSOL to feed the temperature data into their finite element residual stress models. Using ANSYS, Labudovic et al. (2003) developed a finite element model that calculates transient temperature profiles and residual stresses, but did not predict the detailed profile of the laser track. They also neglected to consider phase transformation-induced strains in their residual stress prediction when they simulated MONEL 400 powder deposited onto a steel substrate. But the residual stresses resulting from the solid phase transformations in the steel substrate were undoubtedly significant and should not have been neglected. Using COMSOL, Alimardani et al. (2007) created an FE model and predicted the geometry and residual stresses during laser deposition of 304 stainless steel, but did not consider solid phase transformation-induced strains. Using the commercial finite element package SYSWELD, Wang et al. (2008) predicted microstructure and residual stresses in a 3D powder deposited stainless steel sample. The model used to calculate solid phase transformation-induced strains was, however, not presented in detail. Zhan et al. (2009) also used SYSWELD to predict residual stresses in a melt-hardened workpiece, wherein microstructural changes were based on the Johnson–Mehl–Avrami

equations. However, their stress calculations did not include phase transformation-induced strains. Kamara et al. (2011) used ANSYS to predict temperature and resulting residual stresses in a thin wall of Waspaloy deposited onto an Inconel substrate, again with no solid phase transformation-induced strains.

To make modeling easier, many residual stress finite element models for laser direct deposition used a simplified computational domain where the deposited track profile is assumed to have a known profile based on a geometric shape such as a flat melt surface, an ellipse, or a circle. This simplification allows for the deactivation and reactivation of finite elements to be based on a mathematical function (i.e. the simplified melt pool geometry traveling through the material at the laser travel speed), rather than the physical track profile as predicted by a deposition model's free-surface tracking. Brückner et al. (2007) presented a finite element model for laser cladding to predict residual stresses and they also accounted for strains caused by phase transformation in steel. However, instead of simulating a free surface, their clad geometry was generated from a sheared ellipsoid passing over to an elliptical cylinder at the solidification front. Santhanakrishnan et al. (2011) used ANSYS to predict temperature during high power direct diode laser cladding of H13 tool steel onto a 4140 steel substrate, and then used the temperature to predict the phase transformation kinetics and the hardness in the clad material. Their residual stress model includes an element birth-and-death technique to simulate the melting and solidification. The thermal model did not include free surface tracking, but a preprogrammed surface profile. Farahmand and Kovacevic (2014) developed a model that predicts residual stresses in multi-track cladding with a high power diode laser, including phase transformational stresses in steels. Again, the predicted track geometry was preprogrammed and not based on a free-surface tracking model.

In order to more accurately predict the residual stress in a laser-based manufacturing process that includes material melting, the deactivation and reactivation of finite elements ought to be based on an accurate physics-based prediction of melting and solidification rather than a simplified thermal model or preprogrammed surface profile. This will allow for prediction in more general cases of laser-based melting processes of complex geometry.

1.2.3 Microstructure Evolution during Solidification

Accurate microstructure prediction involves simulating dendrite growth (Flemings, 1974; Kurz and Fisher, 1998; Stefanescu, 2010). The two most popular numerical methods for simulating dendrite growth are the Phase Field (PF) and Cellular Automata (CA) methods, which are further reviewed in the next sub sections.

1.2.3.1 Phase Field Method

The phase field (PF) method has been the most commonly used method for predicting dendrite growth during solidification. The PF method is based on a set of partial differential equations and thermodynamic principles, in which the solid/liquid interface is considered to be diffuse and is defined by the continuous variation of the order parameter ϕ and a defined interface thickness, 2λ (Ode et al., 2001a; Boettinger et al., 2002; Chen, 2002; Gránásy et al., 2004; Takaki et al., 2014; Zhang et al., 2019). Most PF simulations presented in the literature have been performed under ideal or simple conditions, i.e., pure substance or simple binary alloys, an isothermal temperature field or imposed temperature gradient or cooling rate as will be described in the following texts. However, actual industrial solidification processes as in welding and AM processes are rarely ideal and predictive modeling must take into account complex alloy compositions and transient 3D temperature fields.

Suzuki et al. (2002) developed one of the first multi-component PF models, which was an expansion of their two-phase binary model (Kim et al., 1999). In order to handle multicomponent alloys, they assumed that the PF interface is a mixture of liquid and solid phases of various compositions, but all have identical "chemical potential" and the same location, even when a strong chemical potential gradient exists throughout the interface. However, it was found that early PF models, while qualitatively accurate, were quantifiably unreliable in determining concentration fields and precise dendrite morphology, because, in order to be computationally feasible, the interface thickness was too large and they underpredicted the degree of solute diffusion immediately near the interface. Karma (2001) addressed this issue by developing the anti-trapping current term which adds a subtly enhanced diffusion at the interface away from the solid. Kim (2007) later expanded his model to include an anti-trapping current term that prevents excess solute trapping.

When linked to the CALPHAD method, the PF method is able to predict, with additional computational cost, dendrite growth of complex multicomponent alloys (Ode et al., 2000). PF models have been applied to ternary alloys (Grafe et al., 2000; Ode et al., 2000; Kobayashi et al., 2003; Cha et al., 2005; Berghoff and Nestler, 2015) and even higher-order systems (Böttger et al., 2006; Eiken, 2010; Kundin et al., 2014), to obtain realistic multi-phase microstructure patterns. Over the past 20 years, the PF method has been continually developed to improve simulation of solidification processes on the micro scale. Mostly due to limited computing resources, early PF models could only predict dendrite growth in 2D, but a simple thought experiment can show the importance of 3D simulation in alloy solidification. It is well known that the two most significant factors in alloy solidification are temperature and species concentration at solid/liquid interface (Kou, 1987). As solidification occurs, solute is rejected at

the interface into the melt, resulting in a build-up of solute in the melt at the solid/liquid interface. More favorable solidification conditions can only be reached as temperature drops and high concentration solute diffuses into the bulk melt. In 2D PF modeling, diffusion is limited to one plane, i.e., solute must diffuse directly away from the interface. In 3D PF modeling, however, solute may diffuse in all directions and the difference between diffusion in 2D vs. 3D PF models can obviously have a strong effect on dendrite morphology. Kundin et al. (2019) recently presented 2D results comparing predicted vs. measured secondary dendrite arm spacing during the selective laser melting process. However, they state that their results should be verified in 3D due to the "non-trivial" differences between 2D and 3D simulations.

Aside from the advantages of 3D over 2D PF simulation, proper treatment of the temperature field is also an important issue. An isothermal temperature field or imposed temperature gradient or cooling rate may be a legitimate approximation for predicting microstructure development in some casting processes with slow cooling rates. However, to predict microstructure in many other industrial solidification processes such as welding and additive manufacturing, a PF model ought to utilize a complex and highly transient temperature field that closely matches the underlying physics. To calculate the temperature fields used in their PF models for welding and AM processes, some researchers have used basic predictive thermal models (some examples include an FEM-based thermal model with prescribed element deactivation and reactivation (Nie et al., 2014), and an imposed weld pool shape approximated mathematically by two half ellipsoids where the back edge of the shape is an isotherm at the solidification temperature of the alloy (Zheng et al., 2014; Yu et al., 2018)), but these PF models were limited to 2D predictions.

George and Warren (2002) were one of the first groups to develop a 3D PF model that could simulate realistic isothermal dendrite growth in a binary alloy. Since adding another dimension

to the simulation domain increased the computational cost by an order of magnitude, they included details of their parallel computing approach with a discussion of its advantages. Recently, researchers have begun to develop 3D PF models with more capabilities for isothermal or imposed temperature gradient simulations, but these models still lack a realistic temperature field for fast-cooling industrial processes such as laser-based AM or welding processes. Chen et al. developed an adaptive mesh 3D PF model to study the differences between 2D and 3D simulation results in both equiaxed dendrite solidification (Chen et al., 2009) and cellular grain growth (Tsai et al., 2010), but their simulations were limited to isothermal or imposed temperature gradient fields. Yuan and Lee (2010) also studied the effects of natural and forced convection in an initially isothermal field on columnar and equiaxed dendrite growth using both 2D and 3D PF models, and concluded that growth rates and morphologies were drastically different between the 2D and 3D cases because the convectional flow fields between 2D and 3D are drastically different. Zhang et al. (2019) performed a similar study using the lattice-Boltzmann method to calculate convection with similar results but also limited to isothermal conditions. Gong et al. (2019) performed a quantitative comparison of dendrite tip velocity and radius in 2D vs. 3D under isothermal forced convection, concluding that the stark differences in 2D vs. 3D convection and diffusion is the fundamental factor causing the distinctions of dendrite growth rates and morphologies in their results of 2D vs. 3D. In 3D, liquid can flow in many directions around the complex geometry of the dendrite; but in 2D, the flow is restricted to travel in one plane. Even without the presence of significant convection, solute diffusion in 2D is also limited to diffusion within one plane and will significantly affect the morphology of the dendrite growth. Their formulation included temperature fluctuations caused by latent heat of fusion, but the initial temperature field was again isothermal. Perhaps the best existing example of

microstructure prediction during a fast-cooling industrial process (welding or laser-based AM) comes from Wei et al. (2017), who recently used the Monte Carlo method to predict 3D grain growth in gas tungsten arc welding of 1050A, an aluminum alloy with high iron content. Their model predicted grain growth within both the entire melt pool and the heat-affected zone (HAZ) with a computational domain size of $33 \times 6 \times 3$ mm. However, this model only predicted grain growth on a macro scale, not dendrite growth on a micro scale. It is clear from these studies that realistic microstructure prediction of welding or AM processes ought to have 3D capability; such a study is still missing in the literature.

1.2.3.2 Cellular Automata and Hybrid Methods

Cellular Automata models specialize in simulation of micro-scale dendrite growth as well as meso-scale grain growth. The strength of these models lies in their computational efficiency, but their accuracy is completely dependent on the accurate determination of growth velocity of the solid/liquid interface. In a typical example (Zhu and Hong, 2002), the growth velocity of the interface is calculated based on the undercooling as predicted by an analytical model such as the Kurz–Giovanola–Trivedi (KGT) model (Kurz et al., 1986), which assumes equilibrium solidification conditions and a parabolic dendrite tip shape. This restricts the model's accuracy to that of the analytical model, which ought to be applied only to steady state situations, limiting the simulation to qualitative prediction. As another example, a more recent model implicitly calculates the growth velocity at the solid/liquid interface by solving the transport equations for both solid and liquid phases while holding a solute conservation boundary condition at the interface (Beltran-Sanchez and Stefanescu, 2003; Pavlyk and Dilthey, 2003; Wang et al., 2003; Krane et al., 2009; Zhu et al., 2010), but is only quantitatively accurate for domains of low Péclet number (Dong and Lee, 2005; Zhu and Stefanescu, 2007; Pan and Zhu, 2010).

Early CA models used to predict dendrite growth were limited to pure materials and binary alloys. Several attempts have been made to expand these models to multi-component and/or multi-phase alloys (Zhu and Stefanescu, 2007; Michelic et al., 2010; Li et al., 2013; Chen et al., 2015), but most have made simplifying assumptions, limiting their applicability. Tan and Shin (2015) developed a 3D CA model to predict grain growth during laser melting processes of austenitic stainless steel. More recently, Wang et al. (2016a, 2016b) presented a 3D CA model coupled with a FVM model for predicting dendrite growth in forced convection conditions. Their results were limited to ideal cases of single dendrites in a constant flow field and columnar dendrites within a prescribed temperature gradient. With a similar model, Kao et al. (2019) went a step further by analyzing dendrite growth with natural convection. Guo et a. (2017) built a multi-scale 3D CA model and used it to predict dendrite growth and grain growth in directional solidification of a single crystal superalloy. Similar 3D CA models were presented by Koepf et al. (2018) and Zinovieva et al., (2018) to model grain growth during the powder bed fusion AM process. However, these models did not predict dendrite growth and they both used an analytical solution for the heat input. Gu et al. (2019) developed a 3D CA model with quantitative prediction of dendrite growth in ternary alloys applicable at low cooling rates and near steady-state growth conditions, but it is not applicable at cooling rates associated with laser melting processes (Ao et al., 2020).

The Phase Field method, discussed in Section 1.2.3.1, is a more elegant solution, but with a much higher computational cost. It is established on a set of thermodynamically based partial differential equations, with a diffuse solid/liquid interface defined by the parameter ϕ (Ode et al., 2001b; Boettinger et al., 2002; Chen, 2002; Gránásy et al., 2004; Takaki et al., 2014). This modeling method has been widely used to study growth kinetics for different multicomponent

alloys on very small scales due to the high computational cost (Grafe et al., 2000; Ode et al., 2000; Cha et al., 2001; Kobayashi et al., 2003; Qin et al., 2005; Zhang et al., 2013; Bailey et al., 2020).

The major disadvantage of the PF method is the extremely high computational cost. Compared to the CA method, the PF method requires a very fine mesh to characterize the diffuse interface, greatly limiting the domain size of PF models. Adaptive mesh refinement methods have only slightly alleviated the computational cost (Provatas et al., 1998, 2005; Feng et al., 2006).

The CA and PF models listed above all suffer from the disadvantages of the respective methods; that is, the CA models cannot accurately handle multi-component alloys under rapid solidification conditions and the PF models are not computationally feasible for large domains. To dispel these disadvantages, Natsume and Ohsasa (2006) proposed a PF-CA model that used a PF submodel to predict dendrite growth in ternary alloys in order to establish a correlation between undercooling and dendrite tip velocity. The meso-scale CA model then used this correlation to predict the grain growth during casting. By using PF-based growth kinetics, this method enabled their model to handle multi-component alloys. However, since the model only utilized the PF submodel for dendrite tip velocity, overall dendrite morphology was neglected, and the meso-scale CA model was limited to qualitative grain growth prediction.

A novel microscale CA-PF model has been developed by Tan et al. (2011a). This model uses the PF method to calculate the growth kinetics of the solidification interface (along the entire interface of the dendrite) and the CA method to efficiently predict the bulk dendrite growth. This model is linked to CALPHAD databases in order to provide the Gibb's energy data to the PF portion of the model. The model has shown quantitative prediction of dendrite growth and

microsegregation during solidification of multi-component alloys over areas large enough to visualize melt pools in both cladding (Tan et al., 2012) and welding (Tan and Shin, 2015). The major advantage of this method is its superior computational efficiency to PF modeling by a 4-5 orders of magnitude without losing the fidelity.

1.3 Research Objective

The objective of the research presented here is to gain a scientific understanding of the mechanical response of alloys during laser-based manufacturing processes and use that understanding to build numerical models to accurately predict residual stresses and microstructure. The specific goals established to attain this objective are as follows:

(a) Develop a numerical model to predict the residual stresses which develop in steels during laser-based manufacturing processes.

- The model must calculate non-isotropic thermal strains during non-isothermal heating and cooling cycles.

- The model must calculate non-isotropic solid-state phase transformation-induced strains in steels.

- The model must also consider the mechanical response during melting and solidification of the material.

(b) Develop a numerical model to predict dendrite growth during solidification of laser-based manufacturing processes.

- The model must consider multi-component alloys.

- The dendrite growth must be thermodynamically based.

- The model must be computationally efficient.

(c) Validate all numerical models against experimental evidence and apply them to strategic alloys and industrial manufacturing processes.

1.4 Dissertation Outline

This dissertation includes 4 chapters. Chapter 1 comprises the introduction, including the literature review and research goals; Chapter 2 presents the modeling of phase transformation, residual stress, and microstructure development during solidification; Chapter 3 examines experimental work, including laser hardening, laser deposition, and laser welding; Chapter 4 presents the summary and conclusions, and outlines a recommendation of future work.

2. MODELING OF PHASE TRANSFORMATION, MICROSTRUCTURE DEVELOPMENT, AND MECHANICAL RESPONSE

The end goal of the models presented here is to predict the residual stresses and microstructure developed during laser-based manufacturing processes. These models rely on either a comprehensive laser deposition model developed by Wen and Shin (2010, 2011) or a laser welding model developed by Tan et al. (2013; Tan and Shin, 2014) to provide accurate temperature and free surface data to the residual stress and CAPF models that, in turn, help predict the material properties and resultant geometry of the finished part. A flowchart for the comprehensive model is shown in Figure 2.1, and detailed descriptions of the individual models and implementations are presented in this chapter
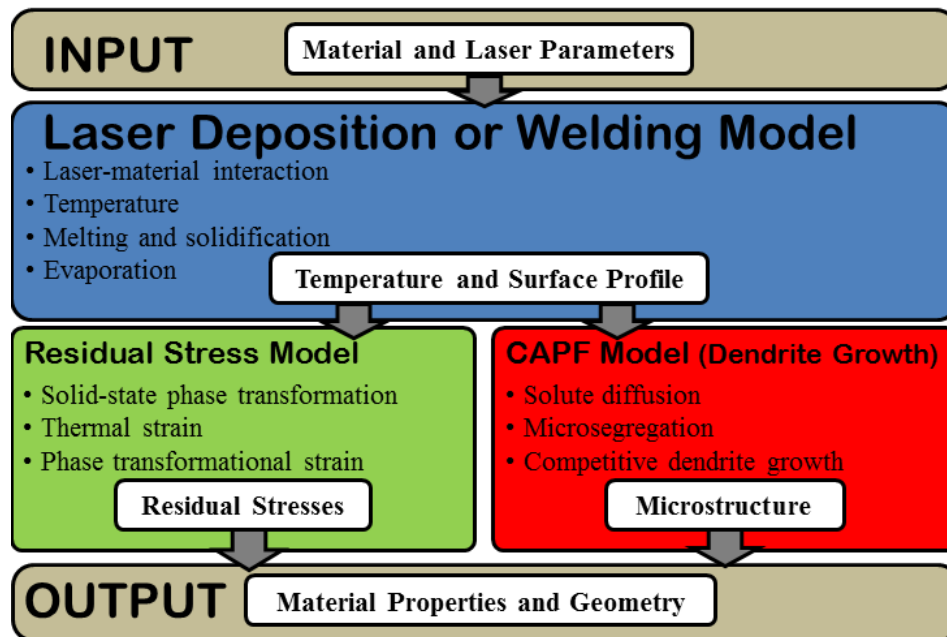
Figure 2.1: Comprehensive flowchart showing the residual stress model and the CAPF model.

As can be seen from Figure 2.1, either the laser deposition model (Wen and Shin, 2010, 2011) or the laser welding model (Tan et al., 2013) (represented by the box labeled Laser Deposition or

Welding Model) provide temperature and free-surface profile information to the residual stress model (represented by the box labeled Residual Stress Model) and the CAPF model (represented by the box labeled CAPF Model (Dendrite Growth)). These models, in turn, predict the residual stresses and microstructure developed during laser-based processes in order to predict the material properties and geometry (including distortion) of the final product.

2.1   Solid-State Phase Transformation in Steels

The sold-state phase transformation calculations are performed in a subroutine of the residual stress model. A flowchart for the residual stress model is shown in Figure 2.2 in order to illustrate the different parts of the model and how they are implemented. This figure will be referenced throughout Section 2.1 and Section 2.2. The residual stress model utilizes commercial finite element software ABAQUS and user subroutines, among other software, to calculate the stress produced during laser-based manufacturing processes. The temperature and free surface information are sent to a C++ program that is used to determine the deactivation and reactivation of each element in the finite element model through the *MODEL CHANGE command, represented by the box labeled *MODEL CHANGE in Figure 2.2. The pseudo-steady temperature data is interpolated onto the ABAQUS finite element mesh, and the local solid phase of the material is calculated based on the temperature data according to the solid-state phase transformation model during the user subroutine UEXTERNALDB. The thermal strains and the phase transformation-induced strains are then calculated during user subroutine UEXPAN, and ABAQUS solves for the prediction of resultant material stresses.
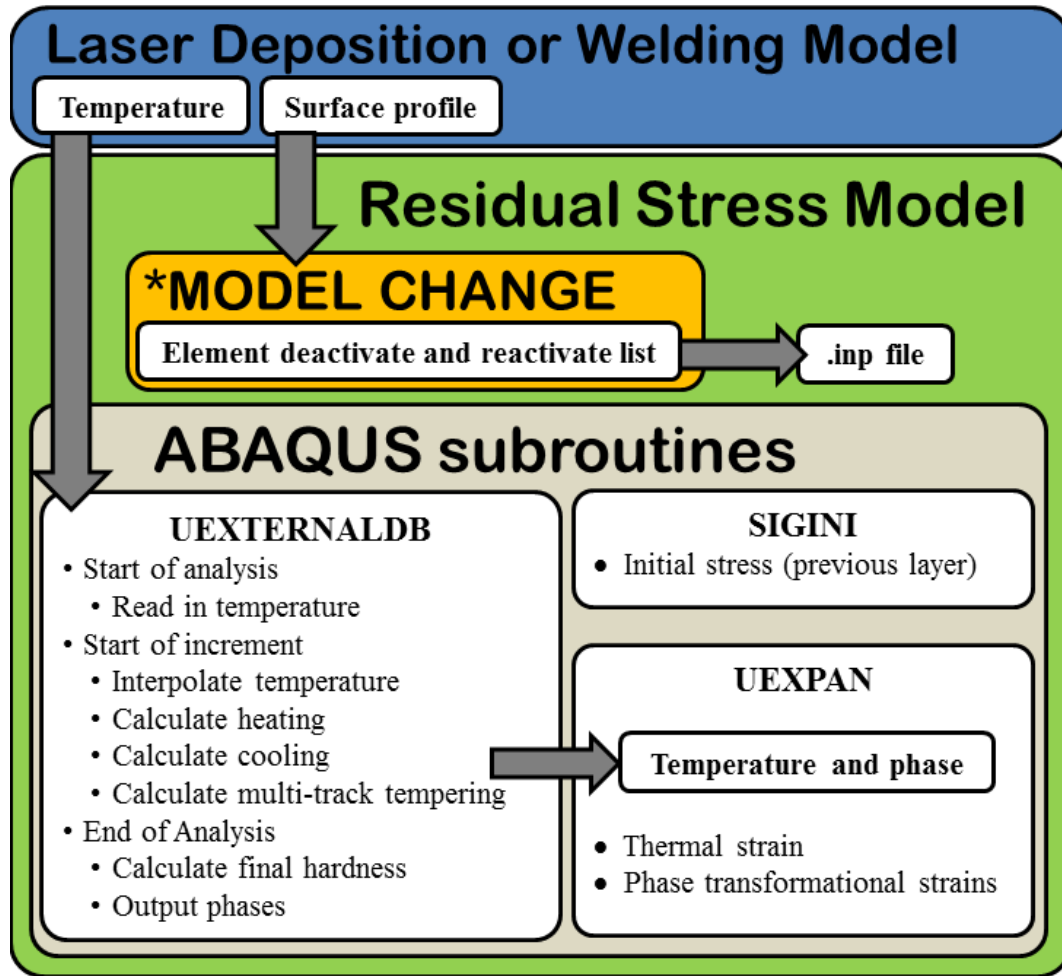
Figure 2.2: Flowchart for the residual stress model.

In material processing of steels, phase transformation kinetics have a strong influence on the behavior of the steel. Skvarenina and Shin (2006) developed a 2D kinetic model that simulates the solid-state phase transformations of hypoeutectoid steels during the heating cycle. Lakhkar et al. (2008) modified this model to include tempering cycles and Bailey et al. (2009) expanded the model to 3D and further modified it to include the cooling cycle. A sufficient description of this model and its adaptation for use in multi-track and multi-layer residual stress prediction during

laser-based processes is presented here. All solid-state phase transformation calculations are performed in a user subroutine UEXTERNALDB, as illustrated in Figure 2.2.

2.1.1 Heating

Phase transformation kinetics during the laser-based manufacturing processes can be divided into three parts: heating, cooling, and tempering. As the laser spot approaches a point of interest, the temperature increases rapidly. When the local temperature passes the eutectoid temperature (727°C), the pearlite colonies, consisting of alternating plates of high-carbon iron carbide and low carbon eutectoid α-ferrite, quickly transform into γ-austenite because the carbon in the iron carbide can quickly diffuse into the close eutectoid α-ferrite plates. As the temperature continues to increase, the carbon from the austenite colonies diffuses into the proeutectoid ferrite colonies, transforming them to austenite. Once the temperature passes the austenization temperature (between 750°C and 900°C for hypoeutectoid steels), all of the ferrite will have transformed to austenite. The transformation from ferrite to austenite between the eutectic and austenization temperatures is governed by carbon diffusion. A 2D kinetic model was built by Skvarenina and Shin (2006) that predicts the austenization of pro-eutectoid steels during non-isothermal heating by calculating carbon diffusion using a finite-difference scheme. This model was used for predicting residual stresses during laser hardening. Because the laser hardening work did not involve melting of the steel, it is important to calculate carbon diffusion in order to simulate the austenization of the steel.

However, laser-based melting processes result in such rapid heating to temperatures high above the melting temperature that the carbon diffusion may be neglected. In this case, a simplified heating model was used. As temperatures pass the eutectic temperature, all pearlite transforms to austenite. Between the eutectic temperature and the austenization temperature, the fraction

between ferrite and austenite is determined by the lever rule as defined by Callister (2003). Once the temperature passes the austenization temperature, the element is transformed to 100% austenite. These calculations are performed at each time increment in ABAQUS during the UEXTERNALDB subroutine, as illustrated in Figure 2.2.

2.1.2   Cooling

The modeling of the cooling cycle is based on Sheil's Additivity Rule, the Johnson-Mehl-Avrami (JMA) model as used by Kang and Im (2005), and the Koistinen-Marburger (KM) equation as used by Woodard et al. (1999). The details of this model are presented by Bailey et al. (2009). Since the cooling rates are very rapid, as predicted by the Laser Deposition model for the simulation presented above, the cooling model predicts that all of the austenite transforms to martensite.

The early kinetic model, as developed by Skvarenina and Shin (2006), assumes that after the thermal cycle and associated austenite homogenization has finished, all the austenite with carbon content greater than 0.05% transforms to martensite, regardless of cooling rate. However, the phase transformation model presented here has been expanded to consider the effects of cooling rate on phase transformation. As the workpiece begins to cool, austenite is transformed to martensite if the cooling rate is fast enough or bainite if the cooling rate is slower. The phase transformation in the cooling cycle of the laser hardening process is based on Sheil's Additivity Rule, the Johnson-Mehl-Avrami (JMA) model, and the Koistinen-Marburger (KM) equation (Woodard et al., 1999; Kang and Im, 2005).

In order to determine if bainite formation will occur, the current cooling time of a material undergoing non-isothermal transformation is compared with the amount of time required to

begin bainite formation in an isothermal process. Sheil's Additivity Rule discretizes the process

over a number of time steps, allowing for non-isothermal calculations. If the integral in Eq. 2.1

reaches a value of 1 before the temperature drops below the martensite formation temperature,

bainite will begin to form.

$$\int_0^t \frac{dt}{t_a(T)} \geq 1 \tag{2.1}$$

Here dt is the length of a time-step, $t_a(T)$ (obtained from the TTT diagram in Figure 2.3) is the

incubation time required isothermally at temperature T for bainite to form, and t is the current

cooling time of an austenite cell in the model. Under the parameters used in this study, bainite is

not formed because the cooling rate is sufficiently fast to avoid satisfying Eq. 2.1, thereby

avoiding formation of bainite. If Eq. 2.1 is satisfied under conditions other than those used in this

study, the JMA model is used in the present solid-state phase transformation model to calculate

the amount of bainite that would be formed.

Type: 4137/4140
Composition: Fe - 0.37% C - 0.77% Mn - 0.98% Cr - 0.21% Mo
Grain size: 7-8 Austenitized at 843°C (1550°F)

°C °F   HARDNESS-RC

800 ──   A
        1400   Af
                As
700 ──   10
        1200   20
600 ──   A + F   29
        1000 A   A + F + C   29
500 ──   29
        800   F + C   37
400 ──   50%   44
                Ms   51
300 ── 600   M50
                M90
200 ── 400
                        I-T DIAGRAM
100 ── 200

  0 ──   I MIN.   IHOUR   I DAY   I WEEK 61

        0.5 1 2 5 10   10²   10³   10⁴   10⁵   10⁶

TEMPERATURE

TIME – SECONDS
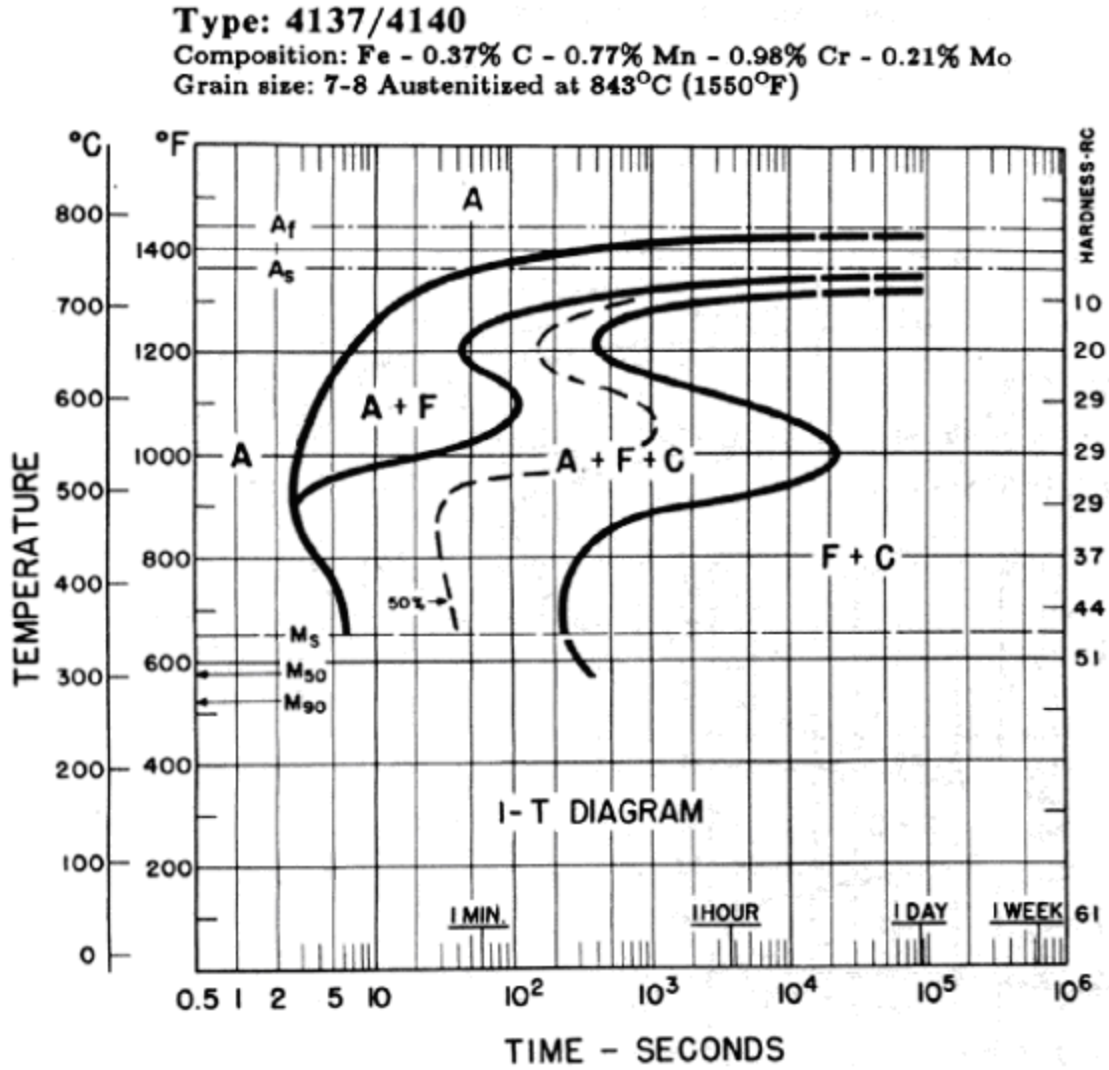
Figure 2.3: Time temperature transformation (TTT) diagram for AISI 4140 steel (Boyer and Gray, 1977).

Once the temperature has dropped below the martensite formation temperature, $T_{m\text{-}start}$, the KM equation is used to calculate the volume fraction of martensite, f_m, in the cooling process.

$$f_m = f_\gamma^*\{1 - \exp[-0.011(T_{m-start} - T)]\} \tag{2.2}$$

Here, $T_{m\text{-}start}$ (obtained from the TTT diagram) is the temperature at which martensite begins to form, and f_γ^* is the volume fraction of austenite at the time when temperature reaches $T_{m\text{-}start}$. If the cooling rate is sufficiently fast, i.e., no bainite is formed, all austenite that does not change into martensite will be considered retained austenite.

The cooling cycle uses a much coarser mesh than the heating cycle ($h = 50$ µm). Every 1000 cells are grouped together in cubes of 10x10x10 cell volumes and the average phase fraction of each cube is calculated. Cooling cycle calculations are then performed over each cube and the phase fraction of each cube adjusts accordingly. Temperature and phase are recorded at each time step. The residual stress model will use this information to calculate residual stress. Once the workpiece in the model has cooled to room temperature and phase transformations are complete, the final phase fraction field is used to calculate hardness. Cooling calculations are performed at each time increment in ABAQUS during the UEXTERNALDB subroutine, as illustrated in Figure 2.2.

2.1.3 Tempering

The tempering model, as presented by Lakhkar et al. (2008), has been expanded and adapted for use in the residual stress model. Ferrite and iron carbide phases are stable below the eutectoid temperature, while martensite is easily tempered at temperatures as low as 100°C. In single-track laser processing, tempering of martensite is not an issue; once the martensite is formed, there is no opportunity for the martensite of the single track to be tempered by the heat of a second track. With multi-track and multi-layer LDD, the heat from neighboring laser tracks can raise the local temperature high enough to temper the martensite, but not high enough to transform to austenite. When this occurs, a certain fraction of the martensite is tempered. This phenomenon must be

accurately modeled in order to predict the resultant phase and ultimately the resultant residual stresses.

In this model, if an element has a phase fraction of martensite greater than zero, and the temperature of that element reaches a maximum of temperature greater than 100°C but less than the eutectoid temperature 727°C, then the martensite may transform to the following tempered phases: ε-carbide and ferrite are formed between 100°C and 250°C, and cementite and ferrite are formed between 250°C and 727°C. The amount of martensite that is tempered, f_m, is calculated by the JMA equation:

$$f_m = 1 - e^{-\beta n} \tag{2.3}$$

where n is an empirically derived constant with a value of 0.109 (Lakhkar et al., 2008). The term β must be solved for non-isothermal conditions and is given by the following differential equation:

$$\frac{d\beta}{dt} = k + \frac{Q}{RT^2} \beta \frac{dT}{dt} \tag{2.4}$$

Where $Q = 1.97 \times 10^5$ is the activation energy of martensite and $k = 5.11 \times 10^9$ is a constant.

For temperatures between 100°C and 250°C, the fractions of ε-carbide (f_ε) and ferrite (f_α) that form from the fraction of martensite that was tempered (f_m) are calculated as

$$f_\varepsilon = \frac{f_m C_{H13} - C_\alpha}{C_\varepsilon - C_\alpha} = f_m - f_\alpha \tag{2.5}$$

where C_{H13} is the carbon concentration of H13, set at 0.4% for this simulation, and $C_\varepsilon = 8.55\%$ and $C_\alpha = 8.22\%$ are the carbon concentrations of the phases ε-carbide and ferrite, respectively.

Similarly, for temperatures between 250°C and 727°C, the fractions of cementite (f_c) and ferrite (f_α) are calculated as

$$f_c = \frac{f_m C_{H13} - C_\alpha}{C_c - C_\alpha} = f_m - f_\alpha \qquad (2.6)$$

where the carbon concentration of cementite is $C_c = 6.7\%$. At the end of the simulation, the hardness, H, of the resultant multi-layer, multi-track laser deposited material is calculated by

$$H = \sum_x H_x f_x \qquad (2.7)$$

where H_x are the hardness values of the various phases and f_x are the phase fractions. Tempering calculations are performed at each time increment in ABAQUS during the UEXTERNALDB subroutine, as illustrated in Figure 2.2.

2.1.4   Melting

In order to predict residual stress in laser-based melting processes, the numerical model must take melting and solidification into account. In order to simulate melting and solidification, this model utilizes the ABAQUS command *MODEL CHANGE, as illustrated by the box labeled *MODEL CHANGE in Figure 2.2. This command deactivates and reactivates elements according to element sets given for each step in ABAQUS. This command must be implemented in the input file and therefore the temperature and the level-set data must already be known.

A C++ program was written which imports the temperature and level-set fields from a previously developed Laser Deposition model (Wen and Shin, 2010, 2011) and interpolates these fields onto

the ABAQUS mesh. During a given time increment, each element that melts during this time increment is added to one list, while each element that solidifies during this time increment is added to another list. Both melting and solidification lists for each time increment are written to a file and copied into the ABAQUS input file as element sets, with two sets for each step in ABAQUS. During the first step of a simulation, the top layer of elements that will represent the deposition layer will be deactivated so that they may be reactivated to represent the additional material added during LDD. The time duration of a step is the given time increment mentioned above; for the simulation presented here, this is set to 0.004 seconds.

Thus, during each step, two sets of elements that represent the regions of melting and solidification become deactivated and reactivated, respectively. The stress existing in the recently deactivated elements is lost and the stress in the recently reactivated elements is initialized to zero. In this way, the melt pool cannot hold stress and the mechanical response of the deposited material is accurately simulated.

2.2   Residual Stress

Many simultaneously occurring physical phenomena affect the mechanical response of the material; in order to predict the resultant residual stress state, the relevant mechanical strains must be accurately modeled. The residual stress model presented here includes the effects of thermal strains, solid-state phase transformation-induced strains, melting, multiple laser tracks and multiple layers, and laser tempering effects. Thermal and phase strains are calculated during the UEXPAN user subroutine in ABAQUS as illustrated in the box labeled Residual Stress Model in Figure 2.2. The relevant thermal $\Delta\varepsilon_{ij}^{T}$ and phase $\Delta\varepsilon_{ij}^{Phase}$ strain increments can be added to the elastic $\Delta\varepsilon_{ij}^{E}$ and plastic $\Delta\varepsilon_{ij}^{P}$ strain increments according to Eq. 2.8.

$$\Delta\varepsilon_{ij} = \Delta\varepsilon_{ij}^E + \Delta\varepsilon_{ij}^P + \Delta\varepsilon_{ij}^T + \Delta\varepsilon_{ij}^{Phase} \tag{2.8}$$

It is assumed that elastic and plastic strains are independent of material phase but are strongly

dependent on temperature. To model the plastic strain, a Johnson-Cook hardening model was

used.

2.2.1   Thermal Strains

Anisotropic thermal strains exist in a workpiece wherever thermal gradients exist. The thermal

strain increment is defined by the temperature increment, ΔT, and the multi-component thermal

expansion coefficient, α, according to Equations 2.9 and 2.10.

$$\Delta\varepsilon_{ij}^T = \alpha(\Delta T)\delta_{ij} \tag{2.9}$$

$$\alpha = \sum_x \alpha_x f_x \tag{2.10}$$

Here, f_x is the phase fraction of phase x and α_x is the thermal expansion coefficient of phase x. A

list of thermal expansion coefficients used in Eq. 2.10 is given in Table 2.1.

Table 2.1: Thermal expansion coefficients for steel phases.

Thermal expansion coefficient, α_k	
ferrite, α_α	1.61×10^{-5} 1/°C*
pearlite, α_P	1.53×10^{-5} 1/°C†
austenite, α_γ	2.20×10^{-5} 1/°C†
martensite, α_m	1.15×10^{-5} 1/°C‡
cementite, α_c	1.48×10^{-5} 1/°C‡
ε-carbide, α_ε	1.48×10^{-5} 1/°C‡

*(Zhao et al., 2001)
†(Zhao et al., 2002)
‡(Jung et al., 2009)

2.2.2 Phase Transformation-induced strains

When a given volume in a material transforms from one solid phase to another, the crystal structure can change. For example, austenite changing to martensite will transform from a face-centered cubic structure to a body-centered cubic structure, thereby expanding the volume. The strain increment due to this volumetric expansion (or contraction as the case may be) is given by the first term on the right-hand side of Eq. 2.11.

$$\Delta \varepsilon_{ij}^{Phase} = \frac{1}{3} \frac{\Delta V}{V} \Delta X \delta_{ij} + \frac{5}{4} \frac{S_{ij}}{Y} \frac{\Delta V}{V} (2 - 2X_n - \Delta X) \Delta X \qquad (2.11)$$

The percent volume change, $\Delta V/V$, due to phase transformation from one phase to another is listed in Table 2.2. The incremental change in phase fraction is defined as ΔX. The second term on the right-hand side of Eq. 2.11 is the transformation-induced plasticity strain as reported by Das et al. (1992). S_{ij} is the deviatoric stress tensor, X_n is the amount of phase already changed during the entire cycle, and Y is the yield stress of the weaker phase, which is usually austenite during these transformations.

Table 2.2: Phase strain properties for steel phases.

Volume change, $\Delta V/V$	
pearlite to austenite	-0.33%*
ferrite to austenite	-0.38%†
austenite to martensite	1.03%*
martensite to cementite	-0.81%‡
martensite to ε-carbide	-0.71%‡

* (Jin, 2001)
† (Zhao et al., 2002)
‡ (Jung et al., 2009)

2.2.3   Model Implementation
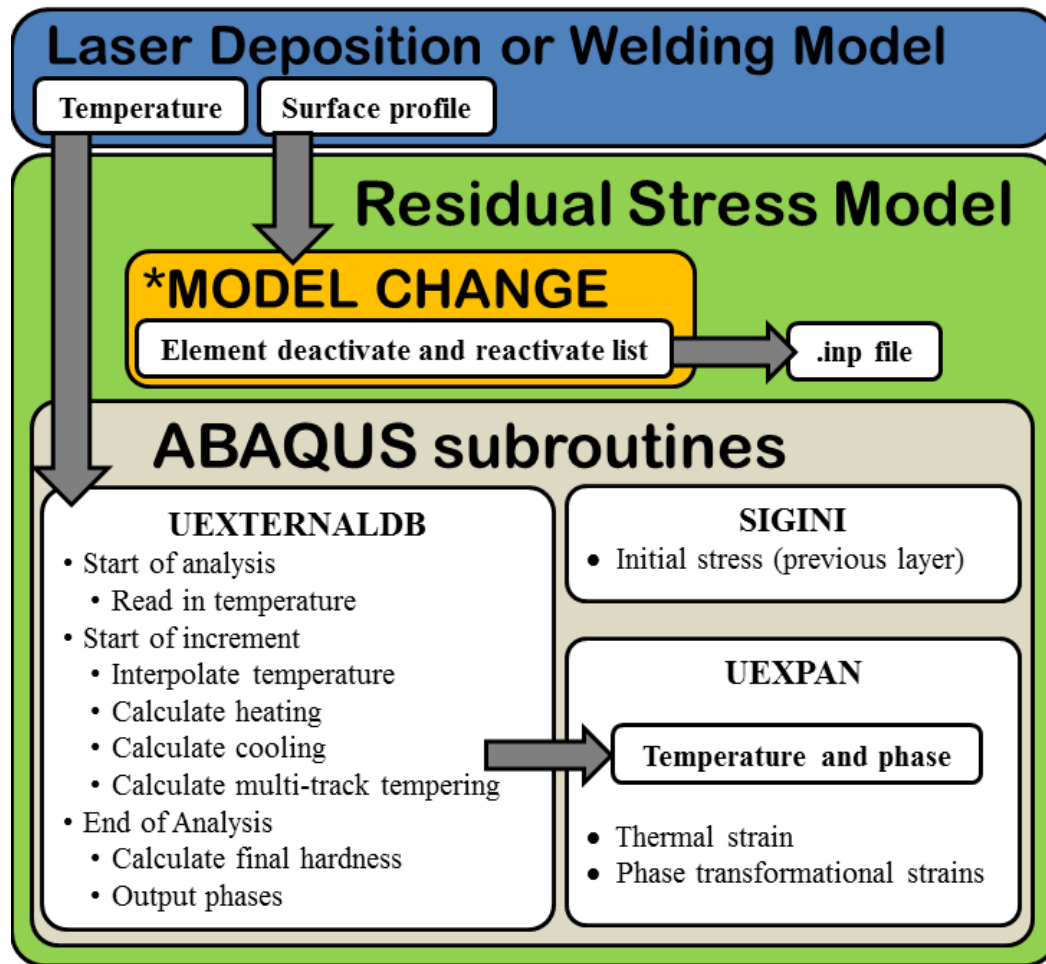
Figure 2.4: Flowchart for the residual stress model.

All pieces of the residual stress model are discussed above. The thermal and phase strains are

calculated in user subroutine UEXPAN, as shown in the lower right corner of Figure 2.4. These

calculations require the temperature field of the current time step and the previous time step

which were interpolated from the either the laser deposition model or the laser welding model

(box labeled Laser Deposition or Welding Model) for each time step as the laser advances across

the domain. Once one laser track has traveled across the domain, another track will travel

parallel to the first track across the domain. This continues until the entire domain has been simulated for one layer of laser deposition.

After the first layer has cooled and the residual stress calculations for the first layer are complete, the residual stress field is exported into commercial data viewing software Tecplot. Once in Tecplot, the six stress fields are rotated 90° in the domain (since the cross-hatching orientation of two adjacent layers is orthogonal) and lowered a distance equivalent to the layer thickness. These stress fields that have been rotated and lowered are then read back into ABAQUS via user subroutine SIGINI (SIGma INItial, or the initial stress field). In this way, the residual stress of each layer is an initial condition for the next layer's calculations. Now the domain is ready to simulate the second layer of deposition. Once the second layer has cooled, the process may be repeated as many times for as many layers as necessary. Model validation and implementation results are presented in Chapter 3.

2.3   Microstructure Evolution During Solidification

Solidification during laser melting processes such as laser welding, cladding, and deposition affects the material properties of the finished product, including the residual stress. Modeling the solidification process can further the understanding of these effects. As discussed in Section 1.2.3, two common methods for modeling the solidification process on the micro scale are the Cellular Automata method (CA) and the Phase Field method (PF). The CA method is very computationally efficient but lacks the physics-based accuracy of the PF method. On the other hand, the phase field method is very computationally expensive, but much more physically accurate and can simulate solidification of multicomponent alloys.

2.3.1 Phase Field Modeling and Validation

When it comes to simulating dendrite solidification, the biggest strength of the PF method is that it is thermodynamically based and therefore easily applicable to multi-component systems. When combined with material-specific Gibb's energy equations (i.e. CALPHAD method (Kaufman and Bernstein, 1970)), the solid and liquid concentrations are easily determined in the PF model throughout the PF domain. However, there is a high computational cost for constantly calculating the thermodynamics throughout the domain. To save computation time, a dilute solution approximation (Kim et al., 1999) can be made, which assumes the alloy can be represented by a simple binary alloy with a constant partition coefficient.

As mentioned in Section 1.2.3.1, phase field models utilize the phase parameter, ϕ, to define a material's phase throughout the entire field. The thickness of the diffuse solid/liquid interface is defined by 2λ. It has been shown that in the case where the interface thickness, 2λ, approaches zero, the phase field equation can become a classic sharp-interface model such as the Stefan model, modified Stefan model, or Hele-Shaw model (Caginalp and Xie, 1993). These models have been used to describe free boundary problems with moving interfaces such as solidification (Caginalp, 1989). However, while computationally expensive, having a diffuse interface gives the PF model the advantage of being able to simulate physical effects within the interface, resulting in more accurate simulation.

The PF equation and coupled solute diffusion equation can be expressed as Eq. (2.12) and Eq. (2.13), respectively (Kim et al., 1999). These equations define the PF parameter, ϕ, and the concentration of the solute, c.

$$\frac{1}{M_\phi}\frac{\partial \phi}{\partial t} = \nabla \cdot \epsilon^2 \nabla \phi - \frac{\partial f}{\partial \phi} \tag{2.12}$$

$$\frac{\partial c}{\partial t} = \nabla \left[D(\phi)H(\phi, c_S, c_L)\nabla \ln \frac{c_L}{1 - c_L} \right] \tag{2.13}$$

Here, M_ϕ is the PF mobility, ϵ is the coefficient of PF gradient energy, f is the free energy density, $D(\phi)$ is the phase-dependent diffusion coefficient, $H(\phi, c_S, c_L)$ is related to the difference in energy between solid and liquid, and c_L and c_S are the concentrations of the liquid and solid, respectively, at the interface.

To predict dendrite growth, the PF model must consider the anisotropic growth preference experienced in crystalline growth. This is commonly done through the ϵ term in Eq. (2.12) by inserting an anisotropy parameter $\epsilon = \epsilon_0 \eta(\boldsymbol{n})$ where $\epsilon_0 = \sqrt{3\sigma 2\lambda/\alpha}$, σ is the interface energy for the binary material, 2λ is the width of the solid/liquid interface, and $\alpha \cong 2.2$ is a constant dependent on the definition of the interface. The anisotropy term, $\eta(\boldsymbol{n})$, is described in Eq. (2.18) below. Since ϵ is dependent on ϕ, Eq. (2.12) must be expanded to (George and Warren, 2002):

$$\frac{1}{M_\phi}\frac{\partial \phi}{\partial t} = \epsilon_0{}^2 \nabla \cdot (\eta^2 \nabla \phi) + \epsilon_0{}^2 \frac{\partial}{\partial x}\left(|\nabla \phi|^2 \eta \frac{\partial \eta}{\partial \phi_x}\right)$$

$$+ \epsilon_0{}^2 \frac{\partial}{\partial y}\left(|\nabla \phi|^2 \eta \frac{\partial \eta}{\partial \phi_y}\right) + \epsilon_0{}^2 \frac{\partial}{\partial z}\left(|\nabla \phi|^2 \eta \frac{\partial \eta}{\partial \phi_z}\right) - \frac{\partial f}{\partial \phi} \tag{2.14}$$

and for the dilute solution formulation Eq. (2.13) can be expanded to

$$\frac{\partial c}{\partial t} = \nabla \left[[D_S \phi + D_L (1 - \phi)] \right.$$

$$\left. * [h c_S (1 - c_S) + (1 - h) c_L (1 - c_L)] \nabla \ln \frac{c_L}{1 - c_L} + j \frac{\partial \phi}{\partial t} \frac{\nabla \phi}{|\nabla \phi|} \right]$$

(2.15)

where the liquid concentration at the interface is defined as $c_L = c/[1 + h(k - 1)]$, $k = {}^{c_S}/_{c_L}$ is

the partition coefficient for a binary alloy (Kim et al., 1999), and j is the strength of the anti-

trapping current term (Kim, 2007) given by

$$j = \frac{\sqrt{2w}}{\epsilon} (c_L - c_S)$$

(2.16)

where $w = 6\sigma\alpha/2\lambda$. For the dilute solution approximation, the thermodynamic force, TDF, is

defined as

$$TDF: -\frac{\partial f}{\partial \phi} = wg' - n \frac{RT}{V} h' \ln \frac{(1 - c_S^e)(1 - c_L)}{(1 - c_L^e)(1 - c_S)}$$

(2.17)

where w is the double well potential defined as $w = 6\sigma\alpha/2\lambda$, g' is the derivative of $g =$

$\phi^2(1 - \phi)^2$ (which ensures the double well potential term, w, is only applied within the

interface), h' is the derivative of $h = \phi^3(6\phi^2 - 15\phi + 10)$, R is the universal gas constant, T is

the local temperature (non-isothermal), and V is the specific volume (Kim et al., 1999). The

equilibrium concentrations for liquid and solid at the interface, c_L^e, c_S^e, are determined by the

phase diagram and partition coefficient, $k = {}^{c_S^e}/_{c_L^e}$, when using the dilute solution

approximation. A noise factor, $n = 1 + 16 n_0 rg$ has been added to the right-hand term of the

thermodynamic driving force (TDF, Eq. (2.17)) to introduce an element of instability that

encourages secondary growth at the solid/liquid interface of the dendrite, where $n_0 = 0.5$ is the

strength of the noise, r is a random number between -1 and +1, and $g = \phi^2(1 - \phi)^2$ ensures the noise term is only applied within the interface.

In the 3D formulation, the anisotropy parameter, $\eta(\boldsymbol{n})$ can be expressed as Eq. (2.18) (George and Warren, 2002).

$$\eta(\boldsymbol{n}) = (1 - 3\zeta)\left(1 + \frac{4\zeta}{1 - 3\zeta}\frac{\phi_x^4 + \phi_y^4 + \phi_z^4}{|\nabla\phi|^4}\right) \tag{2.18}$$

Here, ϕ_i is defined as $\partial\phi/\partial i$, $\boldsymbol{n}$ is the interface's normal vector, and ζ is the strength of the anisotropy, commonly set at $\zeta = 0.04$. Eq. (2.18) can easily be adjusted for 2D by dropping the z term. For a 2D dendrite with preferred growth direction θ, the ϕ_x, ϕ_y terms in Eq. (2.18) must undergo a vector rotation to ϕ_x', ϕ_y' according to Eq. (2.19).

$$\begin{pmatrix} \phi_x' \\ \phi_y' \end{pmatrix} = \begin{pmatrix} \cos\theta & -\sin\theta \\ \sin\theta & \cos\theta \end{pmatrix}\begin{pmatrix} \phi_x \\ \phi_y \end{pmatrix} \tag{2.19}$$

For 3D growth, the preferred growth direction of each dendrite must be described by three rotational terms, α, β, γ. The rotational matrix becomes

$$\begin{pmatrix} \phi_x' \\ \phi_y' \\ \phi_z' \end{pmatrix} = \begin{pmatrix} \cos\gamma & -\sin\gamma & 0 \\ \sin\gamma & \cos\gamma & 0 \\ 0 & 0 & 1 \end{pmatrix} \cdot \begin{pmatrix} \cos\beta & 0 & \sin\beta \\ 0 & 1 & 0 \\ -\sin\beta & 0 & \cos\beta \end{pmatrix}$$

$$\cdot \begin{pmatrix} 1 & 0 & 0 \\ 0 & \cos\alpha & -\sin\alpha \\ 0 & \sin\alpha & \cos\alpha \end{pmatrix}\begin{pmatrix} \phi_x \\ \phi_y \\ \phi_z \end{pmatrix} \tag{2.20}$$

A list of the model parameters and material parameters is given in Table 2.3. The PF equations are solved with the finite difference technique on a uniform mesh with parallel computing capabilities as illustrated in Figure 2.5.

Table 2.3: Model and material parameters.

Model parameters	Symbol	Value	Unit
Mesh size	Δx, Δy	2.0E-08	m
Time step	Δt	1.0E-08	s
Interface width	2λ	$4\Delta x$	m
Anisotropy strength	δ	0.04	
Crystal symmetry	k	4	

Laser Welding Model

Temperature

Phase field model

Master processor (full domain)
- Read in temperature field
- Set concentration field
- Add nucleation seeds
- Divide domain with slaves
- Send field data to slaves

Time loop

- Periodically receive field data from slaves and output to results file
- Receive field data from slaves
- Postprocessing

Slave processors (subdomains)
- Receive data from master

- Solve PF equation
- Solve diffusion equation
- Share border field data with neighbors
- Periodically send field data to master
- Send field data to slaves

Figure 2.5: PF model solution flow chart.

To help illustrate the differences between 2D and 3D simulations, the 2D PF model was used to compare simulation results of an Al-4wt.% Cu alloy freezing at 905 K, 900 K, and 895 K to the work done by Long et al. (2008) with results shown in Figure 2.6. The simulations in Figure 2.6

were carried out in a 7.5 µm×7.5 µm domain on a 375×375 mesh for 0.333 ms, 0.0173 ms, and

0.0174 ms. The simulations were run on 17 processors and required roughly 2-5 minutes of

computational time. The lengths of these small dendrites are approximately 5 µm-7 µm,

matching very well with the results from Long et al. (2008) in dendrite length, secondary

dendrite arm spacing, and overall morphology.
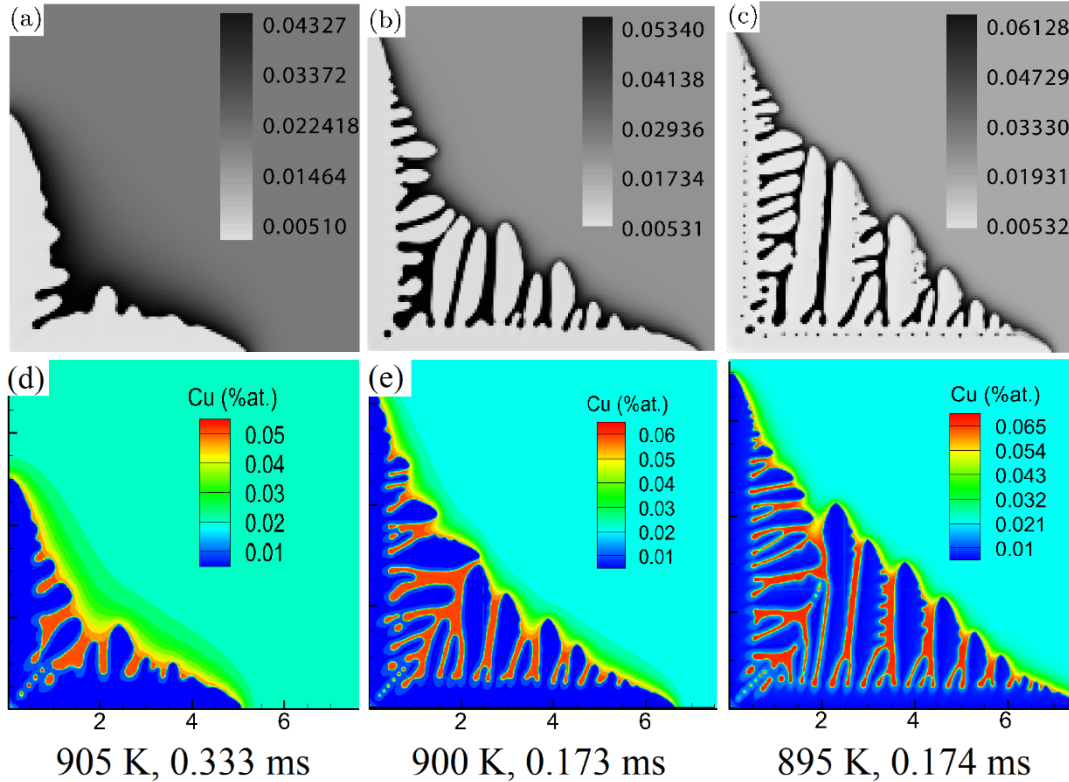
Figure 2.6: The concentration profiles from (Long et al., 2008) shown in (a), (b), and (c) for an
Al-4wt.% Cu alloy compared to results from the 2D PF model shown in (d), (e), and (f). Cu
concentration values shown in at.%

As discussed in Section 1.2.3.1, dendrite morphology between 2D vs. 3D is an important

consideration in predictive modeling. The physical parameters of the following 3D simulation

are the same as those in Figure 2.6: an Al-4wt.% Cu alloy freezing at 900 K in a 15 µm×15

µm×15 µm domain. The simulation was run on a $750 \times 750 \times 750$ mesh for 15,000 time steps on

19 processors requiring roughly 4 days of computational time. The 3D dendrite with the

concentration of copper superimposed on the dendrite surface (defined as $\phi = 0.5$) is shown in Figure 2.7.
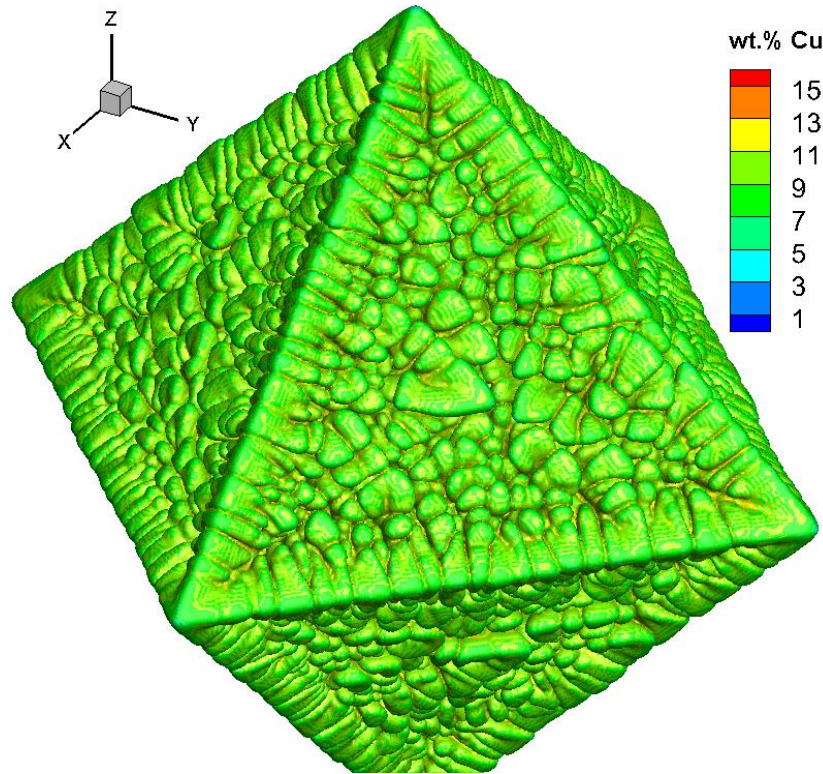
Figure 2.7: 3D dendrite (Al-4wt.% Cu alloy freezing at 900 K for 0.150 ms) showing the interface between solid and liquid. The coloring represents the concentration of copper at the surface in wt.%.

In comparing the cross-section of the 3D dendrite with a 2D dendrite under the same simulation conditions, it is clear that there are some important differences between 2D and 3D simulated dendrite growth. One quadrant of the 3D dendrite is shown in Figure 2.8a along with two 2D planes (Figure 2.8b and Figure 2.8c) of the 3D dendrite, which are compared to the 900 K 2D simulation, Figure 2.8d. Dendrite growth in alloys is governed, primarily, by micro-segregation and solute diffusion. As the solid/liquid interface advances, high-concentration solute is rejected into the liquid because the material can only solidify at low concentrations of solute. In 1D

solidification, the solute only has one direction to diffuse. In 2D solidification the solute can diffuse away within a plane, but pockets of high-concentration solute are easily formed along the interface as shown in Figure 2.6 and Figure 2.8d. However, in 3D the liquid can diffuse in three dimensions, allowing the secondary dendrite arms to grow closer together than in 2D simulations, sometimes even fusing together into larger shapes. An example of these fused regions is illustrated in Figure 2.8b where dendrites arms in the top left and bottom right of the image that were initially separate have fused together after the higher concentration solute was allowed to diffuse in the direction perpendicular to the plane of the image. This perpendicular diffusion, of course, cannot happen in 2D PF simulations where the solute can only diffuse within the plane and can easily get trapped within the interdendritic region, as illustrated in Figure 2.8d. However, 3D diffusion will always occur during solidification processes such as in welding and additive processes. Additionally, at an offset from the center plane of only 0.5 µm, Figure 2.8c shows that the rejected solute that diffused perpendicularly from the fused regions of Figure 2.8b affected the solidification within the regions in Figure 2.8c where that solute diffused to. It is clear from these images that this 2D vs. 3D diffusion phenomenon can strongly affect secondary dendrite arm spacing (SDAS) and solute concentration predictions.

Additionally, because of the 2D vs. 3D diffusion phenomenon, simulated 3D dendrites will grow faster than simulated 2D dendrites because the solute can diffuse away from the interface quicker than in a 2D simulation. This is illustrated here by the difference in simulated solidification time between the 2D simulation (Figure 2.8d, 0.173 ms) and the 3D simulation (Figure 2.8a and Figure 2.8b, 0.150 ms) where both 2D and 3D simulations have the same dendrite length of 6.6 µm.
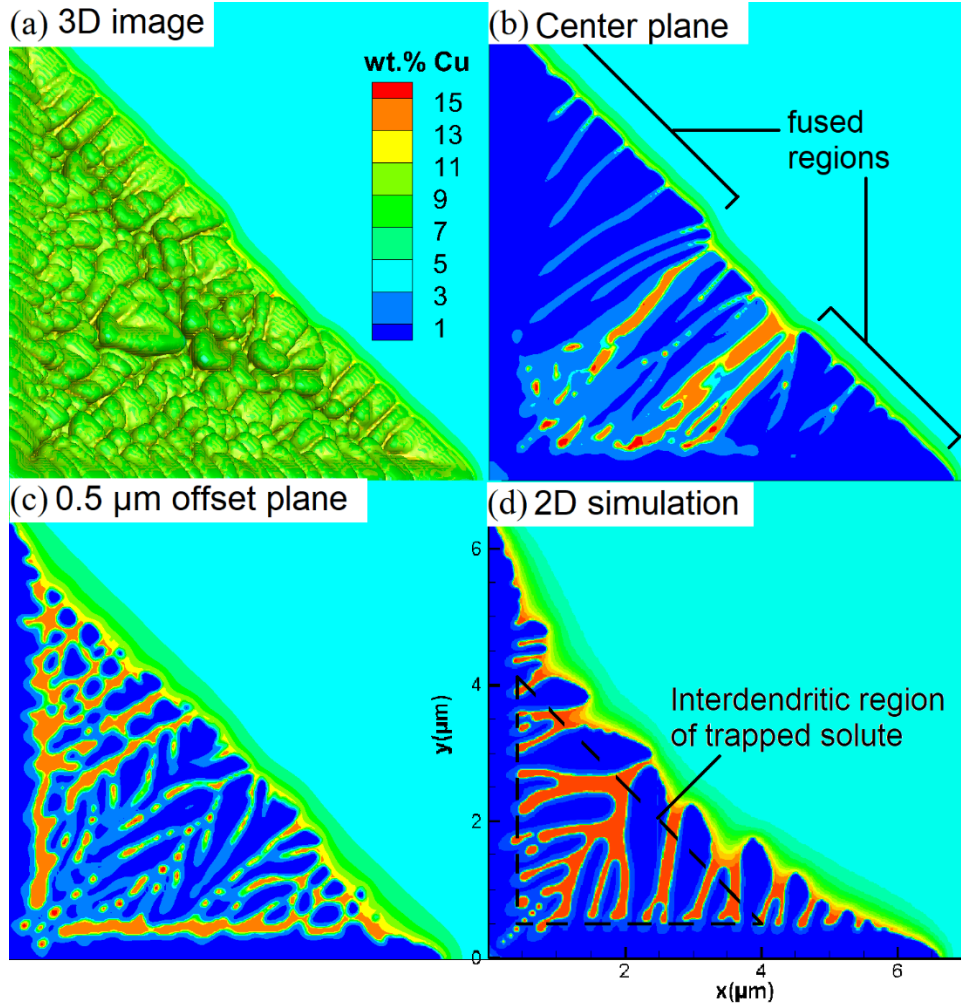
Figure 2.8: (a) 3D image of one quadrant of a 3D dendrite with a (b) 2D plane taken at the center of the dendrite and a (c) 2D plane taken near the center of the dendrite with an offset of 0.5 µm compared to a (d) 2D simulation run with the same parameters.

To show that the differences between 2D and 3D predicted growth are also evident in multi-dendrite simulations, 2D and 3D multi-dendrite simulations were run with the same parameters as in Figure 2.8: an Al-4wt.%Cu alloy freezing at 900 K. The field was seeded with 20 randomly placed seeds with random crystallographic orientations. The 3D simulation results are shown in Figure 2.9 at t = 0.144 ms. After the dendrites grow to fill the entire domain, except for the small high concentration inter-dendritic regions, a 2D cross-section image of the 3D results was taken

and is shown in Figure 2.10 with a comparison to a 2D simulation with all of the same

parameters. By comparing these 2D images, it can be seen that the dendrite morphology is very

different. The primary and secondary dendrite arms of the 2D simulation are much bulkier than

those of the 2D cross section of the 3D simulation. It is clear that the cross-section image is more

representative of an actual microstructure cross-section in overall morphology. Indeed, in

comparing Figure 2.10(a) and Figure 2.10(b), it is clear that the secondary dendrite arm spacing

of the 2D simulation is significantly larger than the secondary dendrite arm spacing of the 2D

cross-section of the 3D multi-dendrite simulation. Therefore, quantitative data such as dendrite

arm spacing and solute concentration values are also more accurate in a 3D simulation than in a

2D simulation.
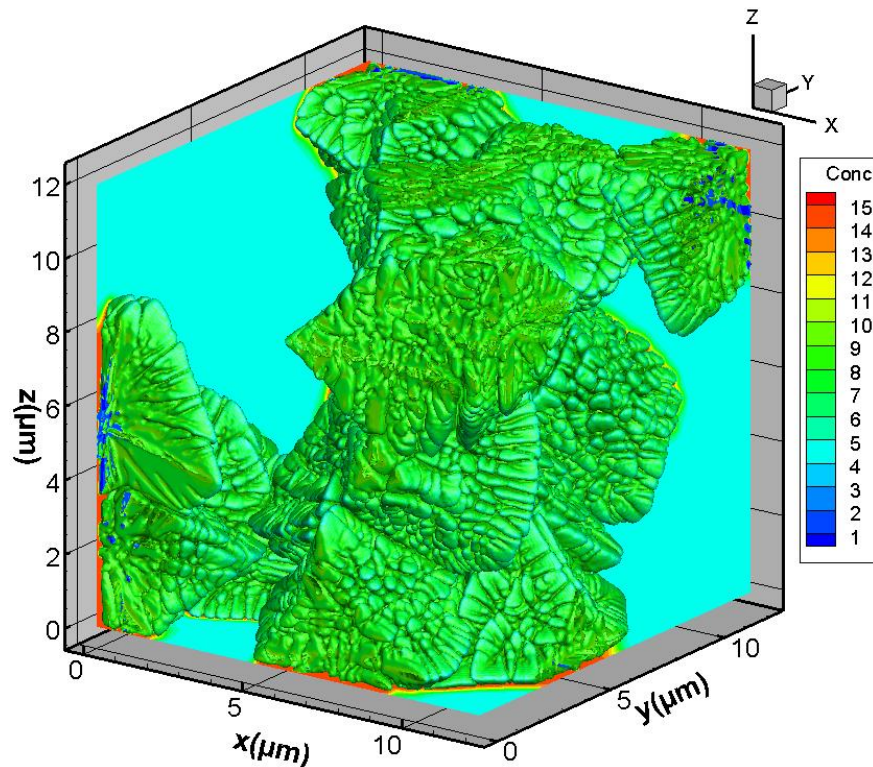
Figure 2.9: 3D multi-dendrite simulation of 10 randomly oriented Al-4wt.% Cu dendrites.
Concentrations shown in wt.%. (A cross section of this simulation at a later time step is shown in
Figure 2.10b.)
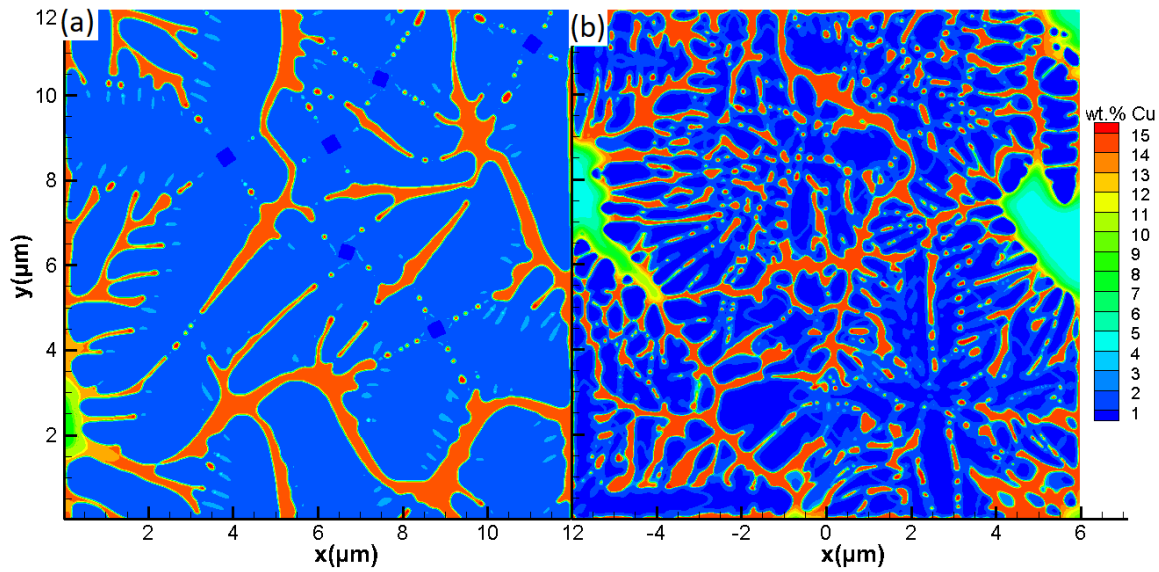
Figure 2.10: (a) 2D multi-dendrite simulation vs. (b) 2D cross-section of a 3D multi-dendrite simulation (shown in Figure 2.9) of Al-4wt.%Cu alloy freezing at 900 K.

2.3.2   CAPF

In this section, CA and PF models are joined in a novel way to take advantage of the strengths and mitigate the weaknesses of each model. While the overall dendrite morphology and temperature and concentration fields are governed by the micro-scale CA model, the detailed growth kinetics and solute concentration balance at the interface is controlled by the PF model. The CA portion of the model was built primarily by Wenda Tan, while the PF portion of the model was built by the present author (Tan et al., 2011a). To minimize computational cost while also accounting for the interface curvature that affects local growth kinetics, the KKS-type phase field equations have been formulated into a 1D polar coordinate system. To ensure accuracy, the model has been validated against an analytical model and other numerical models from literature.

A flowchart, shown in Figure 2.11, helps describe the working of the CAPF model. A 2D slice of the 3D temperature field from a comprehensive thermal model such as the laser deposition model (Wen and Shin, 2010) or the laser welding model (Tan et al., 2013; Tan and Shin, 2014) is provided as input to the CAPF model. The CA portion of the model uses the temperature data to calculate the solute diffusion in the CA domain and determine the initial shape of the solid/liquid interface. Then, for each interface cell in the CA domain, the CA model sends and receives data to and from the PF model, which calculates the growth kinetics along the solid/liquid interface.
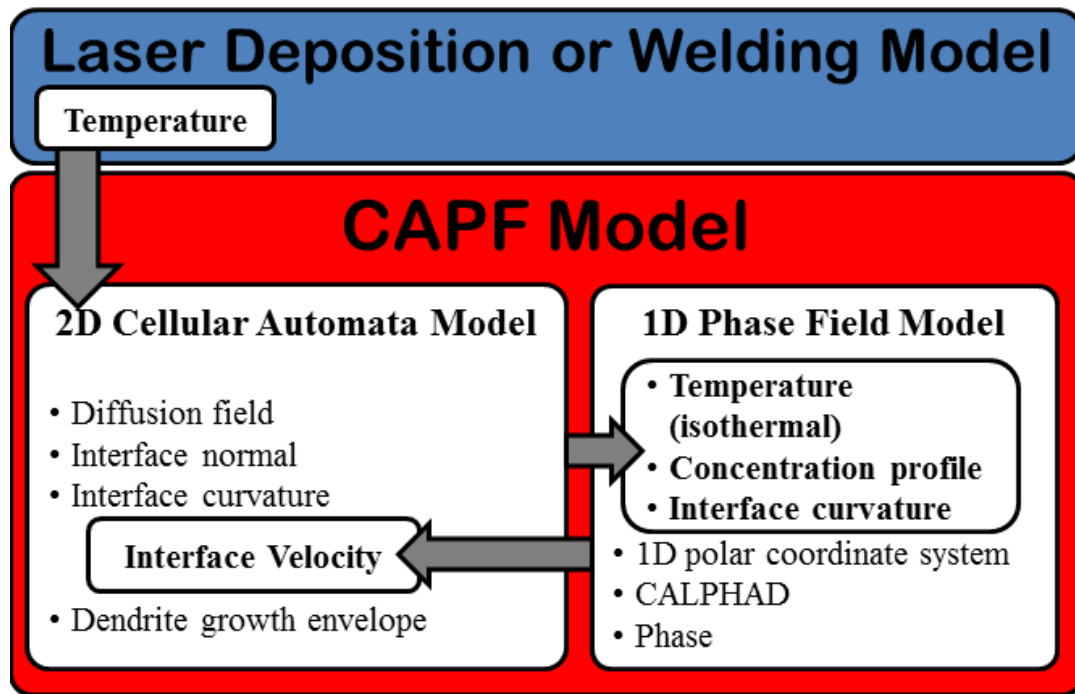
Figure 2.11: Flowchart for the CAPF model.

2.3.2.1 CAPF: Cellular Automata Model

In the CA model, the 2D CA domain is discretized into regular square cells. Each cell can be assigned one of three state variables: liquid, interface, or solid. Other important values needed for calculating the growth kinetics for each cell include solute concentration C for each solute

(two solutes in a ternary alloy), temperature T, a vector β normal to the solid-liquid interface, curvature value K, and crystallographic orientation θ.

Dendrite growth is indicated by increasing numbers of cells changing their states from liquid to interface and then to solid. The cells' state change is dictated by the decentered square algorithm (Beltran-Sanchez and Stefanescu, 2003), in which a nucleus grows with a square envelope whose corner aligns with its crystallographic orientation θ (Figure 2.12a).
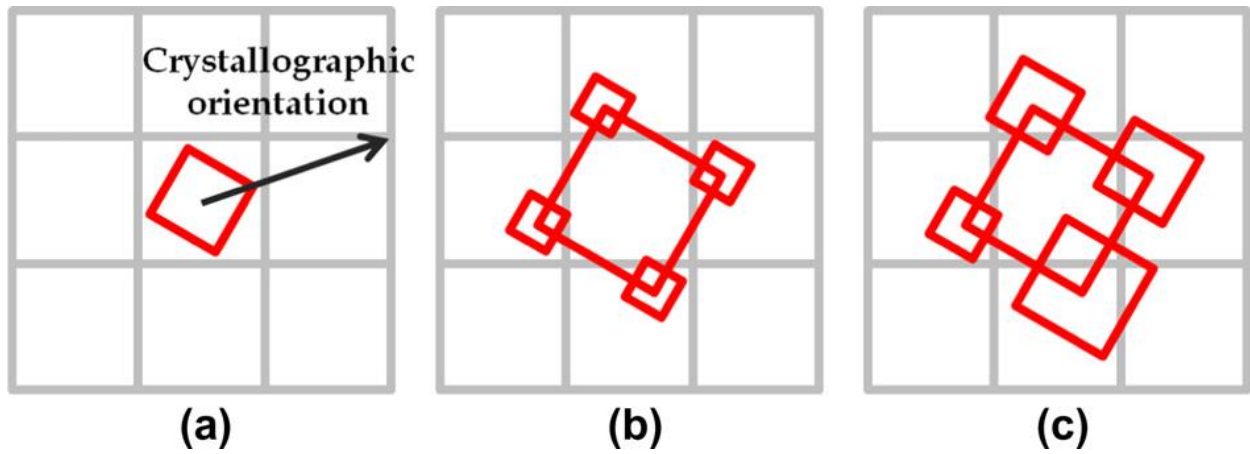
Figure 2.12: Illustration of decentered square algorithm.

The growth envelope will expand according to Eq. 2.21,

$$L = \sum_t V(t_i)\Delta t \tag{2.21}$$

where L is half the length of envelope diagonal, t is the time duration of the interface state of the cell, $V(t_i)$ is the velocity of the solid-liquid interface at time t_i, and Δt is the time step. As the envelope expands during growth, it will contact neighboring cells. If the "contacted" cell is liquid, it will be reassigned as an interface cell. The crystallographic orientation of the "parent" cell will then be passed on to the new interface cells, and the new daughter cell's envelope will

center at the corner of the parent cell's envelope (Figure 2.12b). The child cells will then expand

with their own velocities, which may be different from that of the parent envelope (Figure

2.12c), and will assign other liquid cells as interface cells as they grow sufficiently large. The

solid fraction, f_S, of each cell is governed by Eq. 2.22,

$$f_S = \frac{L}{\Delta x(|\sin\theta| + \cos\theta)}$$

(2.22)

where Δx is the mesh size of the CA model. Once f_S reaches 1, the interface cell is considered

solid and is no longer included in the calculations of the interface cells.

The governing equations and details of the CA model are given by Tan et al. (2011). A brief

explanation will be given here to support the explanation of the PF portion of the model. Two

alloying components must be considered in a ternary system. During solidification at the

interface, a certain amount of each solute is rejected into the liquid while each solute also

diffuses throughout the liquid. This solute diffusion and rejection of each alloying component is

governed by

$$\frac{\partial C_{e,i}}{\partial t} = \nabla \cdot \left(D_{e,i}\nabla C_{e,i}\right) + \frac{\partial f_S}{\partial t}\left(C_{L,i}^I - C_{S,i}^I\right) \quad (i = 1,2)$$

(2.23)

Where $D_{e,i}$ and $C_{e,i}$ are the equivalent diffusion and composition coefficients for liquid,

interface, and solid cells.

The normal vector β at the solid-liquid interface, as shown in Figure 2.13, and the curvature, K,

are needed to calculate the growth kinetics of each interface cell; β for an interface cell is

calculated by using Raghavan's algorithm (2005). As shown in Figure 2.13, a circle is drawn

inside a 7x7 cell area centered on the cell of interest. Point C, the mass center of the solid area

within the circle, is then calculated based on a weighted average of the solid fractions of the cells. The vector between point C and point A is the normal vector β of the interface at cell A.
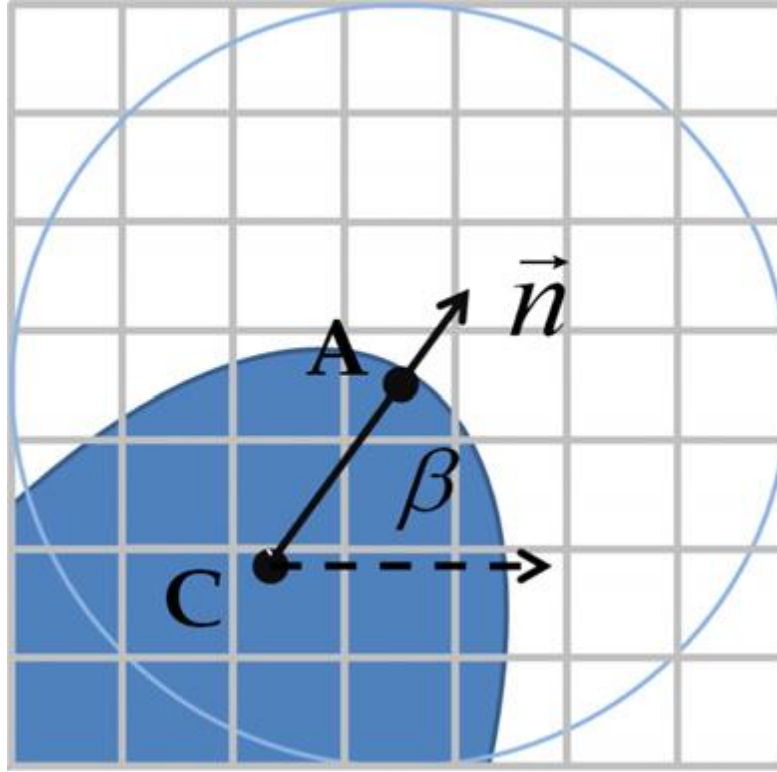
Figure 2.13: Illustration depicting Raghavan's algorithm (Raghavan, 2005) to determine the interface normal using 7x7 grid.

The calculation of the curvature K is based on the work of Martorano et al. (2006). First, as illustrated in Figure 2.14, a line segment is used to approximate the curve of the interface in each interface cell inside a 3x3 cell area centered on the cell of interest. A polynomial is then calculated based on the midpoints of each line segment with the normal vector β as the polynomial's vertical axis, y´, and the origin, point O, at the midpoint of the cell of interest. The curvature can then be calculated from the polynomial.
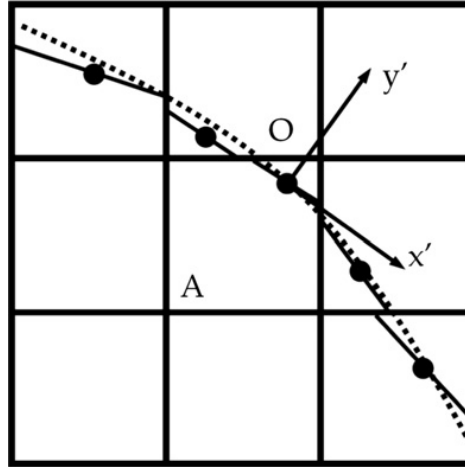
Figure 2.14: Determination of interface curvature.

After the temperature and concentration field are calculated on the CA mesh and the interface

normal vectors and curvatures are known, the growth kinetic values of interface velocity V and

the interface concentrations $C_{L,i}^{I}$ and $C_{S,i}^{I}$ can be calculated from the PF model.

2.3.2.2   CAPF: Phase Field Model

The sole purpose of this phase field model is to provide the cellular automata model with

accurate local growth kinetics along the solid/liquid interface based on local solidification

conditions. It is assumed that the local growth at a given interface cell can be approximated as

1D growth as long as the direction is always normal to the interface. Therefore, a 1D PF model

should be sufficient to calculate the local growth kinetics along the solid/liquid interface.

Similar to Section 2.3.1, the PF equations may be expressed as Eq. 2.24 and Eq. 2.25 (Kim et al.,

1999; Kobayashi et al., 2003; Cha et al., 2005; Zhang et al., 2006; Kim, 2007).

$$\frac{1}{M_\phi}\frac{\partial \phi}{\partial t} = \varepsilon^2 \nabla^2 \phi - \frac{\partial f}{\partial \phi} \tag{2.24}$$

$$\frac{\partial C_i}{\partial t} = \nabla \cdot \sum_j^n \left(D_{ij}\nabla C_j\right) + \nabla \cdot \sum_j^n \left(M_{ij} \frac{\partial^2 f}{\partial C_j\, \partial \phi} \nabla \phi\right) \qquad (2.25)$$

Here, the order parameter of the phase field is represented by ϕ, M_ϕ is the phase field mobility, ε is the gradient energy coefficient, and f is the free energy. The concentration of each component i of the alloy is C_i, while D_{ij} and M_{ij} are the (i, j)th components of the material diffusion and mobility matrices, respectively.

If this system is solved in 1D, it would simulate the solidification of a planar interface. Yet locally, at the interface, the curvature of a dendrite strongly affects the velocity of the solidification interface. For example, an interface with a positive curvature, such as the tip of a dendrite, will solidify much faster than a planar interface since the rejected solute can diffuse to the sides of the dendrite tip. On the other hand, an interface with a negative curvature such as the area near the base of a dendrite arm will solidify much slower than a planar interface since the ejected solute cannot diffuse away and is trapped by an inward-curving interface. A 1D planar PF model would underestimate the growth near the tip of a dendrite and overestimate the growth near the root of the dendrites.

Therefore, the 1D PF model has been re-formulated, as shown in Eq. 2.26 and Eq. 2.27, into a polar coordinate system with radius r (taken from the curvature value as calculated in Section 2.3.2.1).

$$\frac{1}{M_\phi} \frac{\partial \phi}{\partial t} = \frac{1}{r} \frac{\partial}{\partial r}\left(\varepsilon^2 r \frac{\partial \phi}{\partial r}\right) - \frac{\partial f}{\partial \phi} \qquad (2.26)$$

$$\frac{\partial C_i}{\partial t} = \frac{1}{r}\frac{\partial}{\partial r}\left(r\sum_{j}^{n}\left(D_{ij}\frac{\partial C_i}{\partial r}\right)\right) + \frac{1}{r}\frac{\partial}{\partial r}\left(r\sum_{j}^{n}\left(M_{ij}\frac{\partial^2 f}{\partial C_j\partial\phi}\right)\frac{\partial\phi}{\partial r}\right) \qquad (2.27)$$

The effect of interface curvature is incorporated into the model through this 1D polar formulation. By using this formulation, the growth kinetics of the CAPF model assumes a unique circular shape for each interface cell, depending on the local shape of the dendrite. The solidification velocity of the interface is then dependent on the local curvature and the concentration gradient(s) of the solute(s).

Following the formulation of the KKS model (Cha et al., 2005), the equilibrium state of a ternary alloy in the interface region is defined as shown in Eq. 2.28 and Eq. 2.29.

$$C_i = f(\phi, C_1, C_2, T)C^e_{S,i} + (1 - h(\phi))C^e_{L,i} \qquad (i = 1,2) \qquad (2.28)$$

$$\frac{\partial}{\partial C^e_{L,i}} f^L\left(T, C^e_{L,1}, C^e_{L,2}\right) = \frac{\partial}{\partial C^e_{S,i}} f^S\left(T, C^e_{S,1}, C^e_{S,2}\right) = \mu_i \qquad (2.29)$$

Here, $C^e_{S,i}$ and $C^e_{L,i}$ are the solid and liquid concentrations of alloy components $i = 1$ or 2, T is temperature, and $h(\phi) = \phi^3(6\phi^2 - 15\phi + 10)$ is the interpolating function. Additionally, μ_i is defined as the "chemical potential" in the KKS model and it is the slope of the tangent line to the Gibbs energy curve (Kim, 2007). Eq. 2.28 and Eq. 2.29 can be solved with known ϕ, C_1, C_2, and T, and the equilibrium parameters of $C^e_{S,1}$, $C^e_{S,2}$, $C^e_{L,1}$, $C^e_{L,2}$, f^S and f^L can be found. The function $f(\phi, C_1, C_2, T)$ is the free energy density function defined in Eq. 2.30,

$$f(\phi, C_1, C_2, T) = g(\phi)W + f^S\left(C^e_{S,1}, C^e_{S,2}, T\right)$$
$$+ h(\phi)\left[f^L\left(C^e_{L,1}, C^e_{L,2}, T\right) - f^S\left(C^e_{S,1}, C^e_{S,2}, T\right)\right] \qquad (2.30)$$

where W is the height of the energy penalty at the interface, and $g(\phi) = \phi^2(1-\phi)^2$ is the double well function. The source term on the right-hand side of Eq. 2.26 can be written as

$$\frac{\partial f}{\partial \phi} = W\frac{\partial g}{\partial \phi} + \left[f^S - f^L + \sum_i (C^e_{S,i} - C^e_{L,i})\mu_i\right]\frac{\partial h}{\partial \phi} \tag{2.31}$$

In Eq. 2.31, the term in brackets is called the thermodynamic driving force (TDF), and the chemical potential, μ_i, is calculated from the solution of Eq. 2.28 and Eq. 2.29.

The phase field mobility, M_ϕ, is calculated in Eq. 2.32 and 2.33 (Zhang et al., 2006)

$$M_\phi = \frac{\sigma\sqrt{2W}}{\varepsilon^3\zeta} \tag{2.32}$$

$$\zeta = -\sum_{j=1}^{n}\left(C^e_{L,j} - C^e_{S,j}\right)\sum_{k=1}^{n}\left(C^e_{L,k} - C^e_{S,k}\right)\int_1^0 h`(\phi_0)\int_{\phi_0}^0 B^e_{jk}\frac{1-h(\phi)}{\phi(1-\phi)}d\phi d\phi_0 \tag{2.33}$$

where ε is the gradient energy coefficient, σ is the interface energy, and B^e_{jk} is a component of the inverse matrix of the material's mobility matrix, $\mathbf{M}$, at equilibrium. The components, M_{ij}, in the material's mobility matrix, $\mathbf{M}$, are calculated from the diffusivity matrix, $\mathbf{D}$, as shown in Eq. 2.34.

$$D_{kj} = \sum_{i=1}^{n}\left(M_{ki}\frac{\partial^2 f}{\partial C_i \partial C_j}\right) \tag{2.34}$$

The gradient energy coefficient, ε, and the height of the energy penalty for the interface, W, are calculated according to Equations 2.35 and 2.36,

$$\varepsilon^2 = \frac{3\sigma 2\lambda}{\alpha} \tag{2.35}$$

$$W = \frac{6\sigma\alpha}{2\lambda} \tag{2.36}$$

where σ is the interface energy, 2λ is the double width of the interface, and α is a constant which depends on how the interface is defined.

For multicomponent alloys, more than one phase may form upon solidification. To determine which phases will form, the PF model is linked to a CALPHAD database which calculates the Gibb's energy of the system.

The PF model needs the interface curvature, concentration distribution for each solute in the alloy, and the temperature to replicate the local solidification conditions in order to calculate the growth kinetics for a CA interface cell. For diffusion-controlled dendrite growth, the concentration distribution is the strongest factor and can be accurately described with a 1D concentration profile in the PF model. A number of points along the interface cell's normal vector are interpolated from the CA model's concentration fields onto the PF model's 1D concentration profile, as shown in Figure 2.15. For example, the solute concentrations of point 1 is interpolated from the values of cells B, C, D and E. A typical cell size for the CA model's mesh is 0.5 μm, while a typical cell size in the 1D PF model is 0.25 μm. The 1D concentration profile along the vector is described by Eq. 2.37.

$$C_i(x) = C_{\infty,i} + \left(C_{L,i}^I - C_{\infty,i}\right)\exp(-A_i x) \tag{2.37}$$

Here, $C_{L,i}^I$ is the concentration at the interface, $C_{\infty,i}$ is the concentration far from the interface, A_i is a variable that defines the exponential strength of the concentration profile, and x is the

distance from the interface into the liquid in the normal direction. The concentration value at the

interface, $C_{L,i}^I$, is known from the last CA time step, the concentration value far from the

interface, $C_{\infty,i}$, is found at a distance into the melt far enough away from the interface that the

value does not change significantly, and A_i is determined from the concentration values of the

1D profile. The interface concentration, $C_{L,i}^I$, and A_i are then used by the PF model, along with

the local temperature and curvature, to determine local growth velocity and equilibrium

concentrations at the interface.
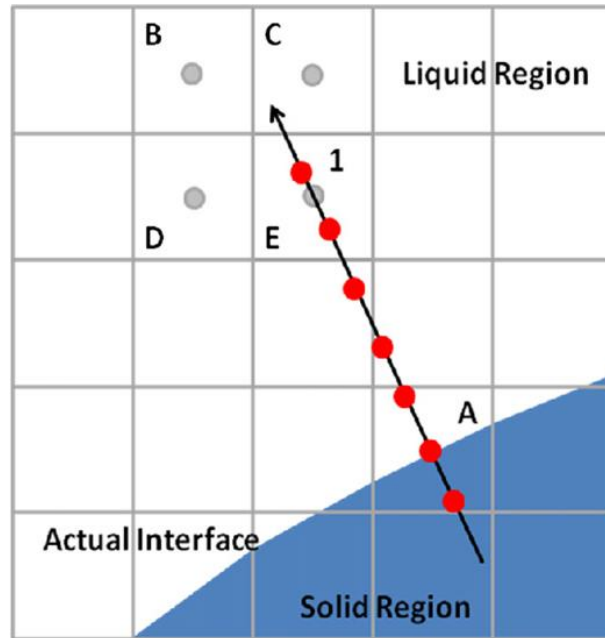
Figure 2.15: 1D concentration profile along Cell A's normal vector is interpolated from the CA model to the PF model.

As an example, a graph of the 1D concentration profiles for two solutes (copper and magnesium)

in a ternary Al-Cu-Mg alloy as calculated by Eq. 2.37, is shown in Figure 2.16. To correctly set

up the PF model, the mid-point of the PF interface ($\phi = 0.5$) must be positioned at $r = 1/K$ in

the polar coordinate domain. The temperature used in the PF model is assumed to be isothermal

at temperature T of the interface cell. The isothermal assumption is valid because the variation in temperature along the normal vector is much smaller than the variation in concentration(s) across the distance the interface advances during one CA time step.
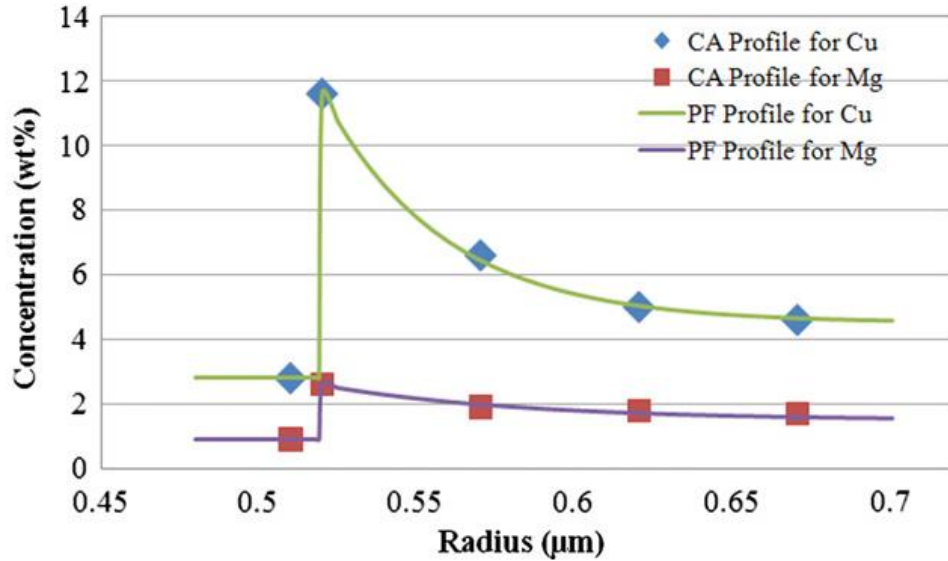
Figure 2.16: 1D concentration profiles for copper and magnesium, interpolated from CA, as a function of radial distance normal to the solidification interface.

With the values of temperature and curvature and the concentration profile provided by the CA model, the PF model can precisely predict the progression of the solidification interface. This velocity of the PF solidification interface is the interface velocity, $V(t_i)$, needed in the CA model (Eq. 2.21) and is the sole purpose of the PF model. A number of time steps are required for the PF model to reach convergence from the initial concentration profile as given by the CA model as illustrated in Figure 2.16 to the converged concentration profile shown in Figure 2.17. Once convergence has been reached, the interface velocity of the PF model is given to the CA model, along with values of the solid and liquid interface concentrations $C_{L,i}^I$ and $C_{S,i}^I$ taken from the PF model's converged 1D concentration profile. Continuing the example of a ternary Al-Cu-Mg

alloy, the PF model's converged concentration profiles of copper and magnesium are shown in

Figure 2.17. The highest concentration values (the peaks in each concentration curve) are

selected as the liquid concentrations $C_{L,Cu}^I$ and $C_{L,Mg}^I$, while the lowest values to the left of the

peaks are selected as the solid concentrations $C_{S,Cu}^I$ and $C_{S,Mg}^I$ for the next CA time step.

However, if the partition coefficient of a given component is greater than unity, the liquid and

solid concentrations are reversed.
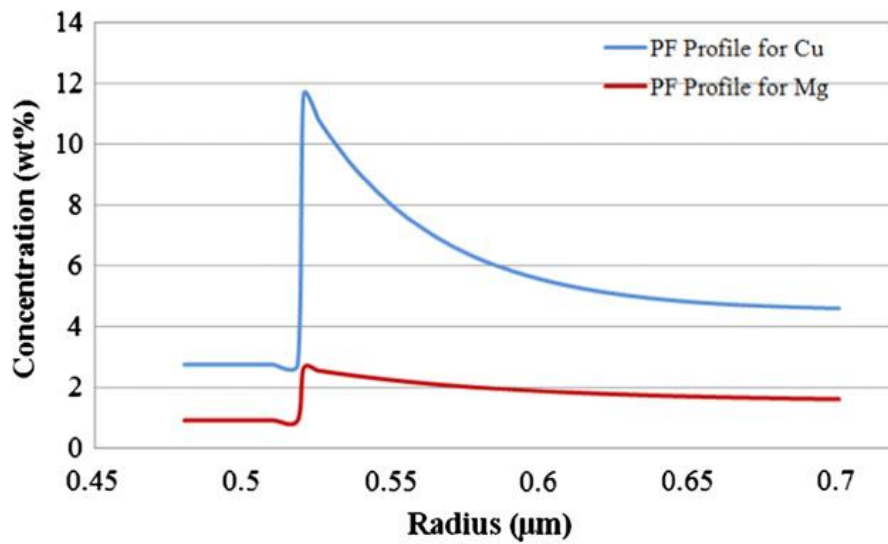
Figure 2.17: Converged concentration profile from PF model.

2.3.2.3 Validation

For model validation, simulations have been performed to predict the dendrite growth of an

aluminum-copper (Al—4 wt% Cu) binary alloy at different undercoolings. At steady state, the

predicted values of tip radius, tip velocity, and copper concentration at the tip are compared to an

analytical model (the Lipton–Glicksman–Kurz (LGK) model) (Lipton et al., 1984). The LGK

model predicts the free growth velocity of a simple needle dendrite in a binary alloy at a given

undercooling temperature. In this simulation, the CA domain is set to 200 µm × 200 µm with a

mesh size of 0.1 µm and the CA time step as estimated by Eq. 2.38 (Beltran-Sanchez and Stefanescu, 2004).

$$\Delta t = \frac{1}{4} \min\left(\frac{\Delta x}{V}, \frac{\Delta x^2}{D_{L,i}}, \frac{\Delta x^2}{D_{S,i}}\right) \tag{2.38}$$

Here, Δx is the CA mesh size and V is the interface velocity. The entire domain is kept isothermal at a constant undercooling and the initial solute concentration is set to be 4 wt.% Cu. At the center of the domain, a seed was planted with crystallographic orientation of $0°$ with respect to the horizontal. The CAPF model simulates the growth of the dendrite and updates the dendrite tip velocity every 50 CA time steps.

The predicted dendrite morphologies and solute distributions for different temperatures of 916 K, 914 K, and 912 K are shown in Figure 2.18. The dendrite growth velocity increases as the temperature decreases. Note that the primary dendrite arms are thinner, and the side branching is stronger at lower temperatures. For the case of lower temperature 912 K, the concentration gradient of the liquid near the interface is steeper than for higher temperatures. Once steady state was reached, the tip velocities, tip radii and liquid interface concentrations C_L^I were measured for the three cases and are recorded in Table 2.4. A comparison between the CA model's results and the LGK analytical model is given in Figure 2.19, showing reasonable agreement. Even though the CAPF model predicts lower values of C_L^I than the analytical result, the CAPF model is more accurate. Because of its use of a linearized equilibrium phase diagram, the analytical model neglects the solute trapping phenomenon and overpredicts the concentration value, C_L^I. Thus, the lower C_L^I values as predicted by the CAPF model are more accurate than the analytical model.
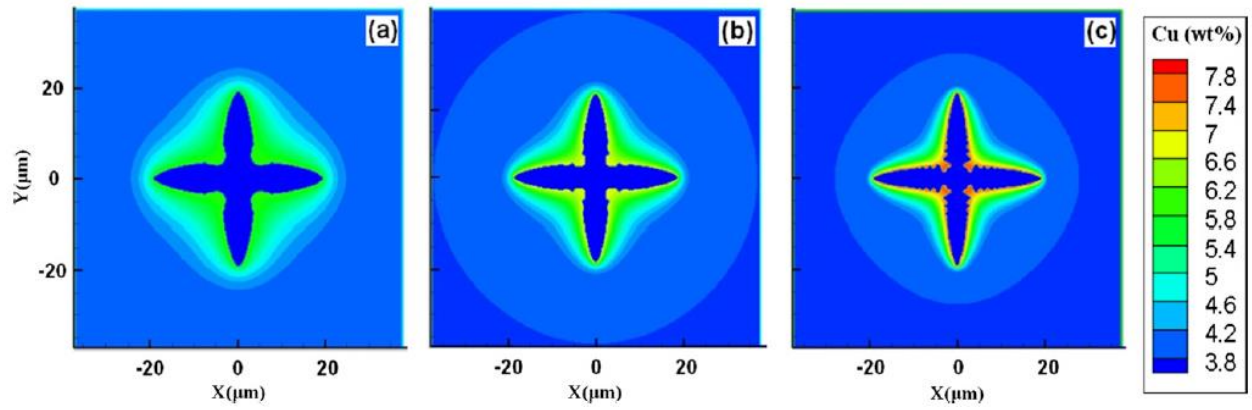
Figure 2.18: Predicted dendrite morphologies and solute distributions of Al—4wt% Cu binary alloy: (a) 916 K; (b) 914 K; and (c) 912 K.

Table 2.4: Predicted steady-state parameters at different temperatures.

Temperature (K)	Tip velocity (m/s)	Tip radius (10^{-6} m)	C_L^I (wt.% Cu)
916	6.10E-04	1.032	5.75
914	2.11E-03	0.406	6.2
912	4.67E-03	0.285	6.65
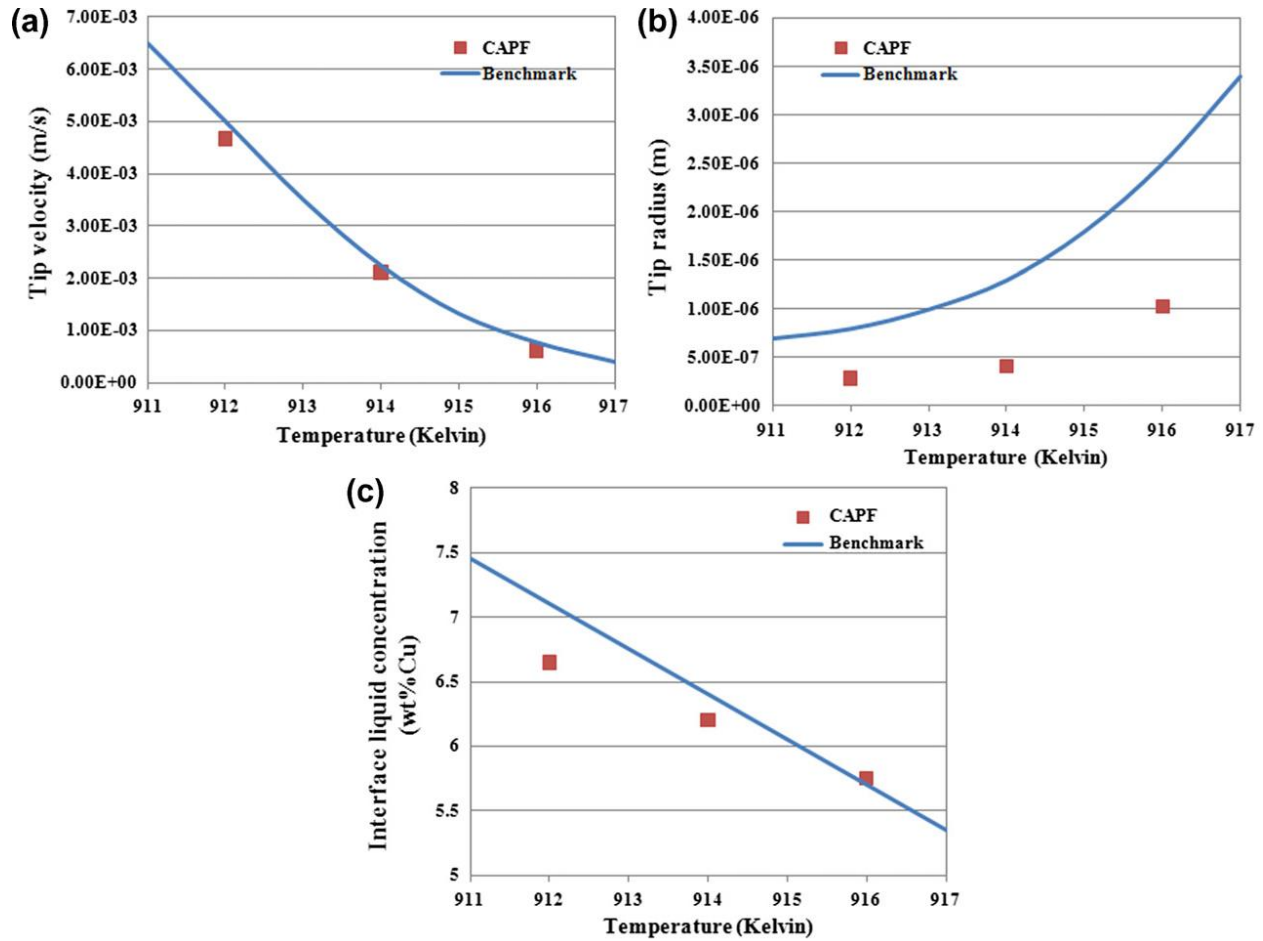
Figure 2.19: Comparisons between LGK analytical model results and CAPF model results: (a) tip velocity; (b) tip curvature; and (c) interface concentration.

The CAPF model is further validated by reproducing PF results of Long et al. (2008), of an Al–4.5 wt.% Cu binary alloy solidifying at 900 K for 0.173 ms. A comparison showing reasonable agreement between two predicted concentrations fields is shown in Figure 2.20: one from Long et al. (2008) and one from the CAPF model. The computational costs, however, are vastly different: the PF model cost is estimated at 200 CPU hours (from data given by Cha et al. (2005)), compared to 0.25 CPU hours for the CAPF model. These results show that the CAPF model has a much lower computational cost than a traditional PF model.
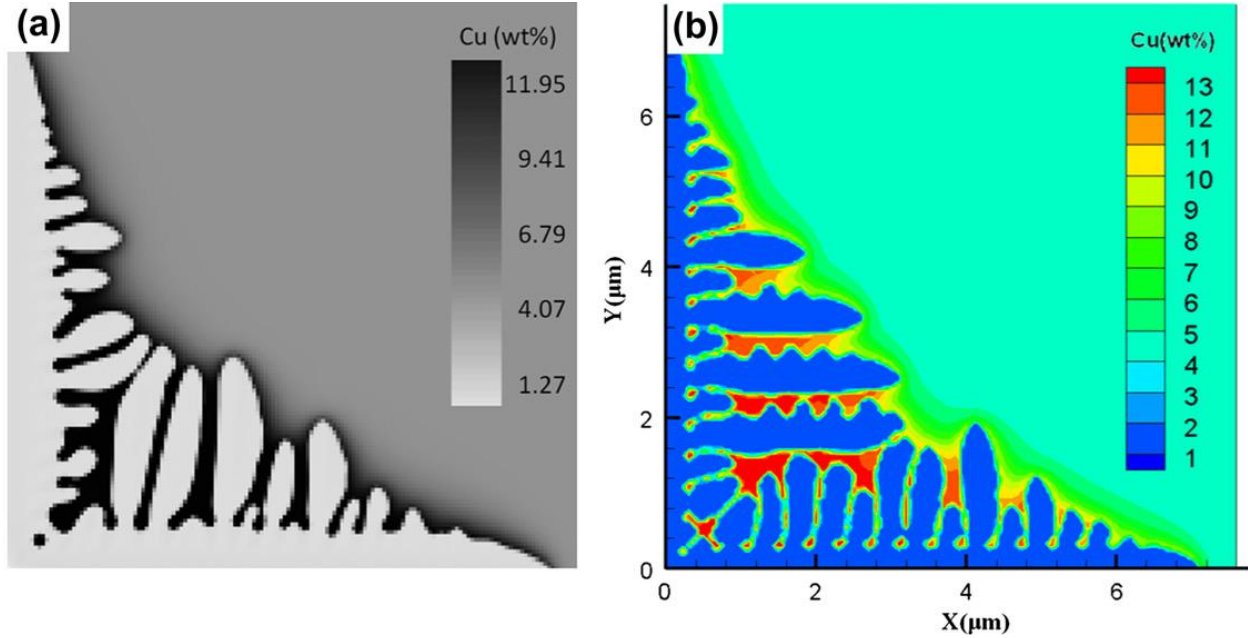
Figure 2.20: Predicted concentration fields between (a) a benchmark PF result and (b) CAPF result for a Al–4.5Cu wt.% binary alloy at 900 K after 0.173 ms.

The computational efficiency of the CAPF model is a result of how the two are coupled. The CA model is more efficient than the PF model in tracking the solute redistribution over the whole domain because the CA model can use a much coarser mesh and larger time step than the PF model. The PF model's advantage (accurate growth kinetics based on Gibb's free energy, which is computationally expensive) is only applied where it is needed at the solid-liquid interface. For this case, the CA model used a mesh size of 0.05 µm (5 times larger than the PF model) and a time step of 5E-8 s (50 times larger than the PF model).

The CAPF model's vast improvement of computational efficiency over typical PF models makes it practical to simulate larger domains and time scales. The domain size of a typical PF simulation is limited about 10 µm and a time scale of less than 0.01 s (Cha et al., 2001; Ode et al., 2001; Qin et al., 2005; Zhang et al., 2006; Long et al., 2008). However, the CAPF model has successfully simulated a casting process with a 900 µm × 900 µm domain for 140 s (Tan et al.,

2011a), a laser welding process with a 40 µm × 25 µm domain for 0.05 s (Tan et al., 2011a), and

a laser cladding process with a 400 µm × 500 µm domain for 2.0 s (Tan et al., 2012), all of

which would not be computationally feasible for a traditional PF model.

3. APPLICATIONS

Two applications are presented here that validate and demonstrate the use of the residual stress model. The first application shows the computational simulation and experimental results of single-track laser hardening of a block of AISI 4140 steel. The temperature field is predicted by a prismatic thermal model and the residual stress model is applied without considering multi-track tempering or melting and solidification. After performing laser hardening with a direct diode laser, the solid phase transformation model is validated via microstructure analysis and hardness measurements while the residual stress model is validated via X-ray diffraction (XRD) measurements (Bailey et al., 2009).

The second application shows the computational simulation and experimental results of multi-track and multi-layer laser direct deposition of H13 tool steel powder on an H13 tool steel substrate. Laser direct deposition experiments are performed with an Optomec LENS 750 system and optimal deposition parameters are determined via experimentation. To show the applicability of laser direct deposition on industrial tooling, repair and remanufacturing are demonstrated on two different die-casting inserts. The temperature field is predicted via a laser cladding model developed by Wen and Shin (2011) and the residual stress model is applied with consideration of multi-track tempering and melting and resolidification. The solid phase transformation model is validated via microstructure analysis and hardness measurements while the residual stress model is validated via X-ray diffraction (XRD) measurements. Ultimate tensile strength measurements were also performed on the deposited material.

3.1 Laser Hardening

A rectangular block of AISI 4140 steel measuring 50x50x18 mm was laser hardened using a
Nuvonyx 4 kW high power direct diode laser, as shown in Figure 3.1. This laser has a
rectangular beam profile with a size of 12x8 mm and was set to a power of 1 kW and traverse
speed of 2 mm/s. The laser track coincides with the center of the workpiece, while the shorter
axis of the beam profile is aligned with the direction of laser travel, as shown in Figure 3.1. A
constant absorptivity of 0.68, determined by a calibration experiment (Touloukian et al., 1974),
is used for the simulation. The initial temperature of the workpiece is 27 ℃.
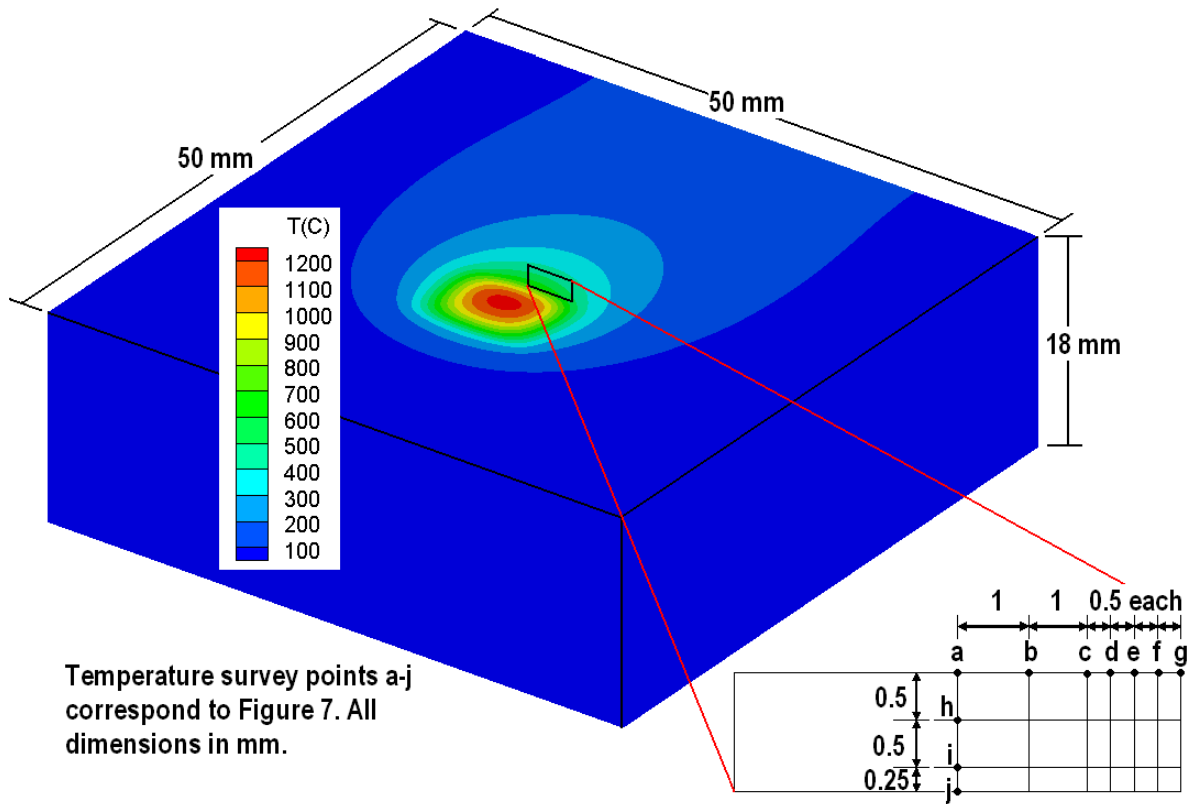
Figure 3.1: Schematic of laser hardening process showing the temperature survey cross-section
and the location of each survey point.

As mentioned in Section 2.2, a Johnson-Cook hardening model was used to model the plastic

strain during laser hardening. A list of Johnson-Cook coefficients for AISI 4140 steel

interpolated from data given in the High Performance Alloy Database by CINDAS (Shahinian et

al., 1961) are shown here in Table 3.1. The elastic strain is dependent on the material's Young's

modulus and Poisson's ratio, as functions of temperature, and both are shown in Figure 3.2.

Table 3.1: Johnson-Cook hardening model coefficients for AISI 4140 Steel.

A	B	n	m	T_{melt}
224.9 MPa	228.1 MPa	0.28	1.3	1700 K
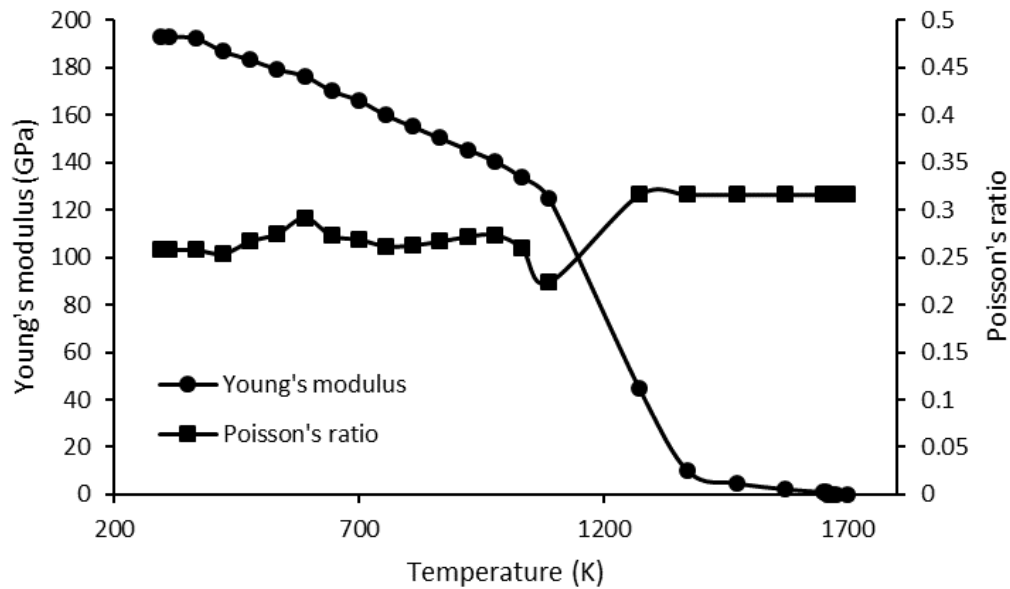
Figure 3.2: Young's modulus and Poisson's ratio for AISI 4140 steel as functions of temperature (Shahinian et al., 1961).

The temperature histories of 10 survey points, shown in Figure 3.1, were recorded. As shown in

Figure 3.3, the temperatures at all of these survey points go above the A1 eutectoid temperature

where the pearlite transforms to austenite. All points, except j and g, are also heated above A3

austenization point, where the remaining ferrite also transforms to austenite. At this point in time, the material at j and g will have a mixed microstructure of austenite and ferrite, depending on the temperature and carbon diffusion. Table 3.2 shows that the temperature at all survey points drops from the A1 eutectoid temperature, 727 ºC, to the martensite start temperature Tm-start, 330 ºC, within 3.0 seconds. This cooling rate ensures missing the "nose" of the TTT diagram, as can be seen in Figure 2.3. Consequently, the final microstructure at these subsections will be martensite with limited retained austenite. The temperature at survey points j and g drops sufficiently fast to avoid bainite formation. However, since the temperature at these points did not peak over the A3 austenization temperature and not all ferrite transformed into austenite, there will be residual ferrite that will soften the material at these points.
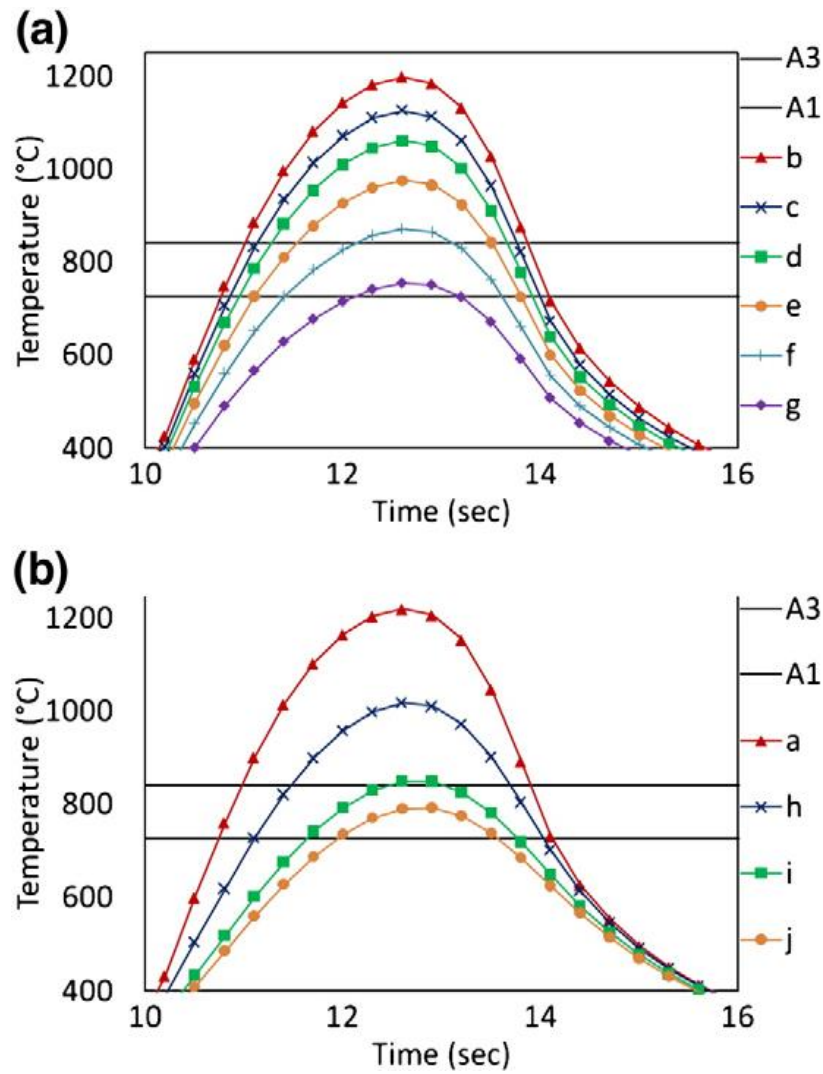
Figure 3.3: Temperature history of various points shown in Figure 3.1 relative to the A3 austenization temperature and the A1 eutectoid temperature.

Table 3.2: Time taken for each survey point to cool from the A1 eutectoid temperature, 727 °C, to the Tm-start martensite start temperature, 330 °C.

Survey point	a	b	c	d	e	f	g	h	i	j
Cooling time* (s)	2.4	2.5	2.4	2.3	2.4	2.3	2.6	2.5	2.7	2.9

*from 727°C to 330°C

3.1.1 Hardness Prediction

Figure 3.4 shows a predicted hardness profile taken from the center of the workpiece. The region

consisting of only martensite and limited retained austenite has a high hardness value of 712

Vickers. The transition region between the bulk material and martensitic region goes through

partial austenite transformation. From calculations made using Equations 2.2 and 2.7, it has a

lower hardness between that of martensite (712 Vickers) and the bulk material (250 Vickers).
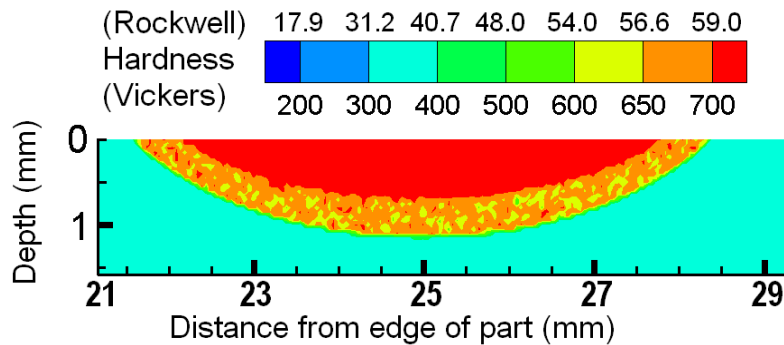
Figure 3.4: Hardness profile of the survey area.

Figure 3.5 shows the optical micrographs obtained at different regions in the heat-affected zone

(HAZ) of the cross-section. The polished specimen was chemically etched with 2% Nital for 40

seconds in order to obtain these micrographs. Due to the high cooling rates (shown in Table 3.2),

homogeneous martensite is obtained through most of the hardened region (Figure 3.5a, needle-

like structure). The cooling rates closer to the HAZ boundary are slower. Hence, this region

(Figure 3.5b) essentially has coarser and inhomogeneous martensite, although the hardness value

is similar. The transition region (Figure 3.5c) between the martensite and the unaffected material

is softer, due to residual ferrite that did not have time to transform into austenite. The material

outside of the HAZ (Figure 3.5d) remains unaffected by heat. As shown, it consists of pearlite

(darker phase) and α-ferrite (lighter phase).
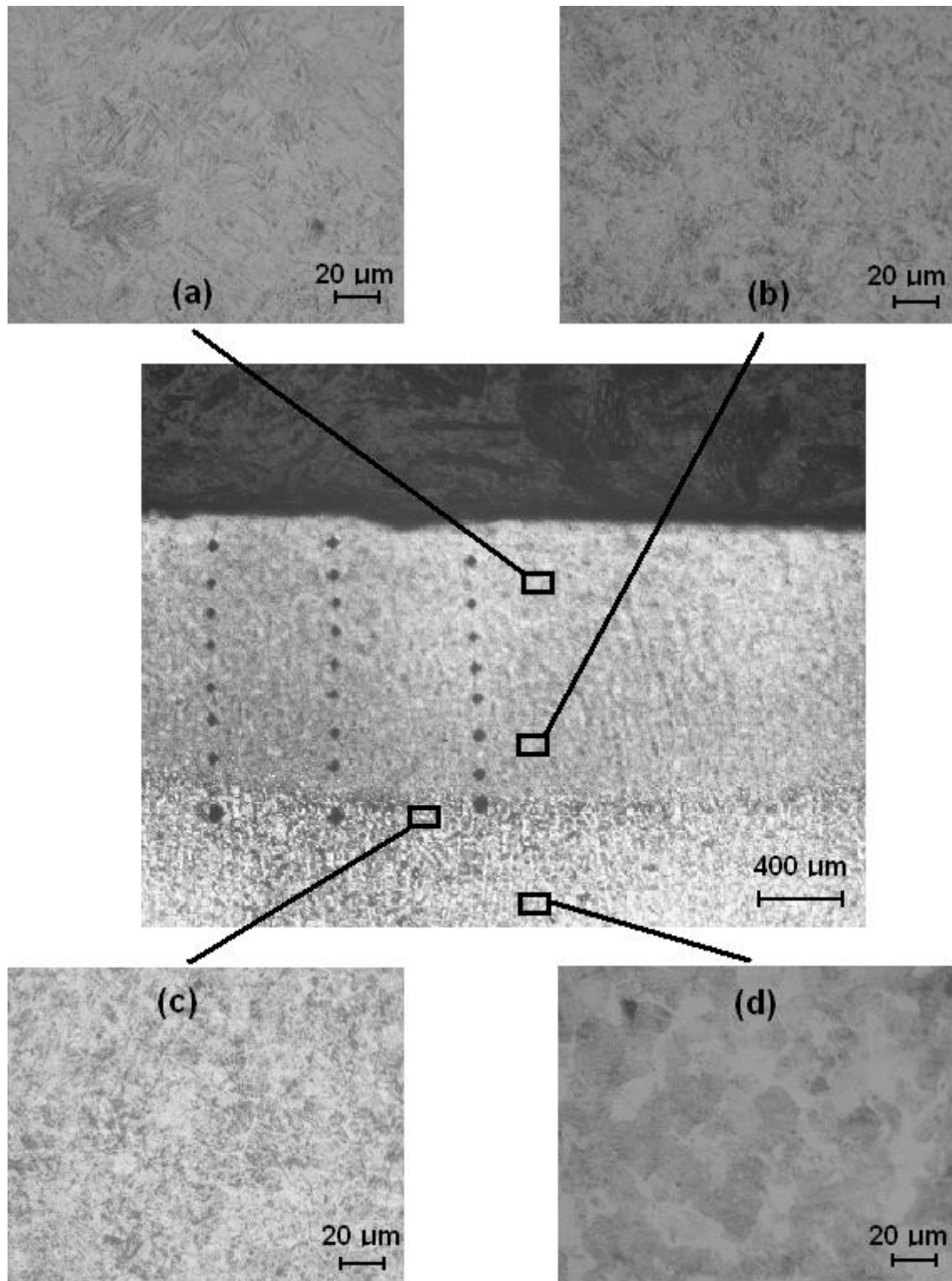
Figure 3.5: Microstructure of the laser hardened AISI 4140 steel sample. (a) Homogeneous martensite, (b) Heterogeneous martensite, (c) Partial martensite, (d) Unaffected base material (pearlite and ferrite)

The microhardness in the HAZ was measured with a Vickers microhardness tester (1 kgf load and a dwell time of 20 s). Figure 3.6 shows the comparison of predicted hardness with measured hardness into the depth at the center of the workpiece, giving a case depth of 1.20 mm. The predicted results are in excellent agreement with the microhardness measurements.
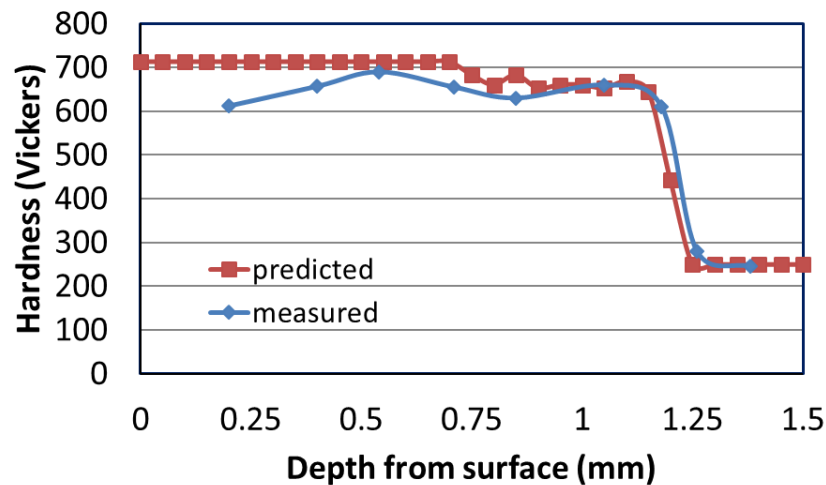
Figure 3.6: Comparison of predicted and measured case depth at the center of the workpiece.

3.1.2   Residual Stress Prediction

From the solid-state phase transformation model, phase fractions of pearlite, ferrite, austenite, and martensite were obtained at each time step. The phase fractions were then accessed by the residual stress model which calculated the thermal strains, volumetric dilatation strains, and transformation-induced plasticity strains at each time step of the stress model.

Residual stresses were measured using the X-ray diffraction method at two points on the surface of the workpiece: one measurement at the center of the laser track and one measurement 2.5 mm

away from the center of the laser track. Residual stress values were predicted across the face of

the workpiece and into the depth of the workpiece as shown in Figure 3.7. Figure 3.8 and Figure

3.9 show predicted residual stress variation along the surface and depth of the cross-section,

respectively. Predicted stress values agree very well with measured stress values.
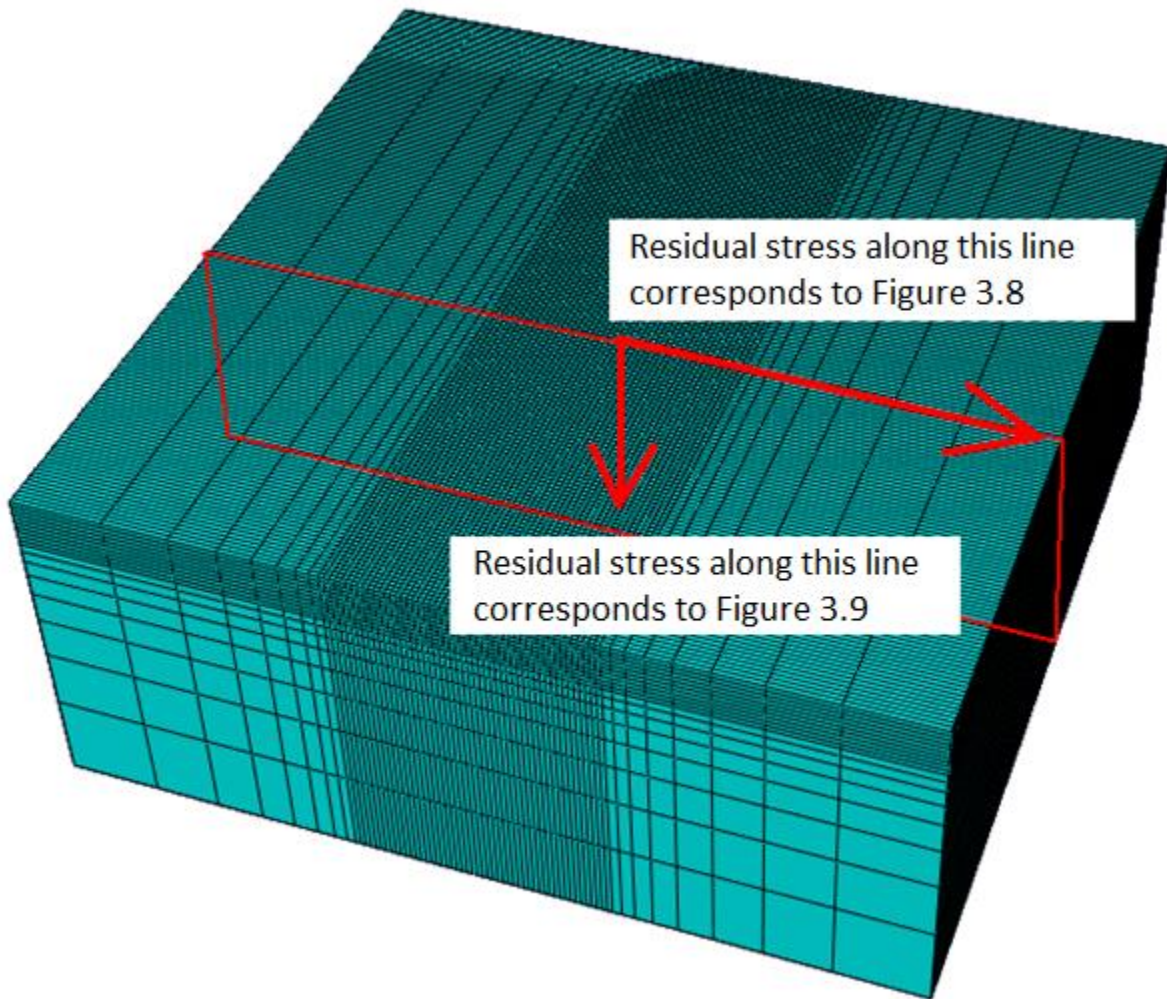
Figure 3.7: Residual stress value reporting scheme in the finite element model.
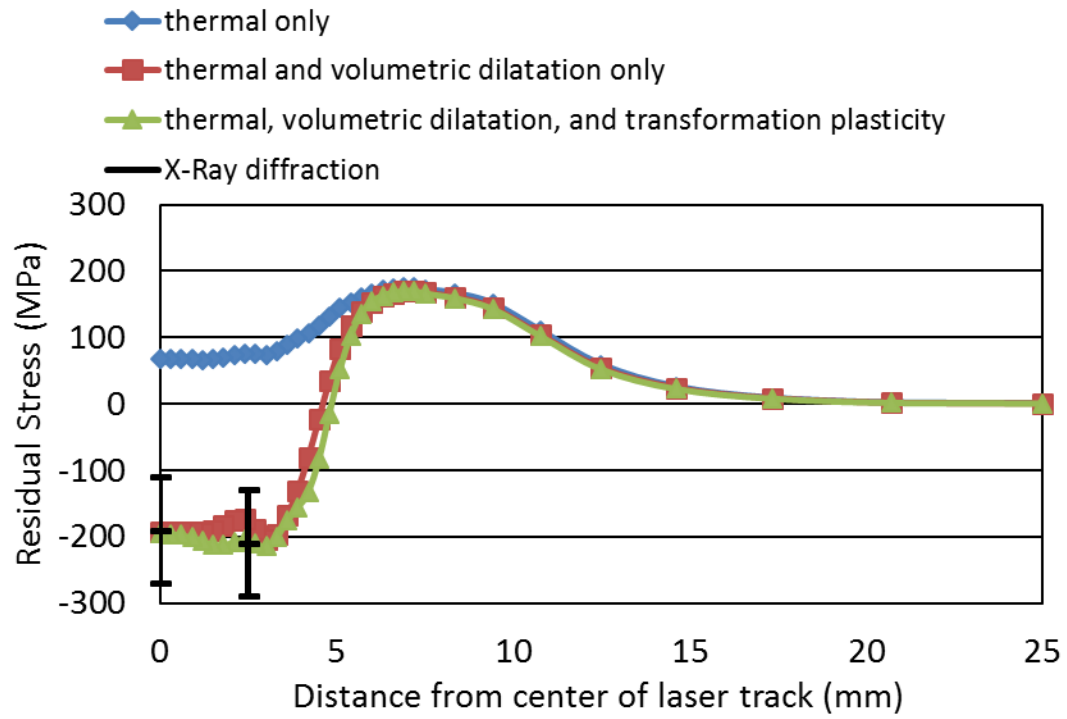
Figure 3.8: Residual stresses perpendicular to the laser travel along the surface of the workpiece.
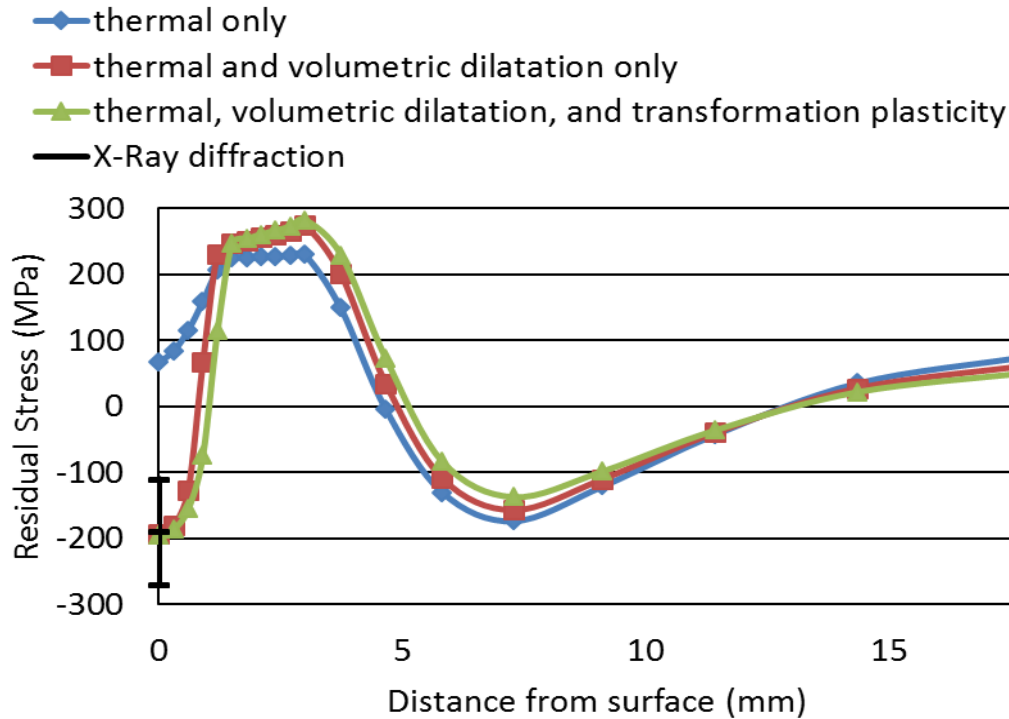
Figure 3.9: Residual stresses perpendicular to the laser travel into the depth of the workpiece.

From Figure 3.8 and Figure 3.9, it can be seen that phase transformation has a significant effect on the final stress state. Thermal residual stresses are essentially tensile, while stresses due to martensite and bainite transformations are compressive. During heating of the workpiece, austenite transformation is accompanied by a slight volume contraction, while during cooling, martensite or bainite is accompanied by a large volume expansion. Thus, depending on whether thermal strains or phase transformation strains are dominant, the residual stress field in a laser-hardened track can be either predominantly tensile or compressive. As shown in Figure 3.8, austenite-to-martensite transformation leads to a high compressive stress region of about 300 MPa in the transverse direction (perpendicular to laser travel), near the center of the laser track. Volumetric dilatation is the major contributor in phase transformation stresses. Stresses across

the surface, as well as stresses into the workpiece depth, show a strong compressive stress zone, then a small tensile stress region, followed by a weak compressive stress region. Compressive stresses are favorable towards higher fatigue strength and resistance to corrosion and wear (Pantelis et al., 2002). Future work in this area could include residual stress analysis in multi-track laser hardening with track overlap and residual stress analysis in a workpiece with complex geometry.

3.2 Laser Deposition

In high temperature applications, H13 tool steel has excellent material properties, as described by Roberts et al. (1998), such as high toughness, high stability in heat treatment, and high resistance to thermal fatigue cracking. Because of these properties, H13 is the standard material used in industry for toolings in hot work applications such as die casting, forging, and extrusion, and is the material used in the work presented in this section.

3.2.1 Experimental Setup and Operating Parameters

The laser deposition system used in this work is an Optomec LENS 750. The attached fiber laser has a maximum power of 500 W and a beam diameter of 0.74 mm. Particle size of the H13 tool steel powder ranges between 50 µm and 150 µm. A powder feeder delivers a stream of carrier gas and powder through four nozzles that converge at the laser's focal point. The laser and powder nozzles move vertically on a Z axis and are focused on an XY table. The system is enclosed in an environmental chamber charged with argon gas with an oxygen level below 20 ppm. As an example, a tensile test sample is shown during deposition in Figure 3.10.
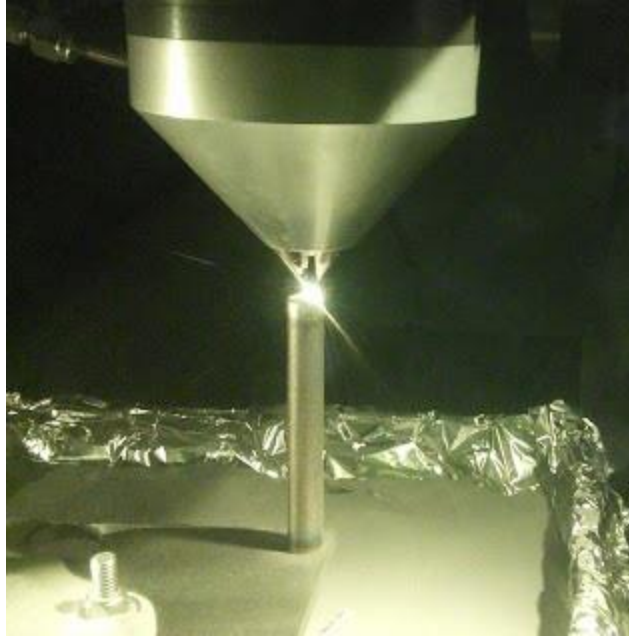
Figure 3.10: Laser deposition of a tensile test piece.

Laser power and powder flow rate can be seen as symbiotic parameters. It is the combination of the two that determines deposition quality. For example, for a given laser power there is an ideal powder flow rate that will result in a quality deposition track. If the powder flow rate is too high, inadequate melting of the powder will occur and porosity may form, or the resultant geometry will be uneven. If the powder flow rate is too low, the lower layer may melt too much and the deposition will be inadequate and inefficient. Thus, once an ideal powder flow rate is determined for a given laser power, a higher laser power ought to be matched with an increase in powder flow rate.

Laser power and laser travel speed together determine the overall amount of energy applied to the system. With a given laser power (and powder flow rate), a decrease in laser travel speed will

result in a greater deposition height, and an increase in speed will result in a lower deposition height.

3.2.1.1 Single-Layer Experiments

The first set of experiments was performed in order to determine the ideal powder flow rate for a given laser power. For this set of experiments, the laser power was set to 350 W, the laser travel speed was set to 14.8 mm/s, and powder flow rate was varied according to the parameters listed in Table 3.3. The goal was to find the powder flow rate that would return a deposition layer with no porosity, a very smooth top surface, and a maximum deposition height, with the former two criteria being the most important. The measured results for this set of experiments are shown in Table 3.3 and images of the cross-sections are shown in Figure 3.11.

Table 3.3: Results for single-layer experiments.

Experiment #	Powder flow rate (g/min)	Porosity	Smoothness	Deposition height (mm)
1	8.5	none	smooth	0.200
2	9.8	porosity	smooth	0.282
3	10.5	porosity	smooth	0.381
4	11.2	porosity	rough	0.414
5	12.5	porosity	rough	0.561
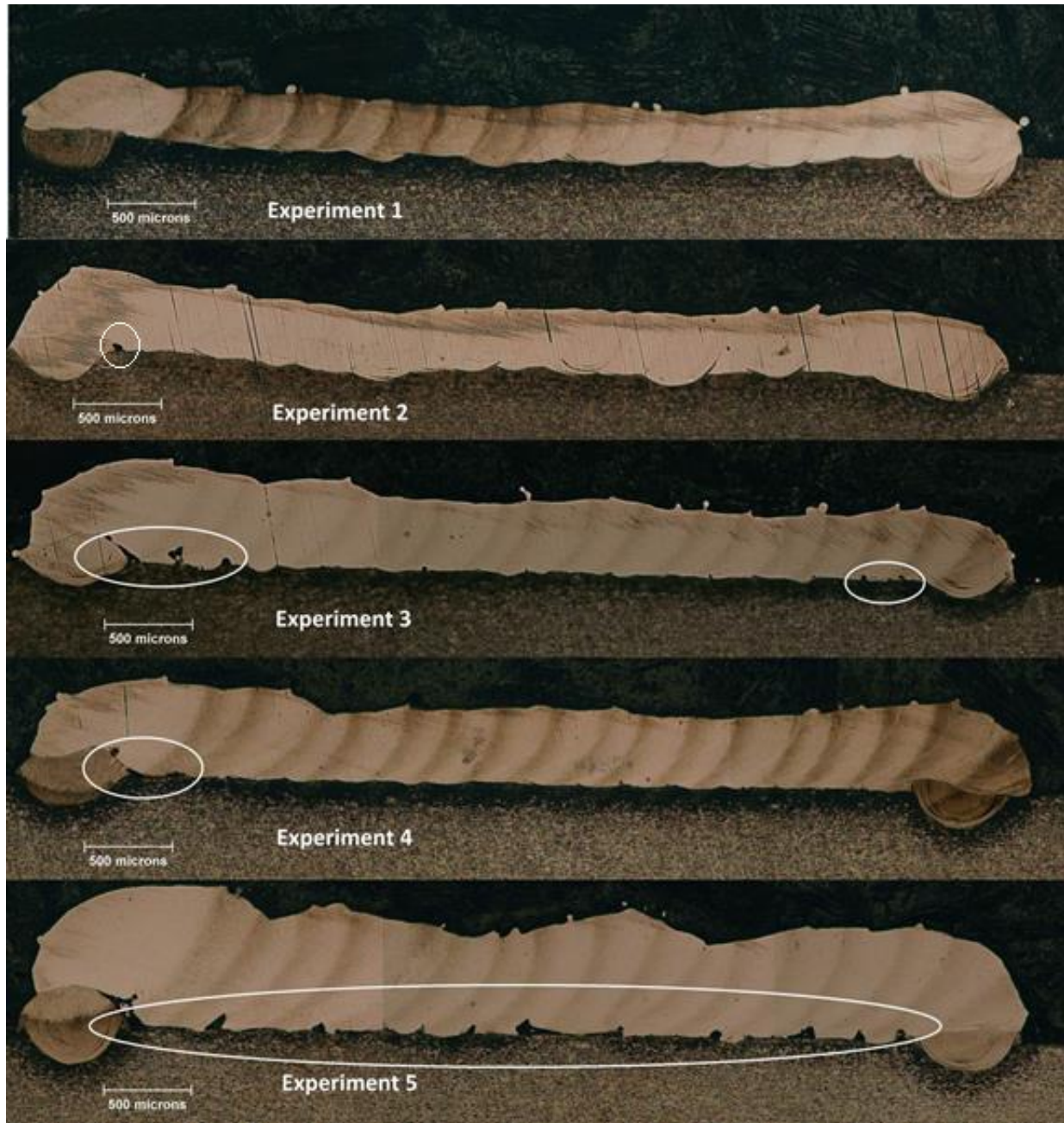
Figure 3.11: Cross-sectional view of the single-layer deposition tracks from Experiments 1-5. White ovals indicate porosity.

Porosity was determined by sectioning and observance under a microscope, while smoothness

was determined visually. Deposition height was measured under a microscope; since the top

surface is the result of the laser direct deposition process, there will always be high and low areas across the profile, as can be seen in Figure 3.11. The deposition height measurement was made at the lowest point of the profile, since this governs the number of passes which would be necessary to reach a target height.

Experiments 3, 4 and 5 resulted in porosity at the interface between the substrate and the deposition layer (as indicated in Figure 3.11), indicating that the powder flow rates for these three experiments are too high for a laser power of 350 W. Experiments 1 and 2 resulted in sides that were noticeably higher than the center area of the deposition. This is due to an improper track spacing that causes the final track to overlap the perimeter track. However, the lack of porosity in Experiment 1indicates that the powder flow rate is acceptable for this laser power. Experiments 4 and 5 resulted in rough tops, also from the too-high powder flow rate.

From these experiments, it was found that for this material and geometry and with a laser power of 350 W and laser travel speed of 14.8 mm/s, the powder flow rate must be no higher than 9.8 g/min; otherwise, porosity will form between the laser tracks at the interface between the deposition layer and the substrate, as shown in Figure 3.11.

3.2.1.2   Multilayer Experiments

Another set of experiments was performed to find an ideal powder flow rate and track spacing that would result in a smooth, low-porosity two-layer (or more) deposition with a maximum height. The measured results of these six experiments are listed in Table 3.4 and the cross-sectional images of each track are shown in Figure 3.12.

For Experiments 1-3, the track spacing was set at 0.300 mm and the powder flow rate varied from 8.5 g/min to 9.8 g/min. The same powder flow rates were used in Experiments 4-6, but with

a narrower track spacing of 0.282 mm. It can be seen from Table 3.4 that the deposition height

increases with powder flow rate, while an increase in track spacing results in a smaller deposition

height. Furthermore, similar trends with regard to the porosity and smoothness are observed for

increasing the powder flow rate.

Table 3.4: Results for two-layer experiments.

| Experiment #	Powder flow rate (g/min)	Track spacing (mm)	Porosity	Smoothness	Deposition height (mm)
1	8.5	0.300	none	smooth	0.526
2	9.1	0.300	porosity	smooth	0.711
3	9.8	0.300	porosity	rough	0.826
4	8.5	0.282	none	smooth	0.663
5	9.1	0.282	porosity	smooth	0.813
6	9.8	0.282	porosity	rough	0.917
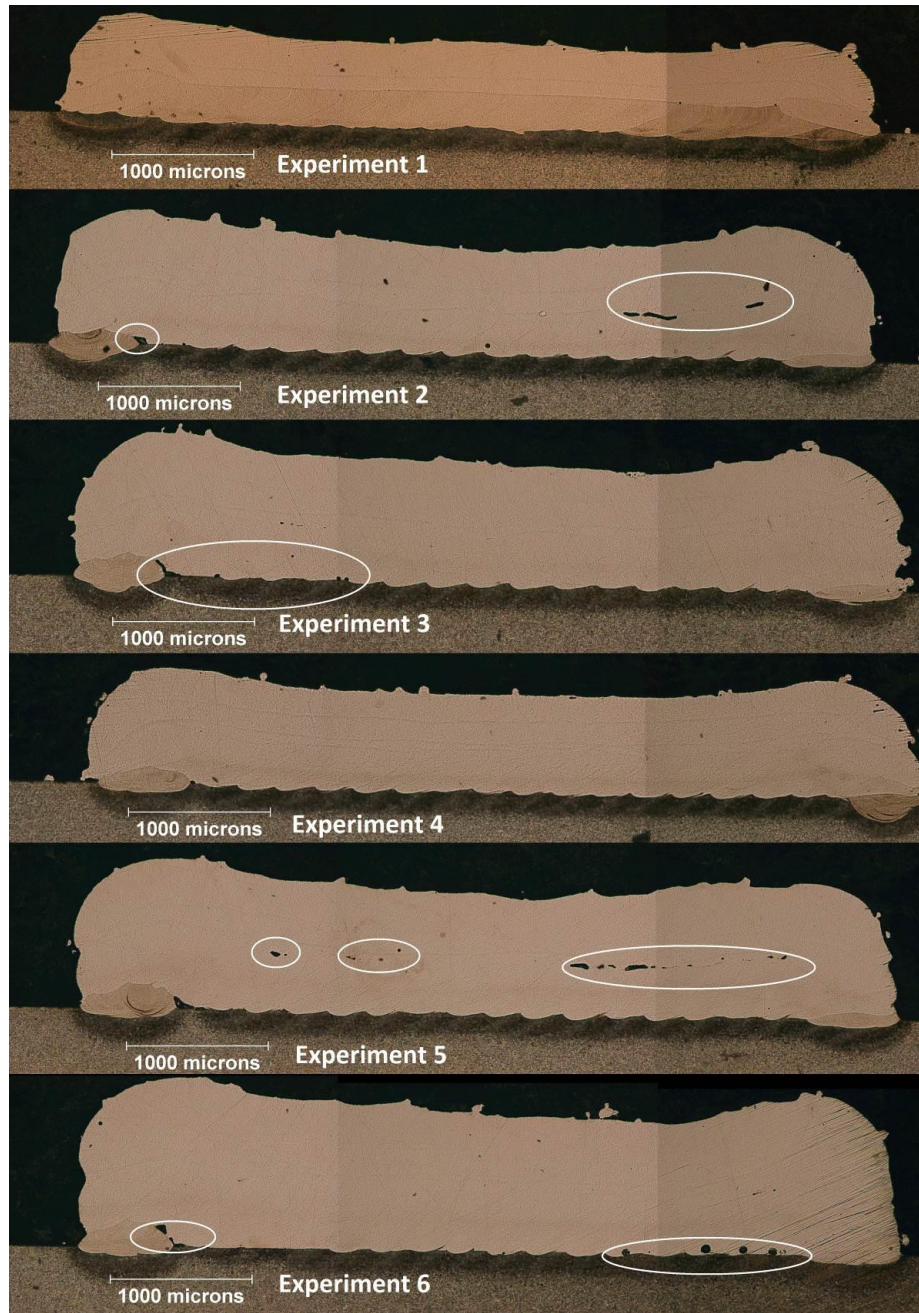
Figure 3.12: Cross-sectional view of two-layer deposition tracks from Experiments 1-6. White ovals indicate porosity.

From Figure 3.12, it can be seen that Experiments 2, 3, 5, and 6 all resulted in significant

porosity, either at the interface between deposition and substrate (Experiments 2, 3 and 6) or at

the interface between the two layers (Experiments 2 and 5). Experiments 1 and 4, both of which

have a powder flow rate of 8.5 g/min, do not have significant porosity. Although Experiments 1

and 4 both resulted in acceptable, porosity-free depositions, the wider track spacing of

Experiment 1 gives the advantage of being able to cover a wider area for the given laser travel

speed. Therefore, given this deposition system, the operating parameters for Experiment 1,

shown in Table 3.5, were chosen as the optimal operating parameters for laser deposition of H13

tool steel.

Table 3.5: Optimal operating parameters for multi-layer laser deposition of H13 tool steel.

Laser Power	350	W
Laser travel speed	35	in/min
Powder flow rate	8.5	g/min
Track spacing	0.300	mm

3.2.1.3   Case study for remanufacturing

Two industrial parts were used to prove the concept of using LDD for remanufacturing and

repair processes. The first part is a die casting mold insert, which was redesigned to have the

height of each spline increased by a certain amount. Rather than build a new insert, the old insert

was remanufactured using the LDD process to increase the height of each spline. A post-

deposition picture of the remanufactured die insert is shown in the top image of Figure 3.13. The

excess deposition material was then removed via traditional machining methods, as shown in the

bottom image of Figure 3.13. This insert was then put back into industrial production.

Figure 3.13: Industrial die insert after undergoing LDD to meet the requirements of a redesign before machining (top) and after machining (bottom).

The second part is a small, fragile die insert with a loop that often breaks when the casting is ejected. Rather than replacing inserts like this one after each failure, the LDD process was used to rebuild this tooling's broken geometry as a proof of concept. Pictures of a similar unbroken insert, a broken insert, and a repaired insert (after LDD, but before machining and finishing) are shown in Figure 3.14.

Figure 3.14: From left to right: unbroken insert with similar loop geometry, broken insert, and repaired insert. The repaired image was taken after LDD, but before machining and finishing.

3.2.2 Properties of Laser-Deposited H13 Tool Steel

Due to the very fast cooling rates associated with laser deposition processes, the microstructure of laser-deposited H13 is usually much finer than that of stock material. The fast cooling rate also results in a microstructure that is mostly martensite, and is, therefore, very hard. The extreme temperature gradients due to the high energy density of the laser beam cause strong thermal strains, while the solid-state phase transformations of steel cause strong phase transformation-induced strains, both of these resulting in strong residual stresses. Due to these phenomena, the strength of laser-deposited H13 can be substantially higher than that of stock H13 material.

3.2.2.1 Microstructure

A micrograph of a multi-layer sample of laser-deposited H13 is shown in Figure 3.15, where three layers with different orientations for laser travel direction can be seen. In the 1st layer, the laser travel direction for the individual laser tracks was oriented normal to the page. Laser track

overlap is clearly visible. In the 3rd layer, the laser travel direction is across the page, or 90° with respect to the 1st layer. The laser travel direction of the 2nd layer is 45° in between the 1st and 3rd layers.
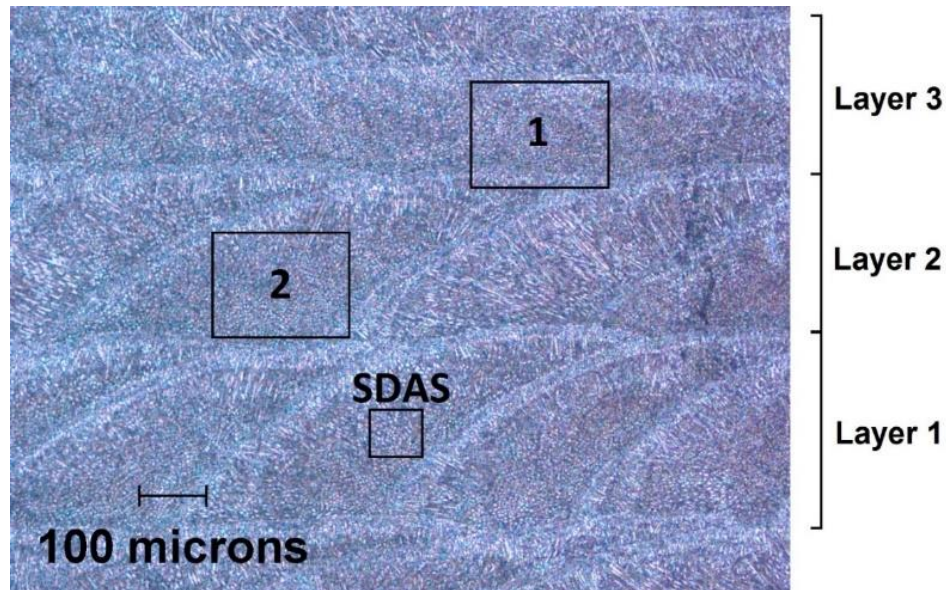
Figure 3.15: Multi-layer sample of laser-deposited H13 showing locations of grain size (1 and 2) and secondary dendrite arm spacing (SDAS) measurements.

Grain size was measured at two separate locations 1 and 2, shown in Figure 3.15 and the magnified images of locations 1 and 2 shown in Figure 3.16. According to these measurements, the average grain size for laser-deposited H13 under the parameters presented in this paper is 28 μm. The secondary dendrite arm spacing (SDAS) was also measured, as shown in Figure 3.17. The distance across a number of secondary dendrite arms was divided by the number of secondary dendrite arms, resulting in an average SDAS of 1.86 μm.
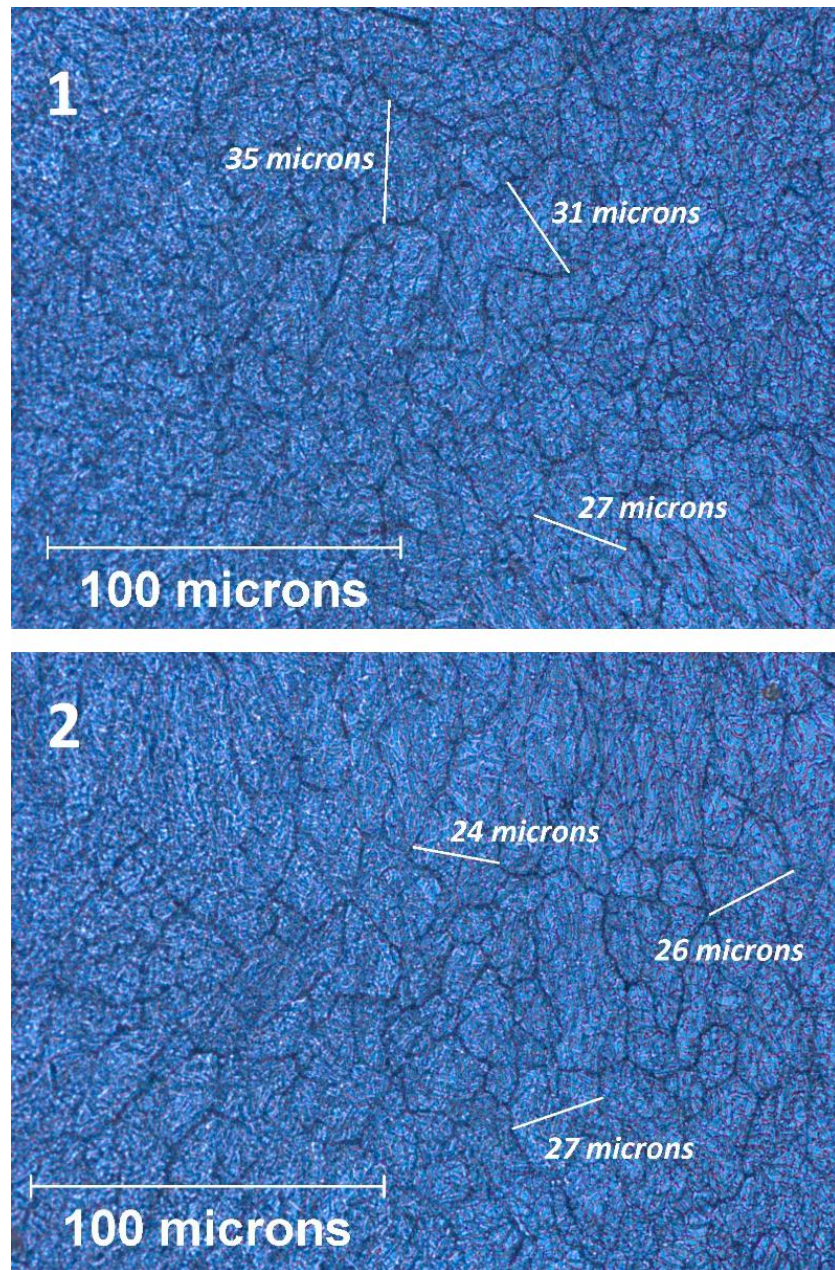
Figure 3.16: Grain size measurements from locations 1 and 2 as shown in Figure 3.15.
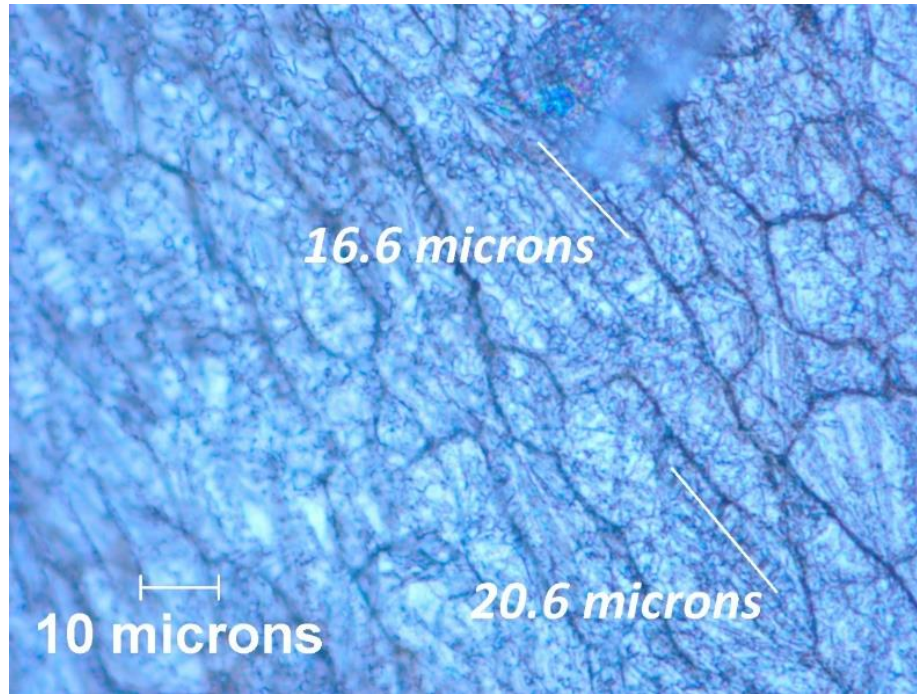
Figure 3.17: Secondary dendrite arm spacing (SDAS) measurements as shown in Figure 3.15.

3.2.2.2   Material Strength

In order to test the strength of laser-deposited H13 tool steel, three test specimens were built via LDD with the same operating parameters as those listed in Table 3.5. Each sample, shown in Figure 3.18, was a cylinder with a diameter of 12.7 mm and a height of at least 90 mm, and was machined on a lathe to meet the ASTM E8 tensile testing standard (ASTM, 2001). The reduced section for each sample is 6.35 mm diameter and 31.75 mm long. The samples were tested in an MTS 793 tensile testing machine at a rate of 5.0 mm/min. The stress/strain curve of each sample is shown in Figure 3.19. The hardness near the center of one of these samples was 690 Vickers (58 HRC), measured by a Vickers indenter with a 1kgf load and a dwell time of 20 s.

Figure 3.18: Laser deposited H13 steel tensile testing samples.
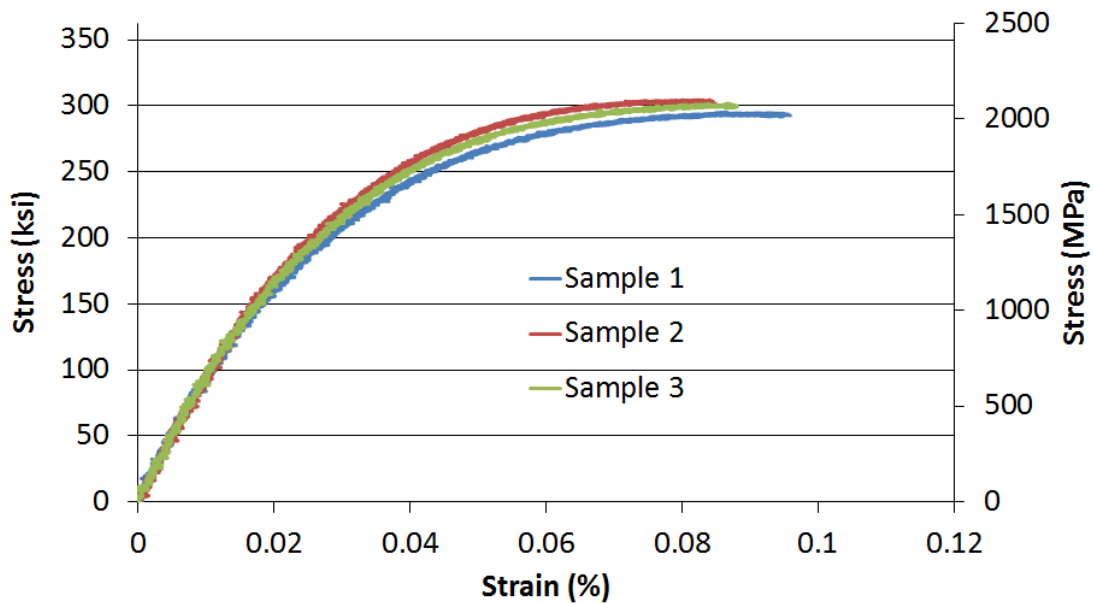
Figure 3.19: Stress/strain data from tensile testing of laser deposited H13 steel.

According to the test data, the ultimate tensile strength (UTS) of the three test samples were

2035 MPa, 2100 MPa, and 2081 MPa, with an average UTS of 2072 MPa. These values match

well with the measured hardness value of 690 Vickers (58 HRC), which correspond to a UTS of 2030 MPa according to a conversion chart ("Maryland Metrics," 2016). Published UTS values for commercial H13 hot-work die steel vary between 1600—1800 MPa. Laser-deposited H13 tool steel, therefore, shows a UTS value between 15% and 30% stronger than commercial H13 tool steel.

3.2.3 Simulation and Comparison

3.2.3.1 Thermal Model Results

Simulation of the deposition process was performed using a three dimensional numerical model developed by Wen and Shin (2011, 2010). The computational domain consisted of a 12mm × 5mm × 12mm substrate composed of H13 tool steel to which H13 powder was being deposited via the LDD process with a total of 343,728 elements arranged in a structured, non-uniform mesh. Thermal and physical properties of the H13 tool steel are provided in Table 3.6. The substrate was assumed to be initially at 300K, and convective boundary conditions were set at all faces of the steel substrate using a constant heat transfer coefficient of 10 W/m2-K with an ambient temperature of 300K.

Table 3.6: Material properties of H13 tool steel and laser parameters for the deposition simulation.

Property	Units	Solid phase	Liquid
Density	kg/m^3	7835*	7835*
Specific heat	J/kg-K	658†	804†
Thermal conductivity	W/m-K	28.6*	28.6*
Liquid viscosity	kg/m-s	0.005†	
Thermal expansion coefficient	1/K	1.45e-5†	
Absorptivity	-	0.15	
Emissivity	-	0.7	
Latent heat	kJ/mol	2.72e5†	
Solidus temperature	K	1588*	
Liquidus temperature	K	1727*	
Surface tension coefficient	N/m-K	4.3e-4‡	

* (Lin et al., 2007)
† (He et al., 2009)
‡ (He et al., 2003)

A series of experiments was performed using an Optomec LENS 750 LDD system in order to validate the simulation by comparing measured and predicted track geometry, heat-affected zone (HAZ), and molten pool depth and width for both single and multiple track depositions. The deposition parameters used in these simulations correspond to those used for experimentation and measurement as listed in Table 3.5 in Section 3.2.1.2.

The simulations were validated against the experimental data, first for a single-track case, then for a multi-track case. Figure 3.20 provides an isometric view of the deposition of the 1st track showing the temperature isocontours upon completion of the single-track simulation. In Figure 3.21, overlays of the predicted track profile, molten pool, and HAZ geometries are shown on an image of a cross section from a single-track experiment, comparing the predicted and measured geometries. Based on the shape and location of each of the contours shown in Figure 3.20 and

Figure 3.21, it can be seen that the deposition process was reasonably well captured in the Laser

Deposition model for a single track simulation.
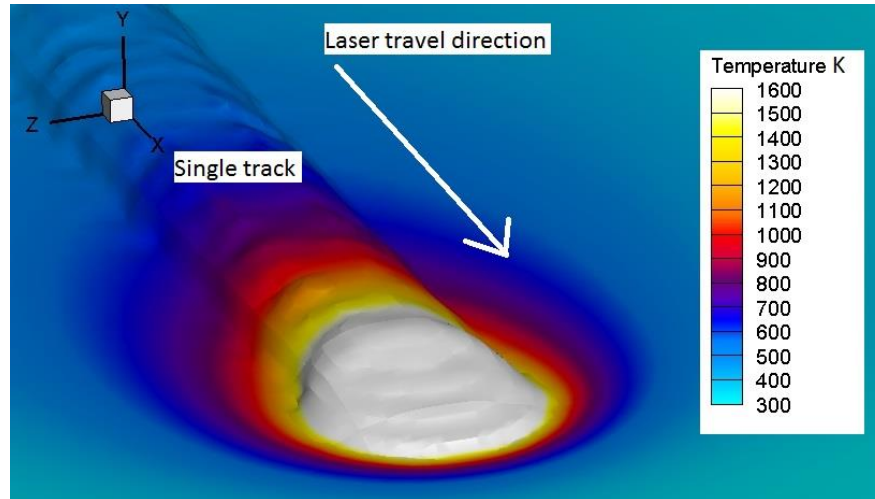
Figure 3.20: Isocontours at the conclusion of simulation for the 1st track deposited on H13 substrate.
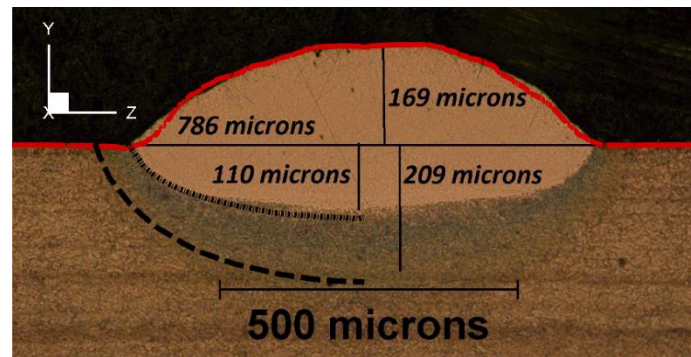
Figure 3.21: Molten pool (dotted black), heat-affected zone (dashed black), and deposited track geometry (solid red line) for single track deposition simulation compared with experiment.

Simulation of the LDD process involves a high computational cost. Since the goal of this

simulation was to acquire the geometry and temperature profile of bulk deposition, the model

must calculate the multi-track case. From experimentation it was determined that the cross-

sectional profiles of the first two tracks in a multi-track deposition sample were unique, but the third and all subsequent track cross-sectional profiles were similar. Therefore, three subsequently deposited tracks provided an average steady-steady profile which essentially remained unchanged upon sufficient additional deposited tracks. Thus, to minimize the amount of simulation time, a solidified multi-track cross-sectional profile was captured based on a two-track experimental sample, as shown in Figure 3.22, and was used as the initial surface condition for the simulation of the third track deposition process. The profile of the two-track surface was created via manual selection of the interface points at 10 µm intervals along the cross section of the two-track sample, and was compared to additional two-track experiments to ensure a reasonable and non-extreme track profile was being selected as the basis for multi-track work.
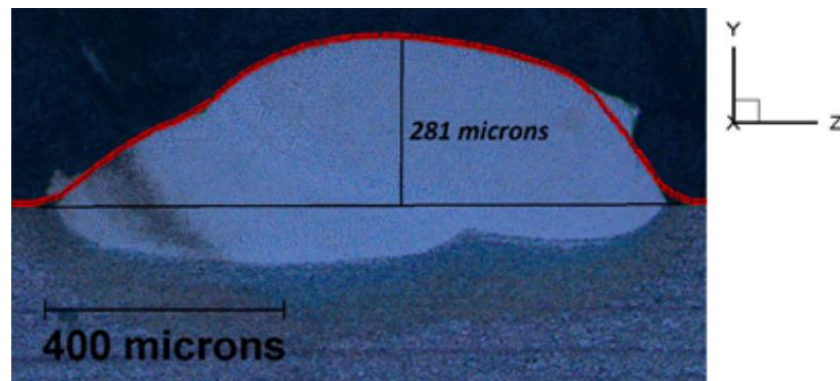
Figure 3.22: Two-track cross-sectional profile showing the extracted track geometry for the initial seeding of the three-track simulation.

Simulation of the multi-track case was allowed to run until a pseudo-steady profile developed with respect to the direction of travel. This required approximately 4.5 mm of travel in the positive x-direction. Figure 3.23 shows an isometric view of the simulated three-track deposition process with temperature isocontours at the end of simulation. In Figure 3.24, overlays of the

predicted track profile and molten pool are shown on an image of a cross section from a multi-track experiment, comparing predicted and measured geometries with a reasonable agreement.
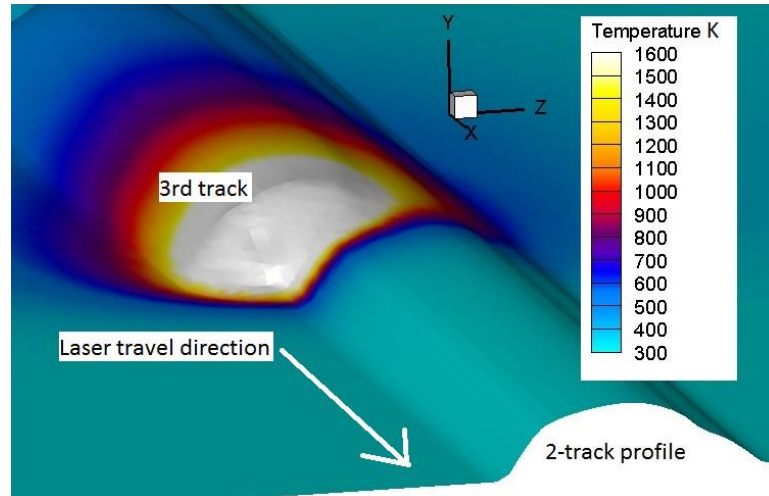
Figure 3.23: Results of the three-track simulation – pseudo-steady-state surface during deposition.
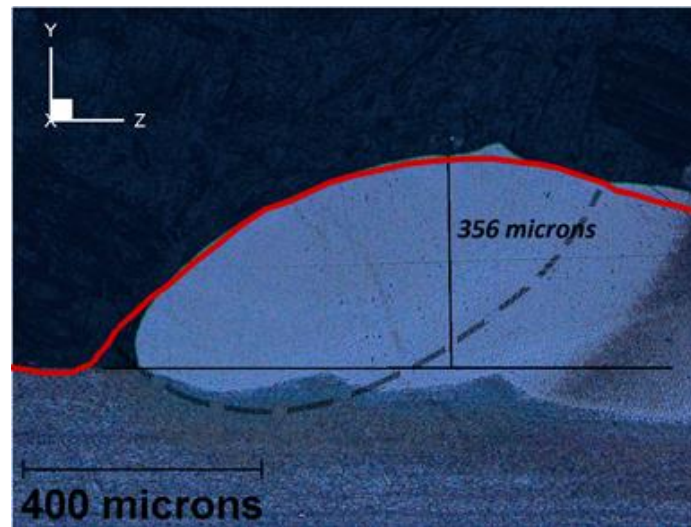
Figure 3.24: Molten pool (dashed black line) and deposited track geometry (solid red line) for the three-track deposition simulation compared with experiment.

3.2.3.2 Microstructure

After completing the three track profile, the temperature and geometry data were used in conjunction with the CA-PF model discussed in Section 2.3.2. The temperature and geometry data are read into the CA-PF model at the beginning of the CA-PF analysis. The 2D CA-PF analysis domain is 430 µm high and 300 µm wide and the initial location of the analysis plane is at the heart of the molten pool (the bright region in Figure 3.25) where the analysis plane has the maximum amount of liquid before solidification begins. Aside from being a mirror image, the data in Figure 3.25 is identical to the data shown in Figure 3.23.
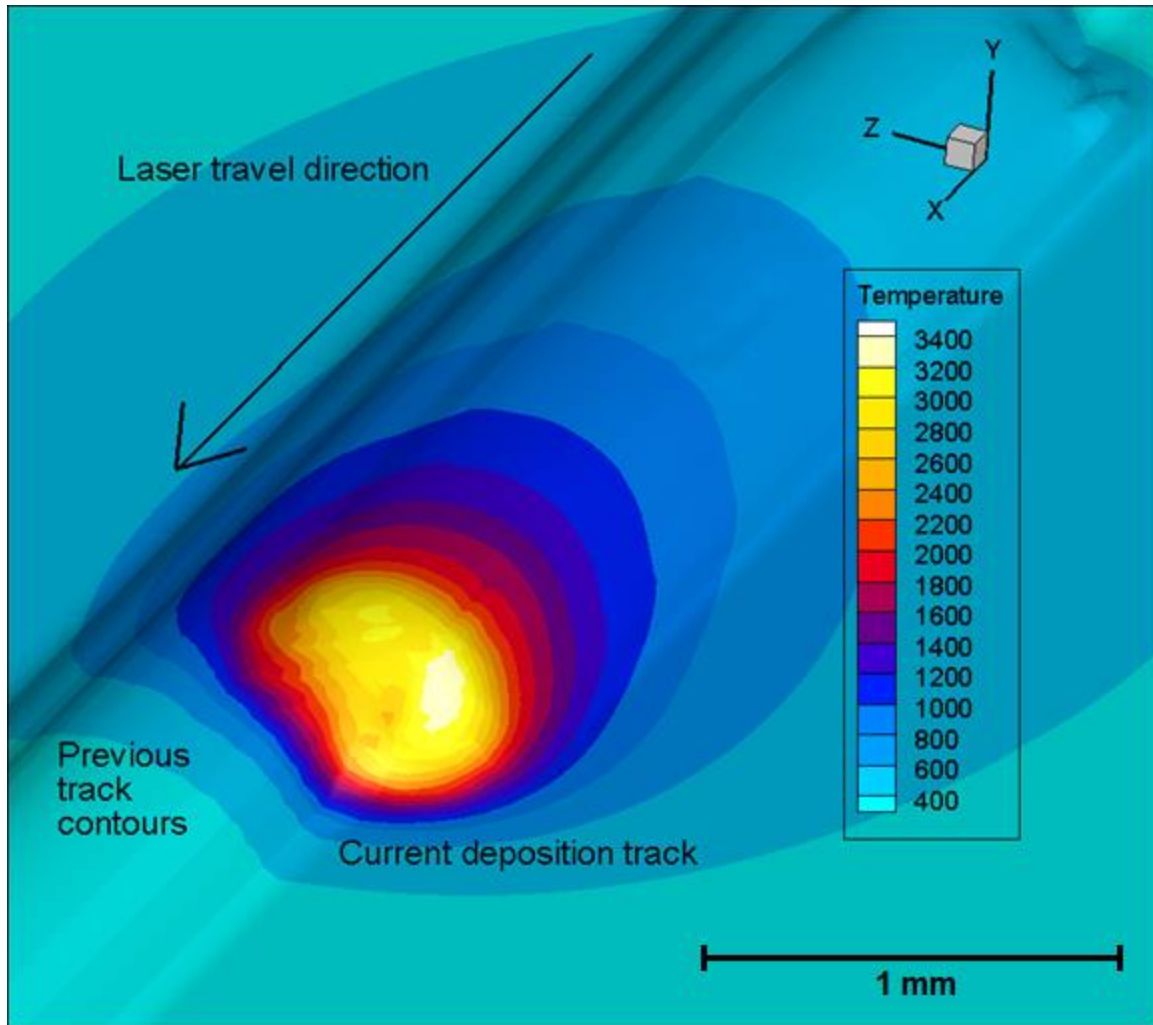
Figure 3.25: Multi-track direct deposition simulation results from which the temperature data for the CA-PF simulation is taken. The data here is a mirror image of the data shown in Figure 3.23.

As time progresses, the 3D temperature field is brought forward (relative to the 2D CA-PF analysis plane) in the laser travel direction and at the laser travel speed. At each time step of the CA-PF simulation, the temperature for the CA-PF simulation is interpolated from the LDD model's 3D temperature field at the current relative position of the 2D CA-PF analysis plane. As the CA-PF 2D domain moves through the molten pool toward the solid region, solidification begins and dendrites will start to grow within the CA-PF analysis plane, according to the thermodynamic conditions of the domain. A track's simulation is complete when all of the 2D

CA-PF domain is solidified. To simulate multi-track and multi-layer dendrite growth, the CA-PF region is shifted laterally by the track spacing (0.300 mm in this paper) for each track and each layer and then the next track begins again with the 2D CA-PF analysis plane in the heart of the molten pool. Areas of the second track that were previously solid and now have a temperature higher than the melt temperature are reset as liquid and are subsequently re-solidified during the second track's simulation.

In this paper, four tracks were simulated: two on the first layer and two on the second layer. The locations of each of these simulations are depicted in Figure 3.26. The microstructure is first predicted by the CA-PF model in the red box labeled "CA-PF initial simulation domain location." After the dendrite growth simulation of the first track is complete, this predicted microstructure is then used as the initial microstructure for the second simulation at the location indicated in Figure 3.26. The small black boxes indicate the locations of the lower left-hand corners of each simulation location. Simulations 3 and 4 then use the previous simulations' predicted microstructure as their initial microstructures, resulting in the final microstructure predicted in the green region labeled "CA-PF final simulation domain location."
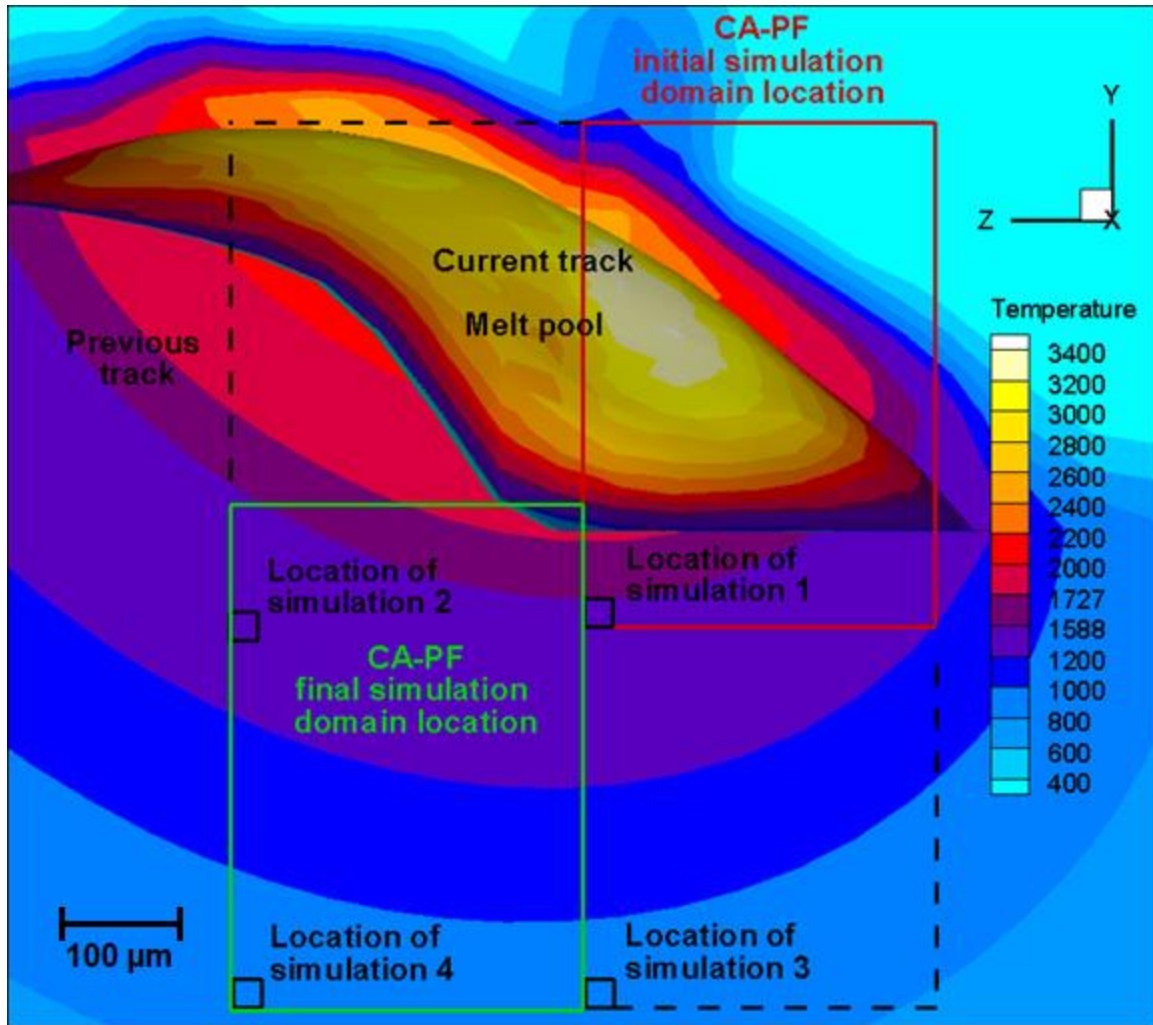
Figure 3.26: Head-on view of direct deposition track. Laser travel is in the X direction (out of the page).

The background temperature field shown in Figure 3.26 (a head-on view of the LDD simulation) represents the 2D temperature as interpolated from the 3D temperature data from the LDD model at a certain point in simulation time. The area in the top half of Figure 3.26 labeled "Current track Melt pool" represents the temperature and geometry of the molten pool. The order of the four simulations, as they appear in Figure 3.26, is not the order in which they each track is deposited. Obviously, a track in the position of simulation 4 as shown in Figure 3.26 would be the first of the four tracks to be deposited. This is the only track that is being considered in the

microstructure prediction simulations as noted by the text "CA-PF final simulation domain location" in Figure 3.26. The temperature field of each neighboring track will strongly affect the final microstructure predicted at this location. Therefore, the four locations noted in Figure 3.26 depict the positions of the temperature field relative to the final simulation domain location as deposition occurs for each neighboring track. Each of the four simulations required about 20 hours of computation on Intel Xeon CPU E5-2660 v3 with 20 cores at 2.6 GHz. This does not include the computational cost of the thermal model.

3.2.3.2.1 Single Track Results

Results for the first track, Simulation 1, are shown in Figure 3.27 through Figure 3.29. The coordinate system of the CA-PF model, as shown in Figure 3.27, is not the same as the coordinate system of the thermal model shown in Figure 3.25 and Figure 3.26. However, the x/y plane of the CA-PF model is always parallel to the y/z plane of the thermal model. The first track simulation begins at the heart of the molten pool with the temperature profile shown in Figure 3.27. The values of some of the isotherms have been adjusted to show the boundary of the molten pool and the location of the mushy zone.
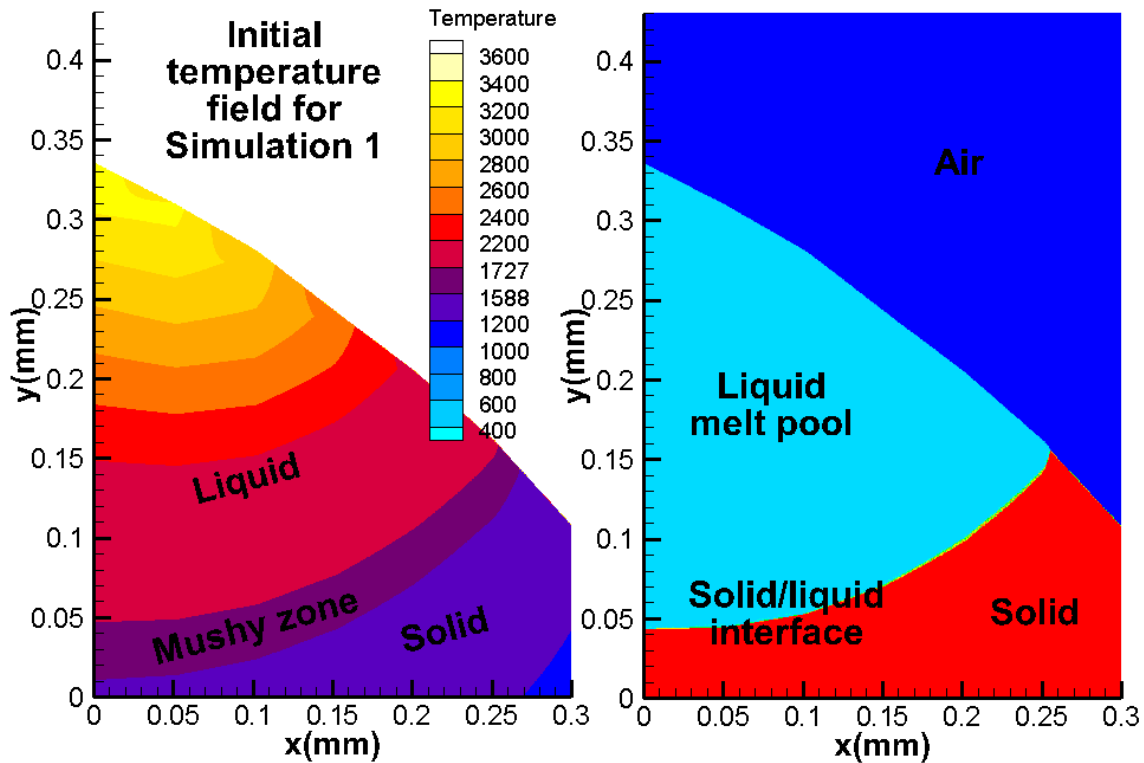
Figure 3.27: Initial temperature field and phases before dendrite growth begins for the first track (Simulation 1).

As the temperature begins to drop, randomly oriented seeds are randomly placed at the back of the molten pool and grains will begin to grow in the direction of the temperature gradient, as shown in Figure 3.28. The first solidified phase here is austenite with a face-centered cubic structure. The dendrites with crystallographic orientations which are closely aligned with the temperature gradient will grow more quickly, blocking the dendrites with less favorable orientations. The competitive growth is clearly seen in the zoomed-in image of Figure 3.28, as well as the detailed microstructure predicted by the CA-PF model. Once the temperature cools sufficiently, the melt in the entire 2D CA-PF domain will completely solidify, as shown in Figure 3.29.
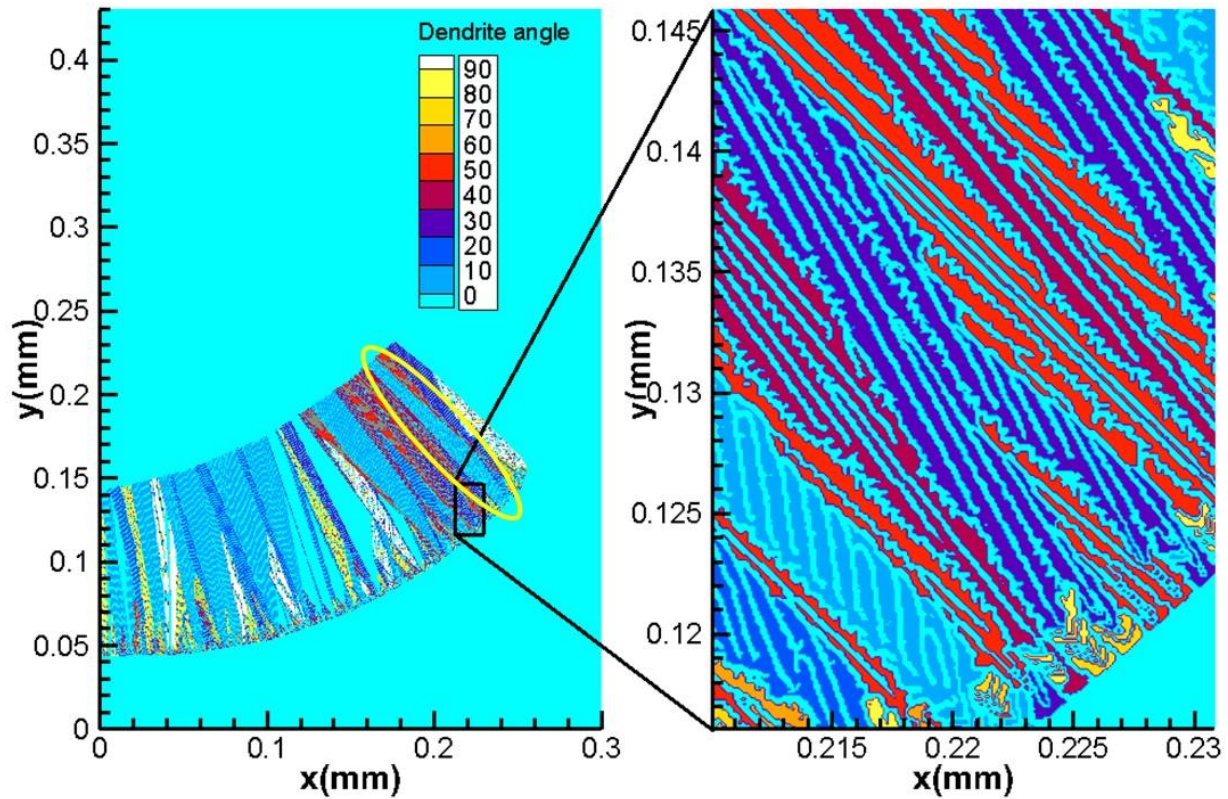
Figure 3.28: The microstructure during solidification of the first track (Simulation 1) (left). A zoomed-in view near the bottom of the molten pool showing individual dendrites, secondary dendrite growth, and competitive growth (right).

In any directional solidification process, grains with a favorable orientation will have an advantage over less favorable orientations, but this is only an advantage—not an absolute outcome. The competitive growth phenomenon will reliably produce large-scale trends, as seen in Figure 3.28. Near the left side of the left figure are shown a majority of orientations at or near $0°$ or $90°$ growing in the y direction, while grains on the right side of the left figure are growing diagonally and are primarily $30°$ to $60°$ orientations. The overall trend is obvious, but some grains may beat the odds and successfully grow in unfavorable directions. In Figure 3.28, a grain with an orientation close to $0°$, indicated by a yellow oval, grows in unfavorable conditions

where the temperature gradient is close to 45°. However, in Figure 3.29 it is shown that the same

grain is eventually blocked by grains with orientations close to 45°.
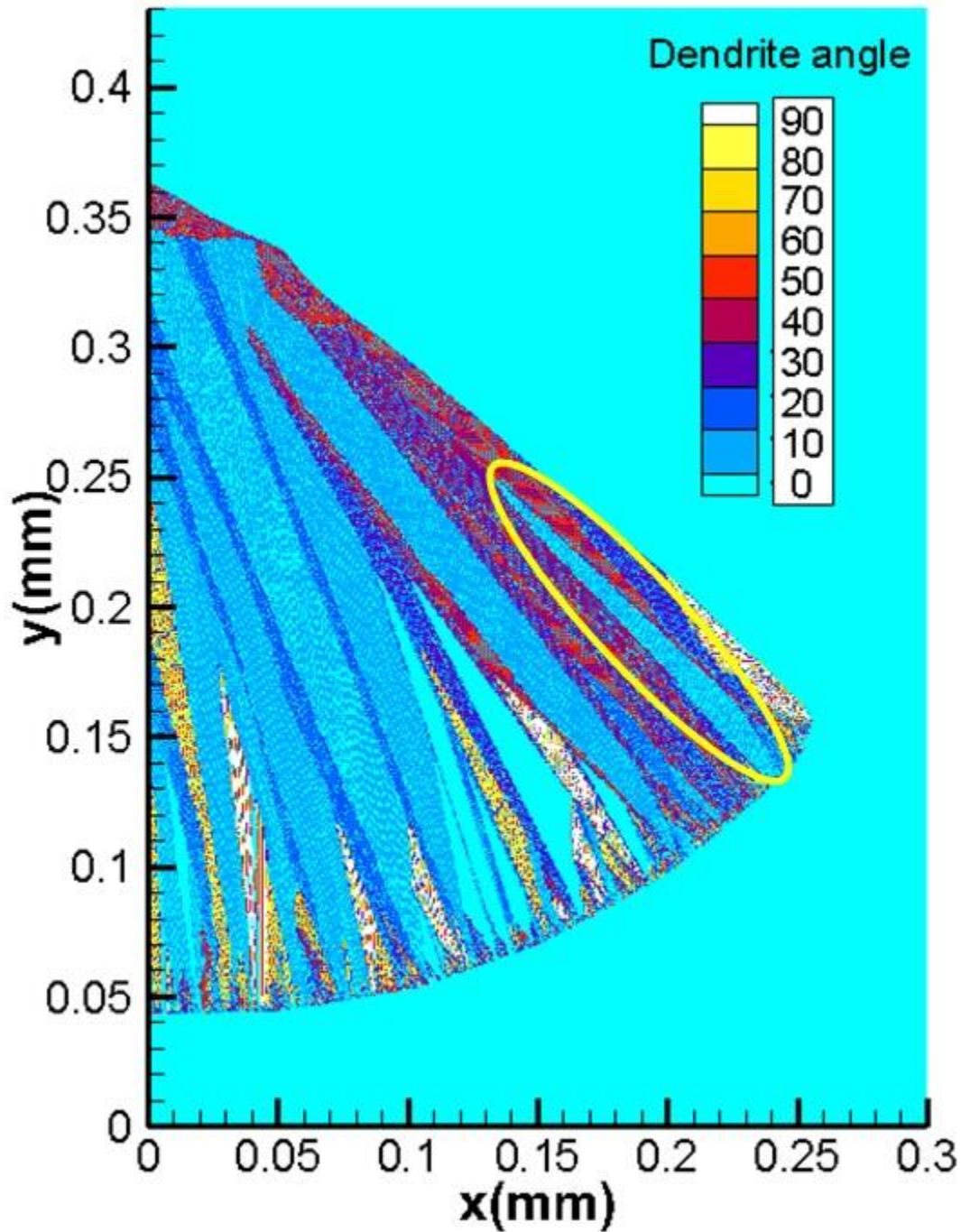
Figure 3.29: Solidification microstructure for the first track (Simulation 1) showing the angle of
each dendrite between 0° and 90°.

It is noted that all simulations from the CA-PF model are 2D. It is true that true grain growth is a 3D phenomenon and a 3D simulation will always be superior to a 2D simulation without regard to computational cost. It is well known that the computational cost of a 3D simulation is usually orders of magnitudes higher than a 2D simulation. Simulations performed in 2D of 3D processes have provided valid and useful data for decades and cannot be overlooked in their usefulness. However, one must be careful in choosing how to perform a 2D simulation of a 3D process (Bailey et al., 2020).

Generally, in solidification conditions during welding or additive manufacturing, dendrites will grow toward the heat source. If the solidification speed of the grains is similar or slower than the heat source's travel speed, the grains will appear equiaxed in a cross-section perpendicular to the heat source's travel direction when in fact the grains are columnar in their growth direction. This will result in a misleading and inaccurate microstructure. However, if the grains' solidification speed is much faster than the heat source's travel speed (as is the case in the conditions in this work), the grains will grow quickly toward the center of the weld pool, resulting in accurate columnar grains as viewed in a cross-section perpendicular to the heat source's travel direction. This phenomenon is clearly explained by Tan et al. (2011).

3.2.3.2.2 Multi-layer Multi-track Results

After the first track is finished, the resulting microstructure (top left image of Figure 3.30) is used as the initial microstructure of the second track, Simulation 2. When the temperature is above the melting temperature, the solidified material in the corresponding region will be assigned as liquid. Then as the temperature in Simulation 2 drops, dendrites again begin to form along the bottom of the molten pool. Once solidification of the second track is complete, the resulting microstructure (top right image of Figure 3.30) is used as the initial microstructure of

the third track (Simulation 3), and the third track's final microstructure (bottom left image of Figure 3.30) is used as the initial microstructure of the fourth track (Simulation 4). The final predicted microstructure of the multi-track, multi-layer laser direct deposition simulation is shown in the bottom right image of Figure 3.30.

The final predicted microstructure, after all four simulations, should match the microstructure of the multi-layer, multi-track experimental microstructure shown in Figure 3.31 through Figure 3.33. Figure 3.31 is a microscope image of a cross-section of a two-layer multi-track LDD sample work piece. The substrate and both layers are clearly shown. The box in Figure 3.31 represents the area of an SEM image shown in Figure 3.32.

Melt boundary lines were added to Figure 3.32 to indicate the melt boundaries of each laser track. The box "Detail A" represents the area of the zoomed-in SEM image at the bottom of Figure 3.33. Shown at 750x zoom, the SEM image in Figure 3.33 shows the dendritic details of the LDD microstructure as well as the melt boundaries between the tracks. The direction of dendrite growth is clear along the melt boundaries. This actual microstructure is compared with the top image in Figure 3.33, a zoomed-in image of the final predicted microstructure after all four CA-PF simulations (Detail B of Figure 3.30).

In comparing these two images, it is clear that the locations and curves of the molten pool boundaries agree, as do the average size and orientations of the dendrite arms near the molten pool boundaries. The arrows in the Figure 3.33 help illustrate the agreement of directional growth between the predicted and experimental dendrites. The measured primary dendrite arm spacing for both the predicted and experimental dendrites agree well at around 2 µm. The CA-PF

model accurately predicts the directional dendrite growth during LDD via multi-track and multi-layer solidification simulations.

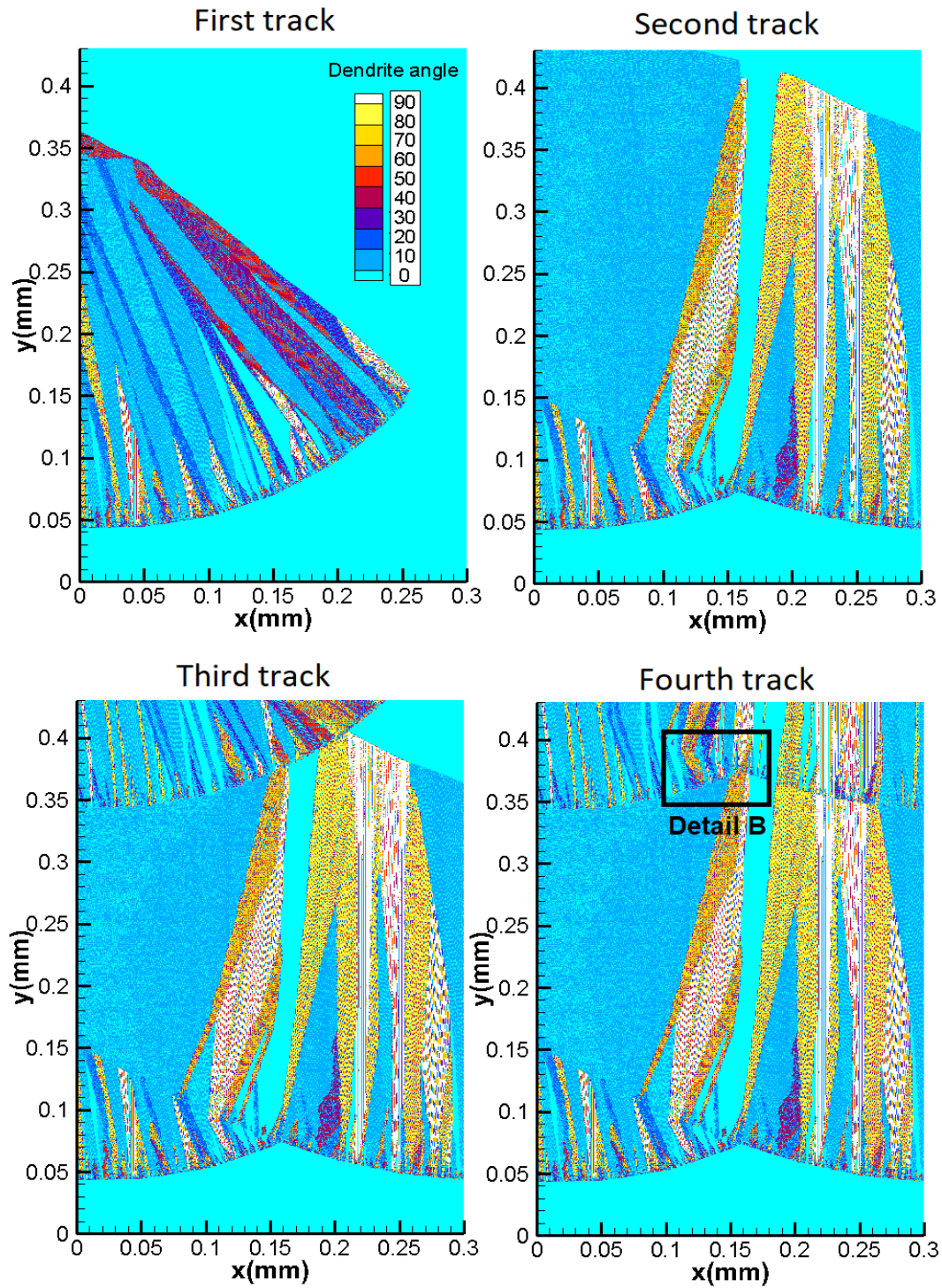Figure 3.30: Predicted solidification microstructures for Simulations 1 through 4 showing the angle of each dendrite between 0° and 90°.
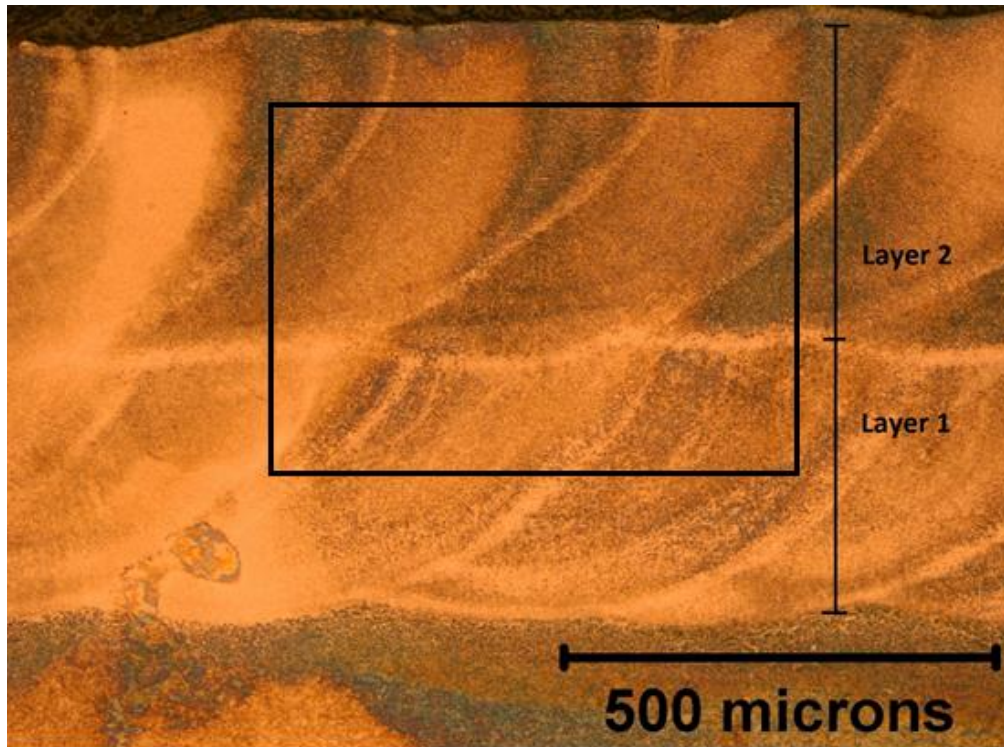
Figure 3.31: Microstructure from 2-layer experimental results. Region for Figure 3.32 shown in box.
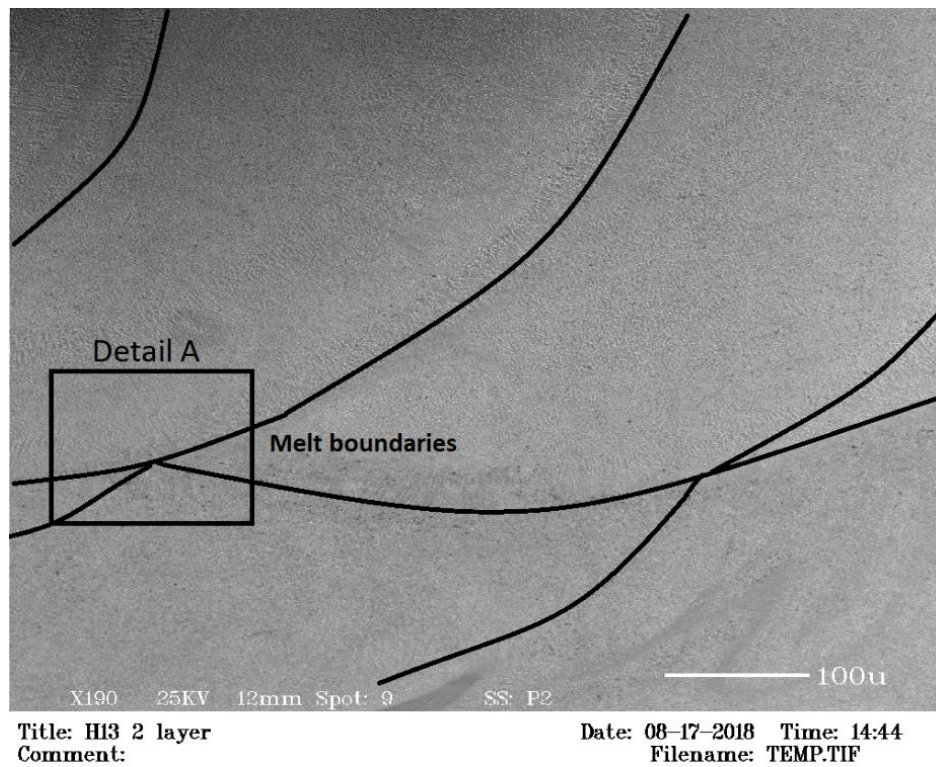
Figure 3.32: Melt boundaries are shown graphically. Detail region A is shown in Figure 3.33.
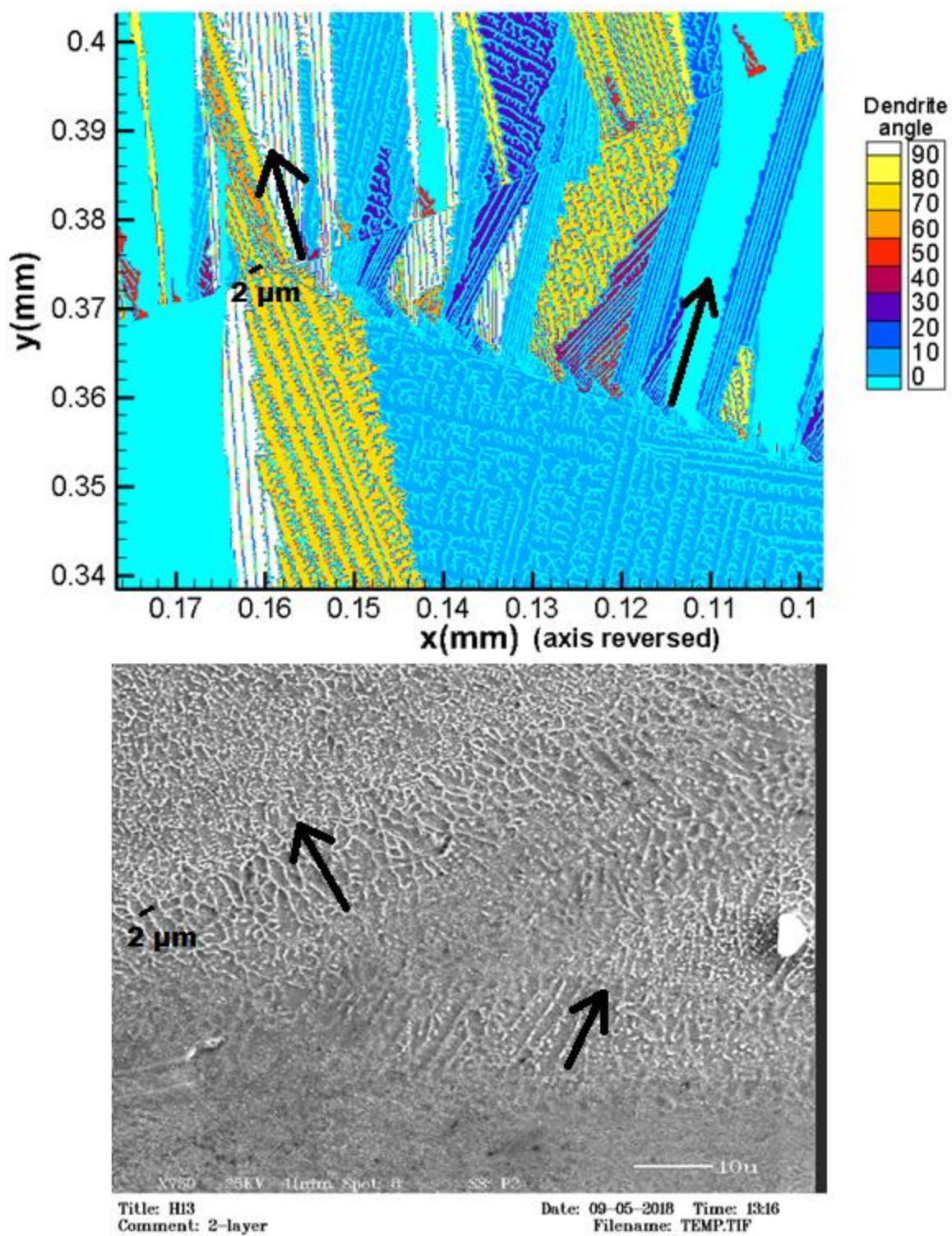
Figure 3.33: Detail A (bottom) from Figure 3.32 compared with Detail B (top) from Figure 3.30.

3.2.3.3 Phase Transformation and Hardness

As discussed in Section 2.2, phase transformation-induced strains may be a significant piece of the overall residual stress developed during manufacturing processes. Using the model discussed in Section 2.1, the phase transformation was predicted through two different implementations: the CA-PF model and an ABAQUS subroutine.

3.2.3.3.1 2D Phase Transformation Prediction via CA-PF

In addition to predicting dendrite growth during solidification, the CA-PF model has been expanded to include solid phase transformation prediction for hypoeutectoid steels. As noted above, austenite is the solidified phase, but H13 steel can undergo dramatic phase transformations during the repeated cooling and reheating cycles, which are typical in AM. Austenite is not stable at room temperature and the newly solidified material will quickly transform to other phases before the material reaches room temperature. Typical to LDD, quickly cooling austenite will transform to martensite, a body-centered tetragonal phase that has a very strong influence on the material hardness, strength, and distortion. Additionally, previously formed martensite is easily tempered by the heat of neighboring tracks in multi-track, multi-layer situations, resulting in additional phase transformation.

The post-cooling results of the solid phase transformation model for all four tracks are shown in Figure 3.34 in terms of the martensite phase fraction. For the first track, it is clear that the solidified and cooled material is nearly 100% martensite. This is expected since the entire molten pool solidifies as austenite and transforms to martensite due to the rapid cooling. The second track, as expected, also consists of nearly 100% martensite. Even though not the entire region of the second track undergoes melting from the heat of its neighboring track, it does reach a

temperature higher than the austenization temperature, thereby transforming every phase (along with newly solidified material) to austenite and then to martensite upon cooling.
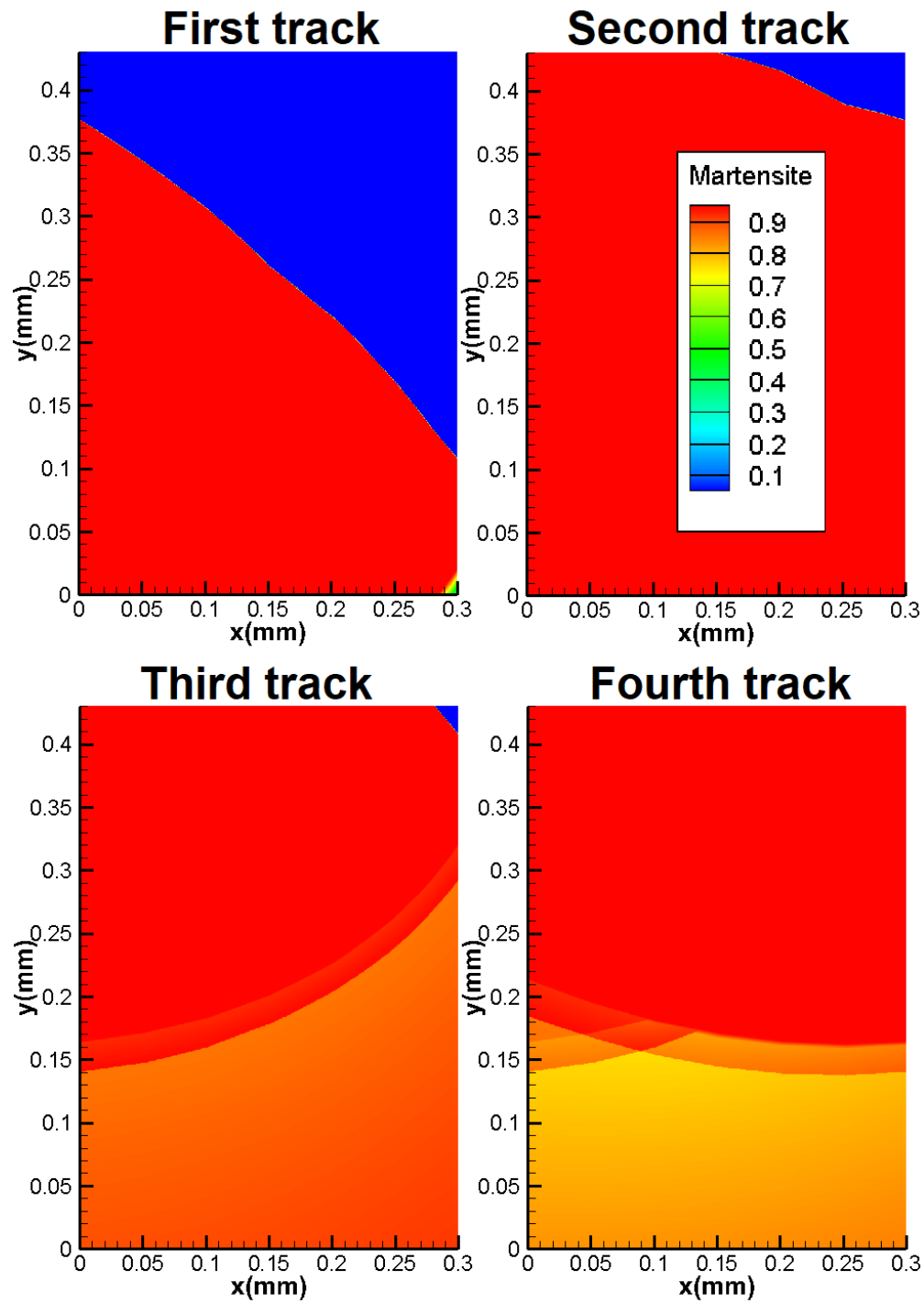
Figure 3.34: Predicted martensite phase fraction of each track after each simulation.

A region within the third track undergoes a heating cycle from its upper neighbor, where the peak temperature is not high enough to cause austenization but is high enough to temper the existing martensite, as can be seen in the lower half of the third track image of Figure 3.34 where the phase fraction of martensite has dropped below 90%. Additionally, the heat from a more distant neighboring track further tempers the martensite in the fourth track's region, resulting in an even lower phase fraction of martensite below 80%.

According to the model, the tempered martensite forms three phases: ferrite, ϵ-carbide, and cementite. The phase fraction of cementite is shown in Figure 3.35 where it can be seen that the degree of tempering increases between tracks three and four.
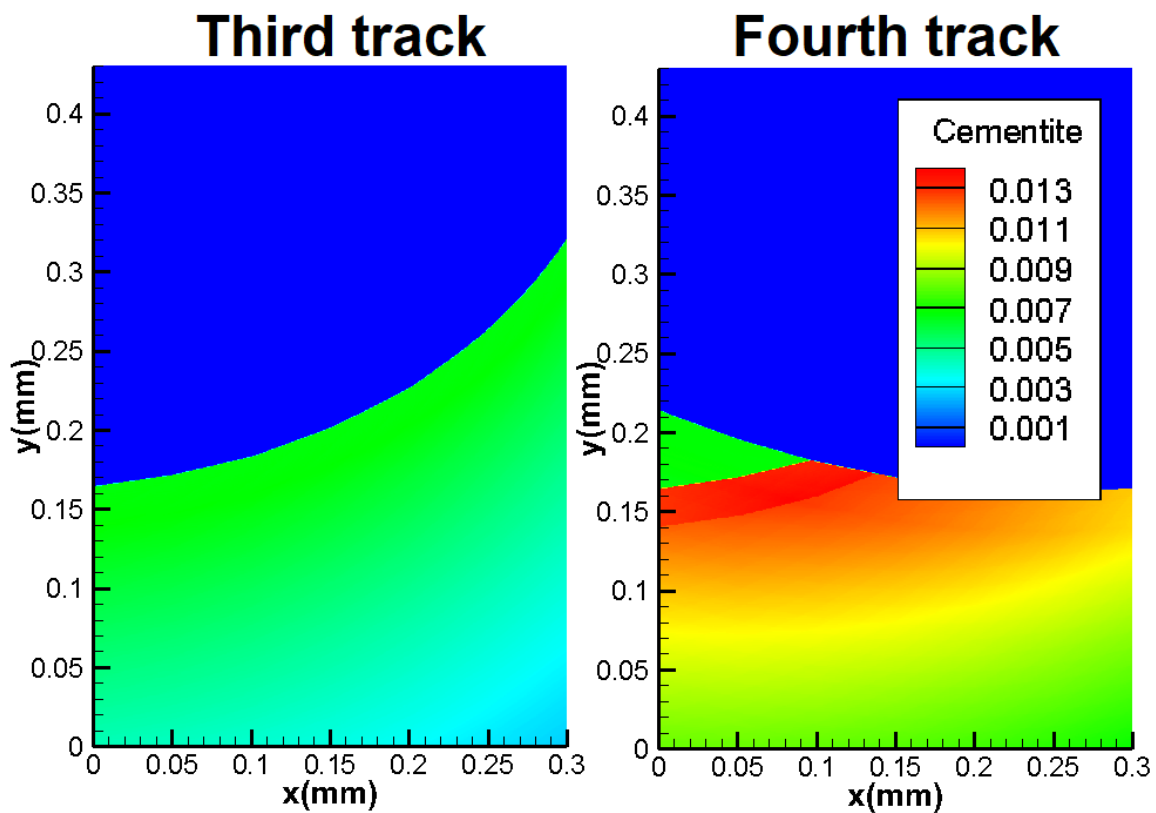
Figure 3.35: Predicted cementite phase fraction after tracks 3 and 4.

To validate the solid phase transformation model, the hardness field was calculated for the domain shown in Figure 3.34 and Figure 3.35 according to Eq. 2.7 and compared to the experimental sample's measured hardness. Using a Vickers indenter, the hardness in the region of the sample shown in Figure 3.31 was tested across a 12 $\times$ 10 grid where each indentation was spaced 0.075 mm across a 0.900 $\times$ 0.750 region under 200 g load for 13 seconds, as shown in Figure 3.36. The measured hardness field data is shown in Figure 3.37 while the predicted hardness field data and the measured hardness field data are compared in Figure 3.38. Note that Detail C represents the same region in Figure 3.36, Figure 3.37, and Figure 3.38.
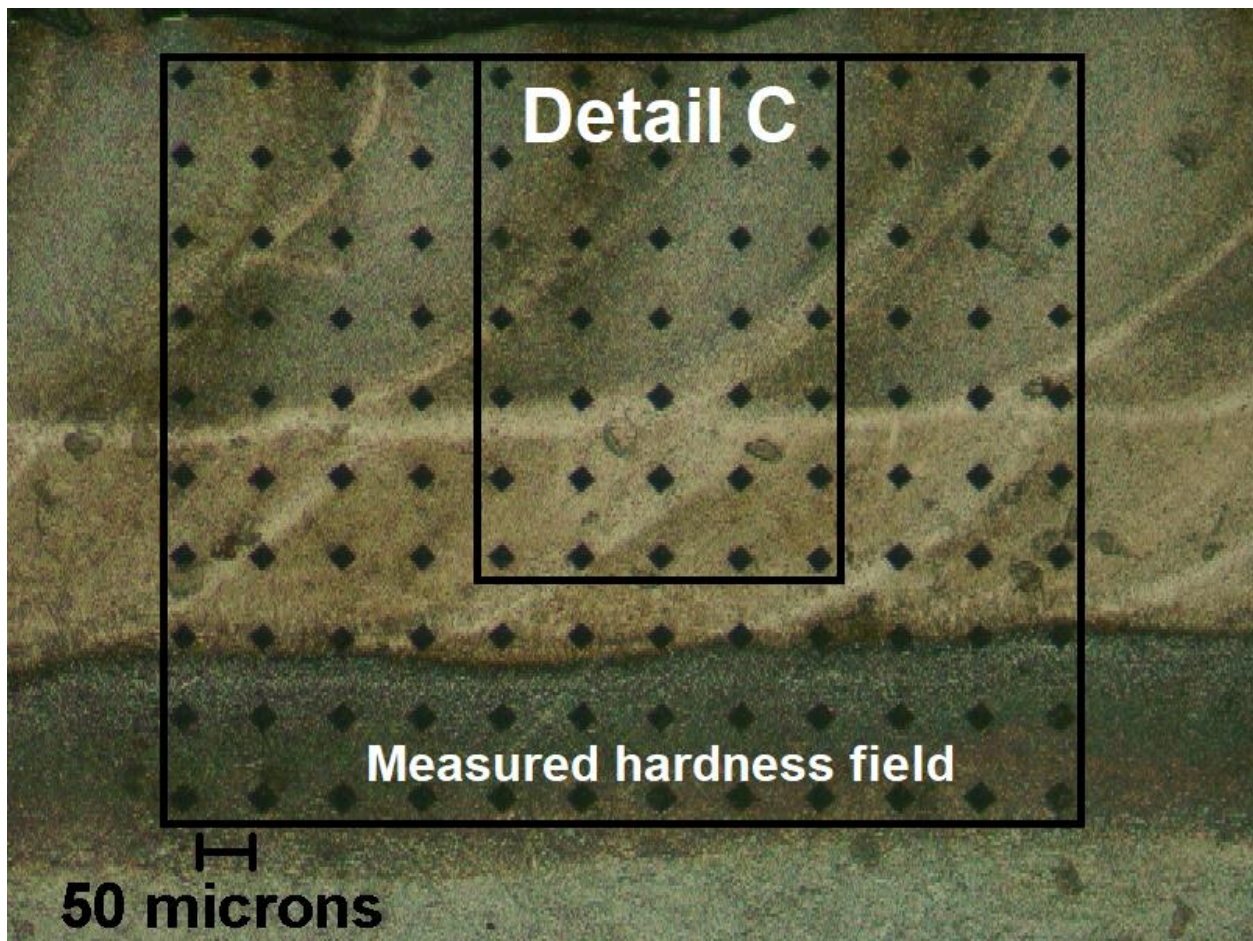
Figure 3.36: Vickers hardness indentation field (75 µm spacing).
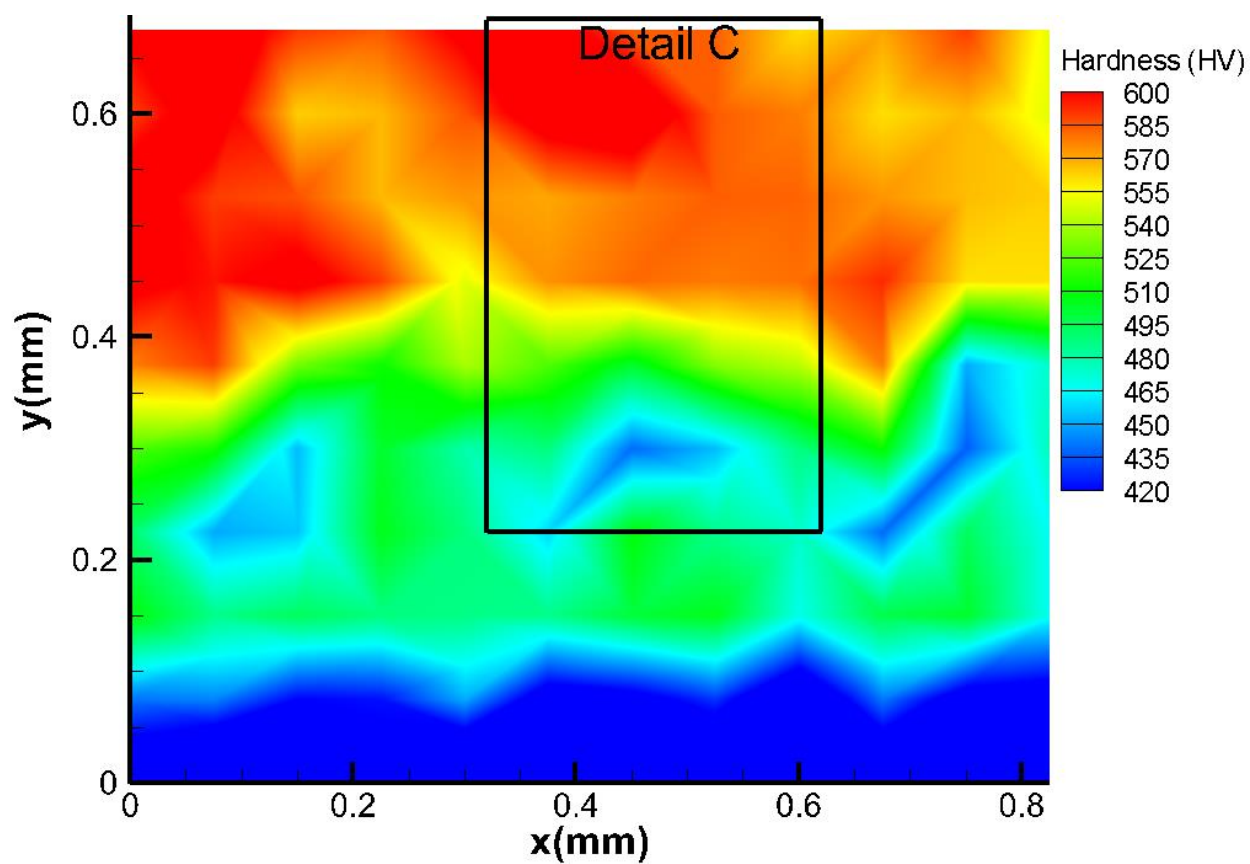
Figure 3.37: Measured hardness field (Vickers) corresponding to the region indicated in Figure 3.36.
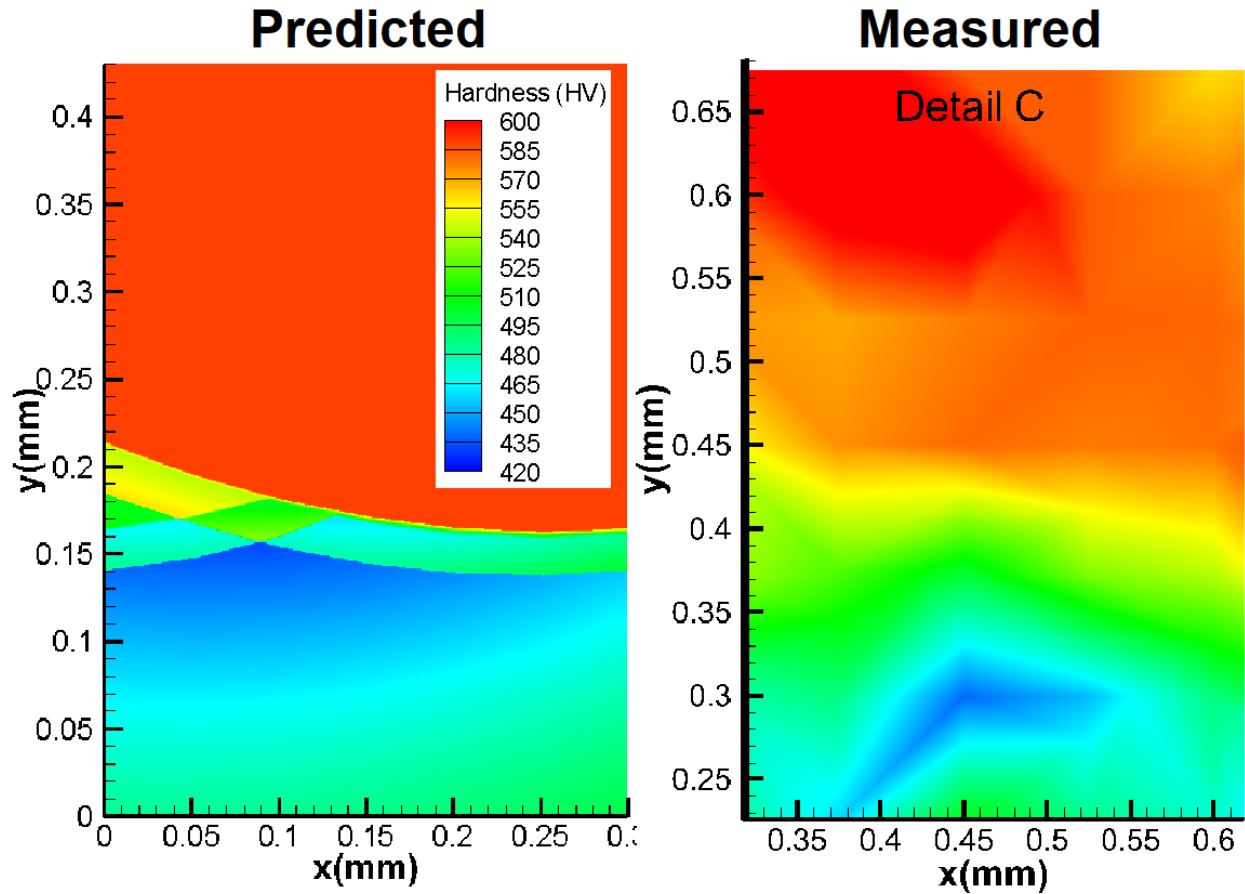
Figure 3.38: Predicted (left) VS measured (right) hardness fields.

From the measured hardness field data in Figure 3.37, it is shown that the top layer of deposited material is rather hard, ranging between 570 HV and 600 HV, which matches well with the predicted value of 589 HV. This corresponds to published data on typical H13 working hardness of 52-54 HRC (Benedyk, 2008). Due to tempering from the top layer, the lower layer is softer, ranging between 550 HV and 430 HV. Additionally, it can be seen from the measured hardness field in Figure 3.37 that the hardness field within the lower layer is horizontally periodic. Between 0.20 mm and 0.35 mm along the y axis, there are three softer regions spaced along the x-axis at 0.15 mm, 0.45 mm, and 0.70 mm where the maximum amount of tempering occurs from each top-layer track. The measured and predicted hardness in these soft spots match well at

around 435 HV. Overall, the predicted hardness data matches well with measured hardness data, as can be seen from Figure 3.38, validating the phase data shown in Figure 3.34 and Figure 3.35.

3.2.3.3.2 3D Phase Transformation Prediction via ABAQUS subroutine

Using the temperature and level-set data from the Laser Deposition model, a multi-track, multi-layer finite element simulation was run to predict the residual stresses that form during LDD. The simulation consists of 2 layers of 8 tracks each. The thickness of the substrate, like that of the Laser Deposition model discussed above, was 5 mm. The distance between tracks was 0.3 mm and the width and length of the square 8-track domain were 2.1 mm (the first and last tracks of each layer were partial tracks). The width of each element was 50 µm and the height of each element was 25 µm.

The time duration for each track was exactly 1 second. At 14.85 mm/s, the laser traveled 14.85 mm for each track. Since the length of the domain was only 2.1 mm, the laser spot spent most of the simulation time outside the computational domain, but the temperature field far from the laser spot still had a strong influence on the thermal strains and phase strains. Since the temperature influence from subsequent tracks can temper the martensite produced by previous tracks, the simulation time for each layer was extended to 15 seconds; 7 seconds after the 8th track has finished. The orientation of the tracks in the 2nd layer was perpendicular to those of the 1st layer. An image of the predicted temperature field during the 3rd track was shown in Figure 3.39.
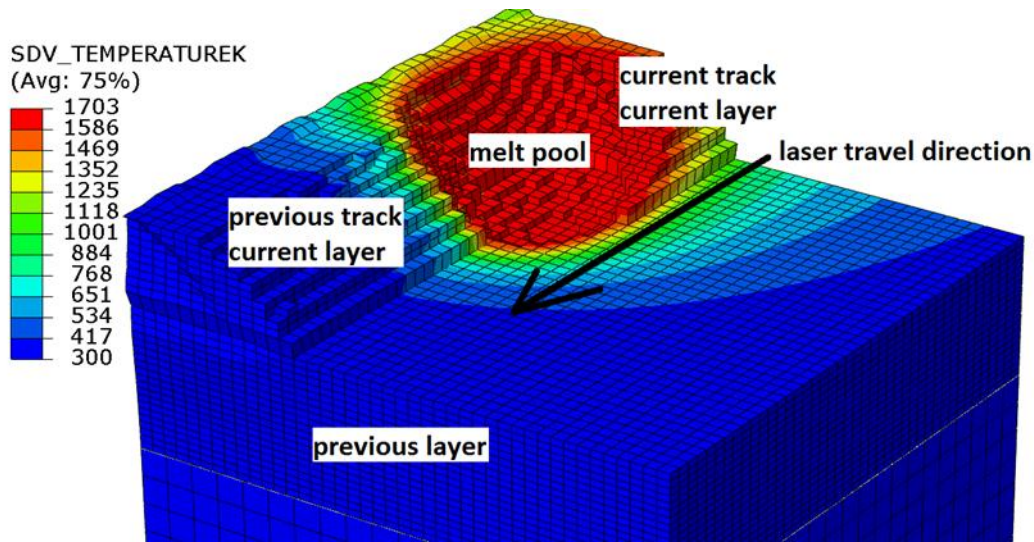
Figure 3.39: Temperature field during 3rd track.

The elements shown in Figure 3.39 were the currently active elements for the current ABAQUS step. During each step as the laser advanced, a set of elements near the front of the melt pool were deactivated due to melting and a set of elements near the back of the melt pool, including elements of the deposition layer that were deactivated during the first step, were reactivated due to solidification.

Phase transformation was calculated during each time increment, including heating, cooling, and tempering as discussed above. From an image of the phase fraction of martensite during the 3rd track of the 1st layer (shown in Figure 3.40), one can see that during deposition of the 1st layer, the bulk of the manufactured component substrate had no martensite. After a laser track passed, the material cooled to martensite (as seen in the left front side), some of which was transformed back to austenite as the next track's laser passed.
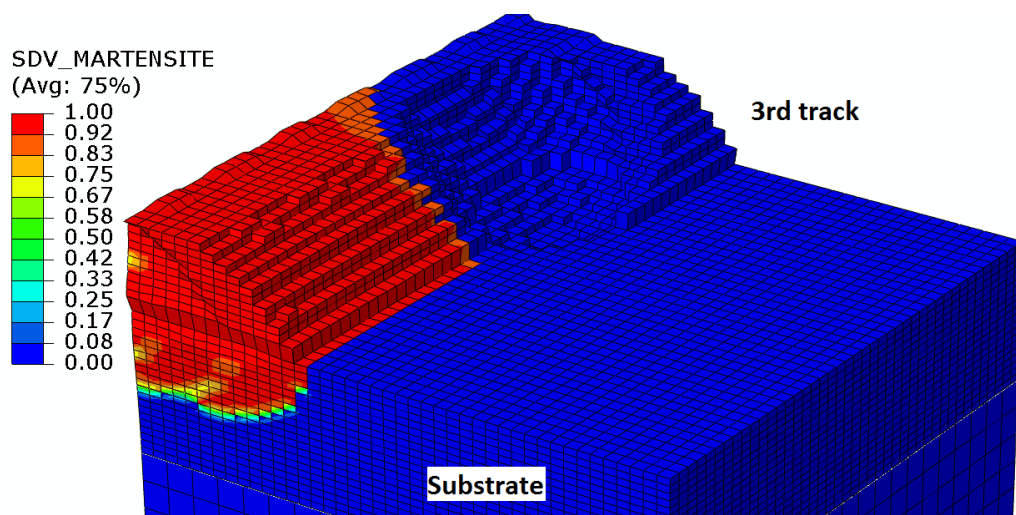
Figure 3.40: Phase fraction of martensite during the 3rd track of the 1st layer.
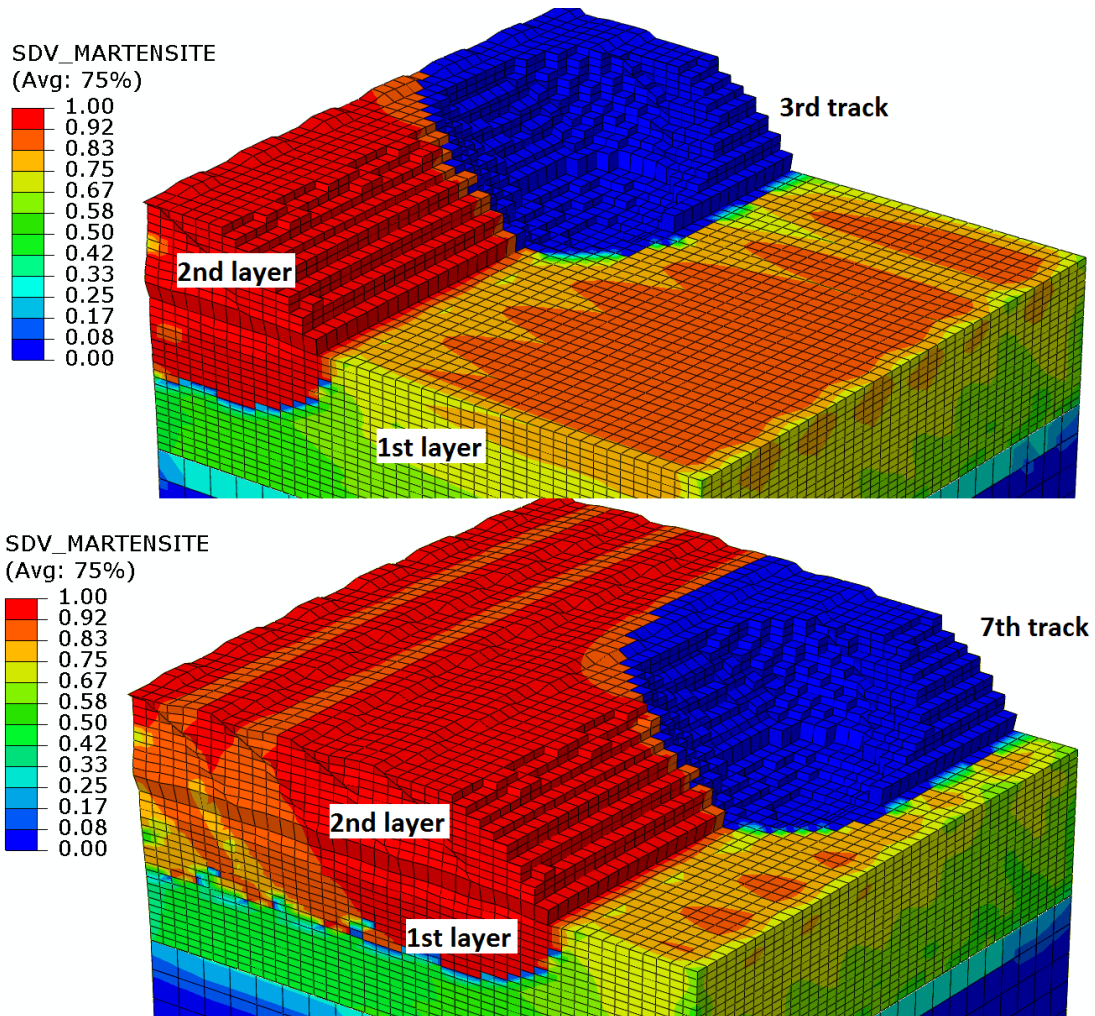
Figure 3.41: Phase fraction of martensite during the 3rd (top) and 7th (bottom) tracks of the 2nd layer.

Images of the phase fraction of martensite during the 3rd and 7th tracks of the 2nd layer are shown in Figure 3.41. From Figure 3.41, one can see that during deposition of the 2nd layer, the material deposited by the 1st layer had a varying amount of martensite. As each track passed a previous track, the heat from the current track tempered (to some degree) the previous track and previous layer. This effect can clearly be seen in the bottom image of Figure 3.41. The previous tracks near the left of the image had a lower martensite phase fraction than the track that had

most recently passed. The material of the 1st layer, below the recently deposited tracks, had an

even lower phase fraction of martensite because it had also been tempered by the 2nd layer.

Hardness measurements from a single-layer multi-track sample were used to validate the solid-

state phase transformation model. At the end of the simulation of the 1st layer, the material

hardness was calculated for each element in the finite element mesh according to Eq. 2.7. The

predicted hardness field is shown as a 3D surface plot in Figure 3.42 as a function of both

distance parallel to the surface and depth from the surface. Notice that the dark peaks in Figure

3.42 represent the hardest material near the surface of the sample, and clearly show a pattern of

hardness repeating in the parallel direction. This repeating pattern represents the tempering that

is experienced by each laser track. The width between each laser track is 300 μm, which is the

same width of the hardness pattern shown in Figure 3.42. As depth into the sample increases, the

hardness value decreases sharply.
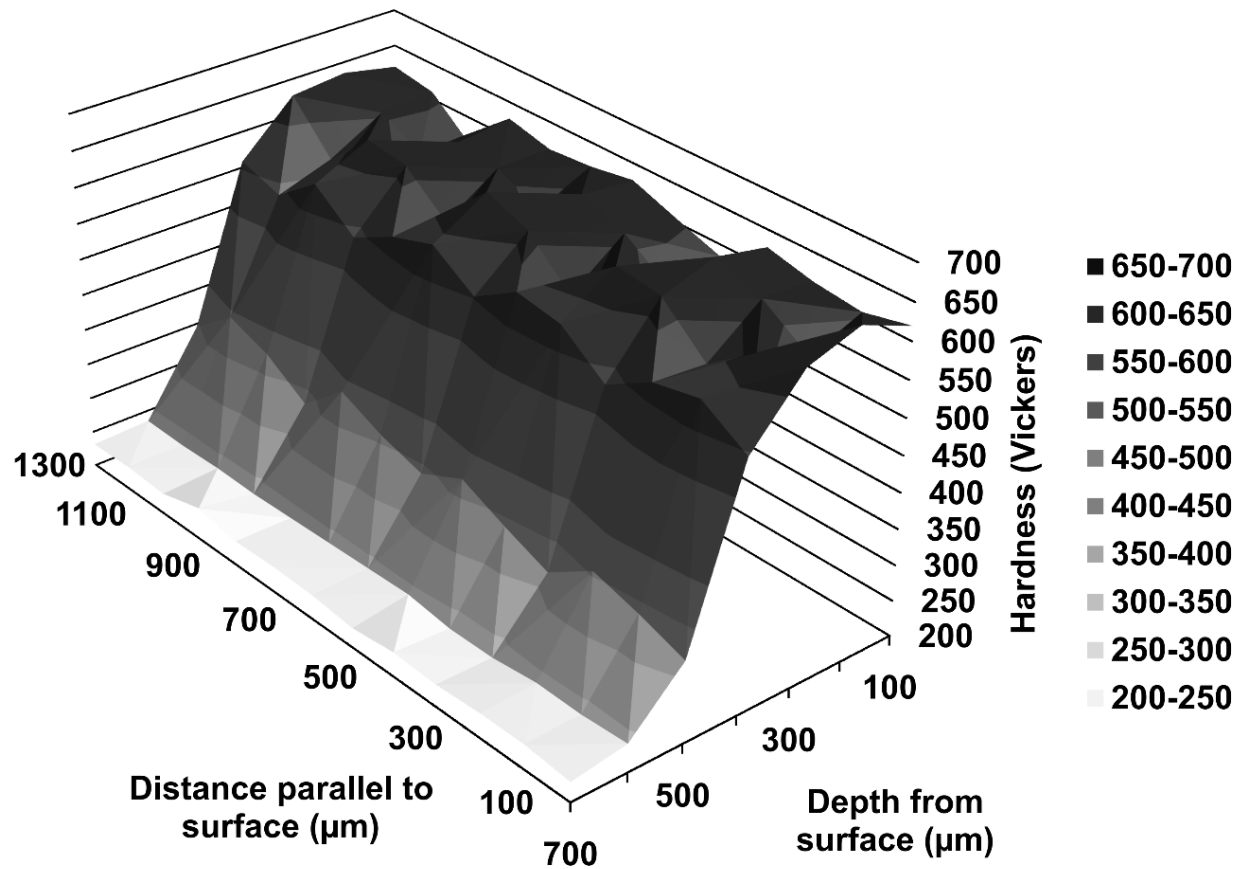
Figure 3.42: Predicted hardness field.

The sample was sectioned and polished in preparation for hardness measurements, then indented with a uniform grid of 7 rows and 13 columns (with grid spacing of 100 µm), as shown in Figure 3.43. The automatic measurements were made with a Vickers indenter, a load of 200-gram force, and a load time of 13 seconds. To show repeatability, the same measurement grid was performed at three separate locations along the sample cross-section.
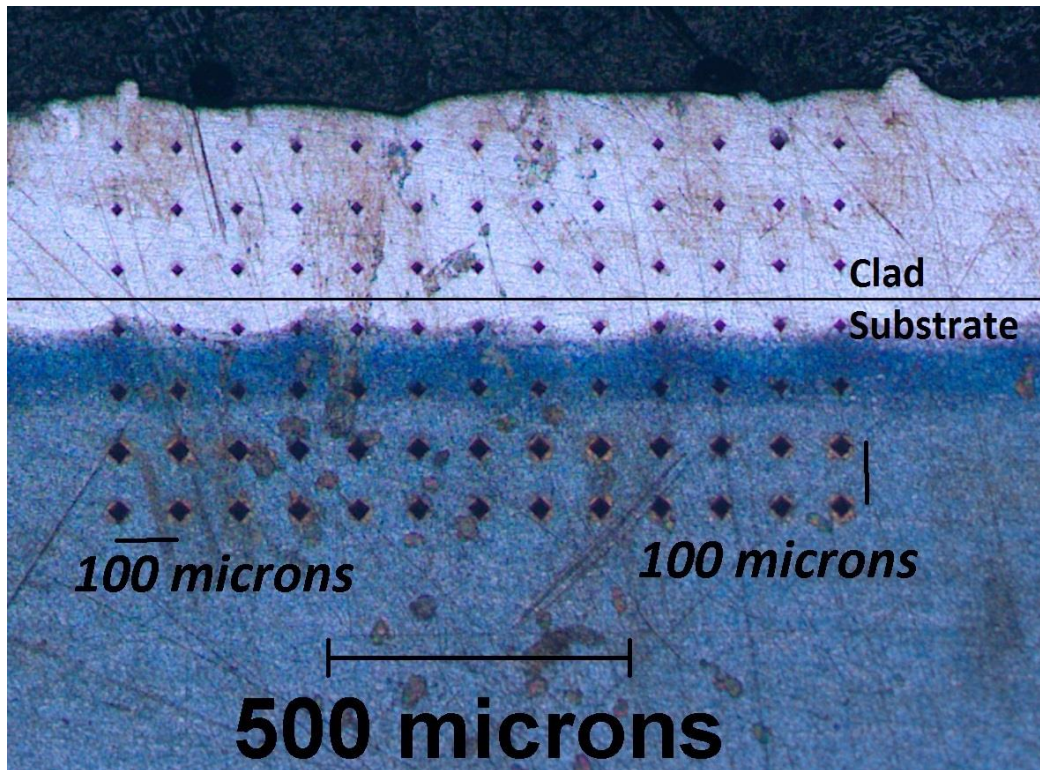
Figure 3.43: Cross-section of a single-layer LDD sample showing the hardness measurement grid.

Hardness values predicted by the solid-state phase transformation model are compared with the measured values in Figure 3.44. Each hardness comparison graph shows a line of measured and predicted values at given depths of 100 µm, 300 µm, and 500 µm below the sample's surface. The measured values shown in these graphs are the average values of the three separate measurements; the error bars show the maximum and minimum values of the three measurements at each location. The predicted values match the magnitude and the general trend of the horizontally varying patterns of the measured values.
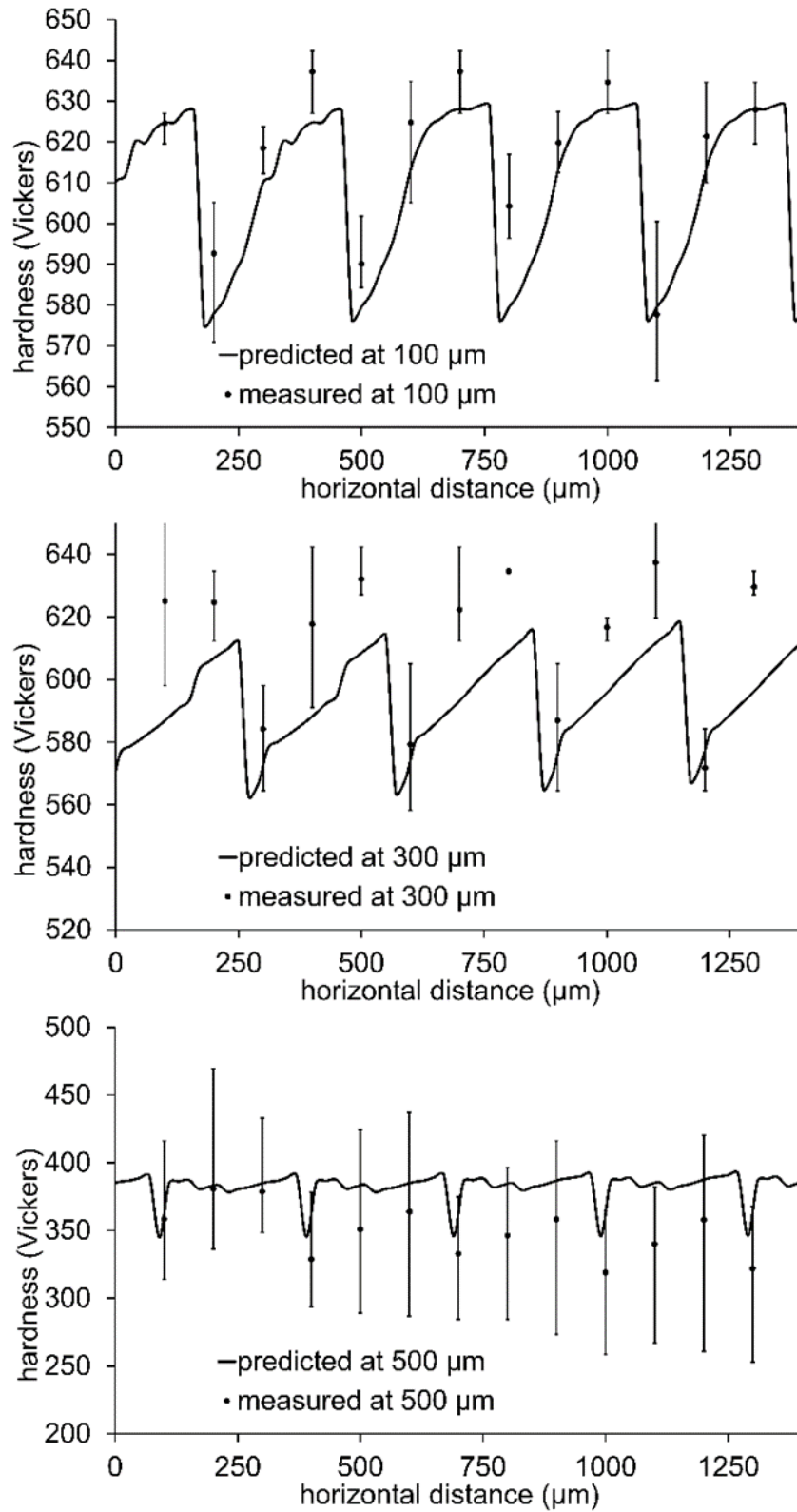
Figure 3.44: Predicted versus measured hardness at 100 µm (top graph), 300 µm (middle graph), and 500 µm (bottom graph) below the top deposition surface.

3.2.3.4   Residual Stress

As mentioned in Section 2.2, a Johnson-Cook hardening model was used to model the plastic strain during laser processing. A list of Johnson-Cook coefficients for H13 tool steel as reported by Shatla et al. (2001) are shown here in Table 3.7.

Table 3.7: Johnson-Cook hardening model coefficients for H13 tool steel (Mahmoud Shatla et al., 2001).

A	B	n	m	T_{melt}
674.8 MPa	239.2 MPa	0.28	1.3	1700 K

The elastic strain is dependent on the material's Young's modulus and Poisson's ratio, and both are functions of temperature. According to the High Performance Alloy Database by CINDAS (Benedyk, 2008), the Poisson's ratio of H13 steel at room temperature is 0.28, but increases with temperature in a nonlinear fashion, approaching 0.3 at 800 K and 0.33 at 1000 K. Philip and McCaffrey (1997) reported the Young's modulus of H13 as a function of temperature up to 800 K, while Bohler-Uddeholm Corporation (2016) reports the Young's modulus of their commercial H13 steel at higher temperatures up to 1300 K. Both the Poisson's ratio and the Young's modulus of H13 used in this study are shown in Figure 3.45 as functions of temperature.
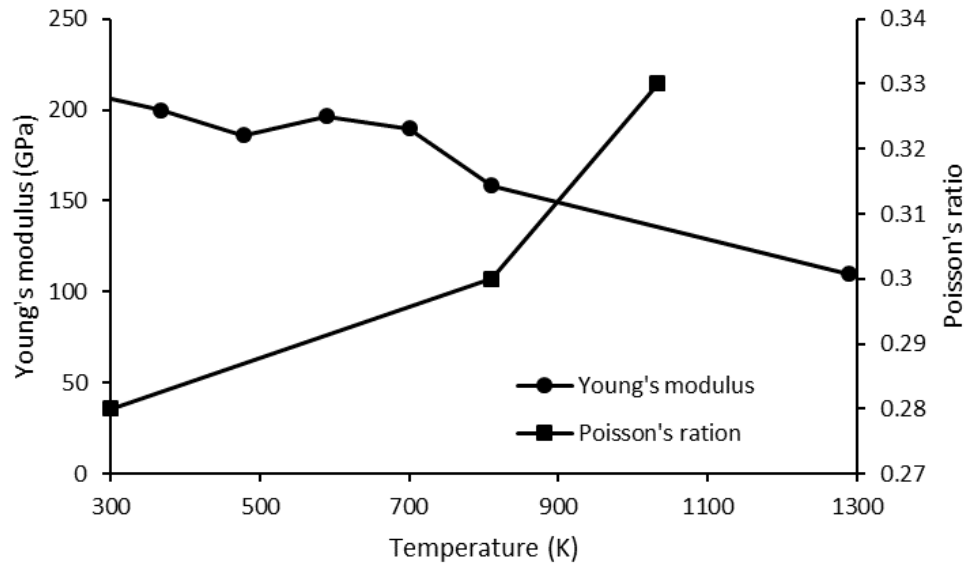
Figure 3.45: Young's modulus and Poisson's ratio from Bohler-Uddeholm Corporation (2016) and Philip and McCaffrey (1997) as functions of temperature.

A section view of the predicted transverse stress field after the simulation of the 2nd layer is shown in Figure 3.46 (transverse stress component is in the direction perpendicular to the laser travel direction of the top layer and parallel to the surface).
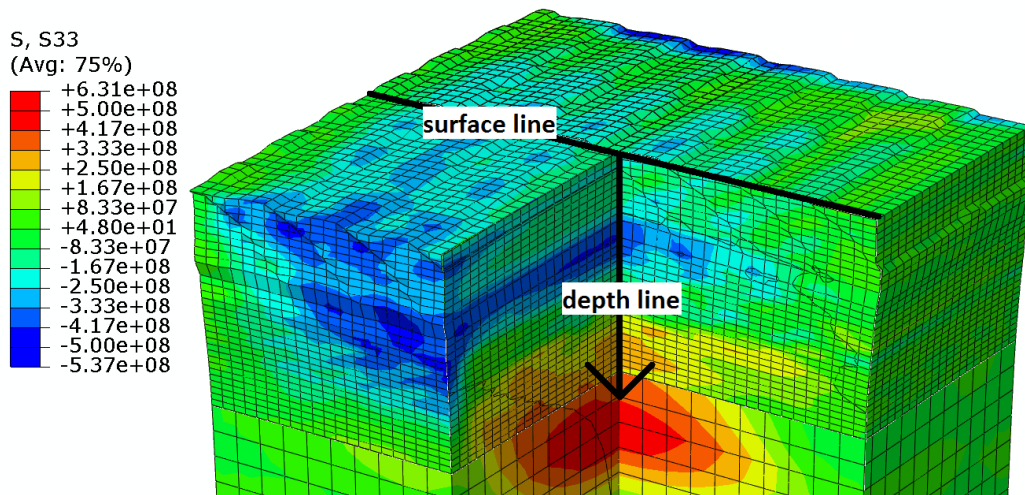
Figure 3.46: Section view of the predicted transverse stress component of the two-layer simulation.

Two lines are shown in Figure 3.46—the surface line and the depth line. To validate the residual

stress model, the same transverse stress component was measured using the X-ray diffraction

technique on two different LDD samples (two samples were used to demonstrate repeatability) at

5 and 7 locations, respectively, along the depth line of the two-layer samples. The transverse

stresses of the samples were measured at the surface where the surface line and the depth line

intersect; the samples were then electropolished (so that no additional stress was introduced) to

subsequent depths along the depth line. The transverse stress was measured at each depth. The

predicted and measured transverse stress values are compared in Figure 3.47 for stresses along

the depth line and in Figure 3.48 for stresses along the surface line.
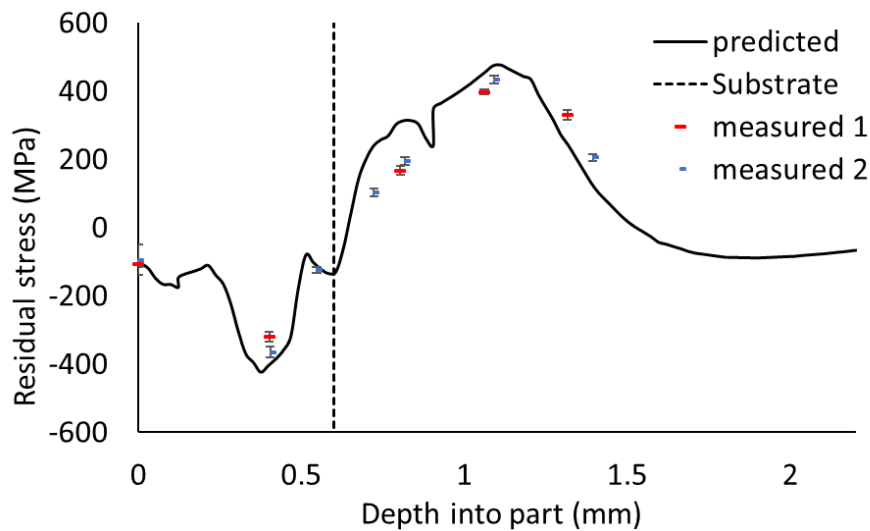
Figure 3.47: Predicted vs. measured transverse stress taken along the depth line of Figure 3.46.
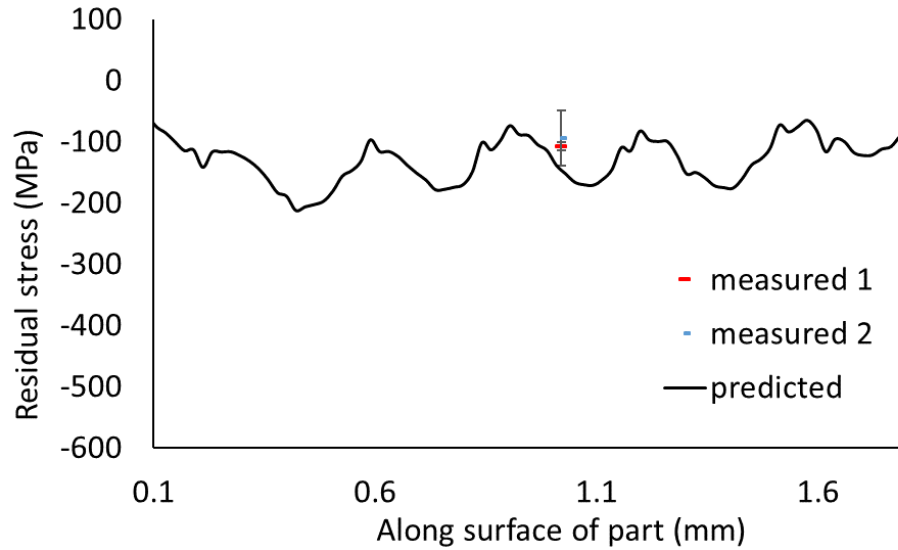
Figure 3.48: Transverse stress profile taken along the surface line of Figure 3.46.

The predicted stress values match reasonably well with measured values. From Figure 3.47 and

Figure 3.48, it is clear that a compressive stress exists near the surface of the sample that

increases with depth to a value of -400 MPa. As depth increases, the residual stress becomes

tensile up to a value of +400 MPa. This general trend of compressive stress followed by tensile

stress as depth increases is primarily due to thermal strains experienced in the sample. As shown

in Figure 3.48, the compressive stress varies between -100 MPa and -150 MPa along the surface.

This compressive stress near the surface is primarily due to the high martensite content of the

material. The periodic variation of stress along the surface is due to the periodic tempering of the

martensite from the multiple tracks of the 2nd layer.

3.3   Laser Welding of AL 6061

During laser welding, the work piece experiences a very complex and dynamic temperature field

with steep temperature gradients and high heating and cooling rates. In order to accurately model

the microstructure development during solidification in laser welding, the temperature field of

the PF domain cannot be assumed to be isothermal or to follow a mathematical expression. The experimentally validated welding model developed in the authors' group (Wenda Tan et al., 2013) is used to predict the temperature field within the PF domain.

3.3.1 Thermal Model Results

A 3D PF simulation and two 2D PF simulations have been run to predict the dendrite growth during laser welding of Al 6061 aluminum alloy with the welding parameters listed in Table 3.8.

Table 3.8: Welding parameters for simulations and experiments.

2 mm thick substrate bead-on-plate weld
800 W laser power from fiber laser
(1077 µm in wavelength, 240 µm in focal diameter)
500 mm/min welding speed

The mechanical behavior of aluminum alloy Al 6061 (composition is given in Table 3.9) is affected by the precipitation hardening of the Mg_2Si secondary phase. Therefore, in order to simulate the solidification of AL 6061, both magnesium and silicon ought to be considered. However, PF simulations considering thermodynamics of multicomponent alloys are computationally more expensive than the case of binary alloys. One method to mitigate the computational cost is to reduce multicomponent systems to pseudo-binary systems.

Table 3.9: Composition of Al 6061 in wt.%.

Element	Composition
Mg	0.8-1.2
Si	0.4-0.8
Cr	0.04-0.35
Mn	0.15 max
Ti	0.15 max
Cu	0.15-0.4
Zn	0.25 max
Fe	0.7 max
Al	balance

Using Gibb's energy calculations and experimentation, Zhang et al. (2001) developed a pseudo-binary phase diagram for the Al-Mg_2Si system, shown in Figure 3.49. During isothermal solidification of Al 6061, the primary α phase (Al) solidifies over the entire domain before the secondary β phase (Mg_2Si) begins to solidify within inter-dendritic regions where the solute was left behind in high concentrations. During PF simulations, the amount of solute rejected into the liquid at the solid-liquid interface is determined through the system thermodynamics: For a multicomponent alloy, the CALPHAD equations and equilibrium equations are used to solve for equilibrium concentrations, but for a binary (or pseudo-binary) alloy, only the phase diagram is needed.
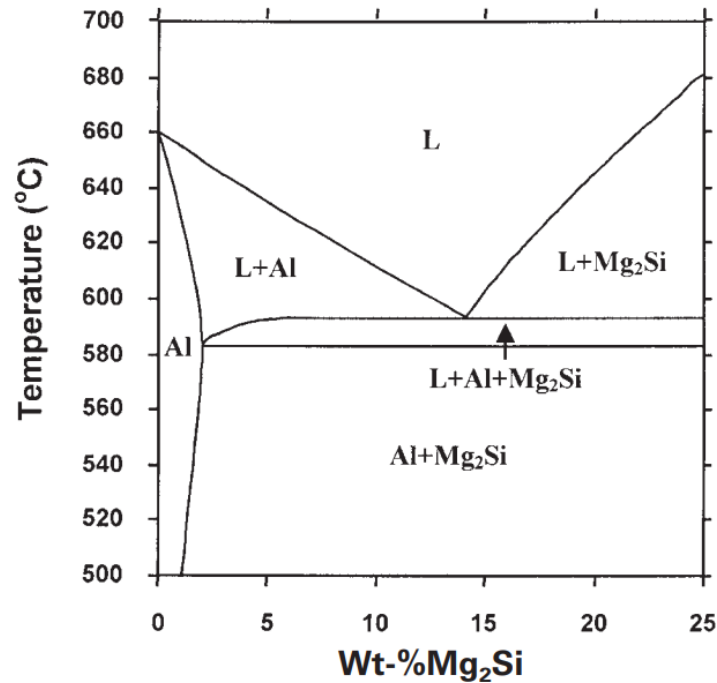
Figure 3.49: Pseudo-binary phase diagram for Al-Mg2Si (Zhang et al., 2001).

In this study, the partition coefficient was taken from the pseudo-binary work diagram presented by Zhang et al. (2001) as well as the average diffusion coefficients of Mg_2Si in liquid and solid Al, in the simple binary PF model. The material parameters used for all PF simulations are listed in Table 3.10. The biggest advantage of the pseudo-binary approximation is the computational cost, which will allow for a larger simulation domain in both 2D and 3D PF models. The disadvantage is that the magnesium and silicon are always tied together in a ratio of 2 to 1, i.e., they cannot diffuse separately throughout the domain.

Table 3.10: Material parameters for Al-Mg$_2$Si pseudo-binary alloy.

Material parameters	Symbol	Value	Unit
Diffusivity in solid	D_S	3.0E-09	m^2/s
Interface energy	σ	0.093	J/m^2
Molar volume	V_M	1.05E-05	m^3/mol
PF mobility	M_ϕ	0.1	m^3/s·J
Diffusivity in liquid	D_L	3.0E-13	m^2/s

The temperature data used by the PF simulations are taken from the results of a welding model simulation which was run using the same welding parameters listed in Table 2 (laser power, welding speed, material properties, etc.). Due to computational necessity, the PF computational domain is much smaller than the welding model's computational domain. Since the purpose of the PF model is to predict the dendrite growth and micro-segregation during solidification, the initial location of the PF simulation domain was chosen near the back edge of the melt pool where solidification will begin as shown in Figure 3.50. The PF simulation's domain size is 28 µm×14 µm×8 µm while the welding model simulation's domain is much larger.
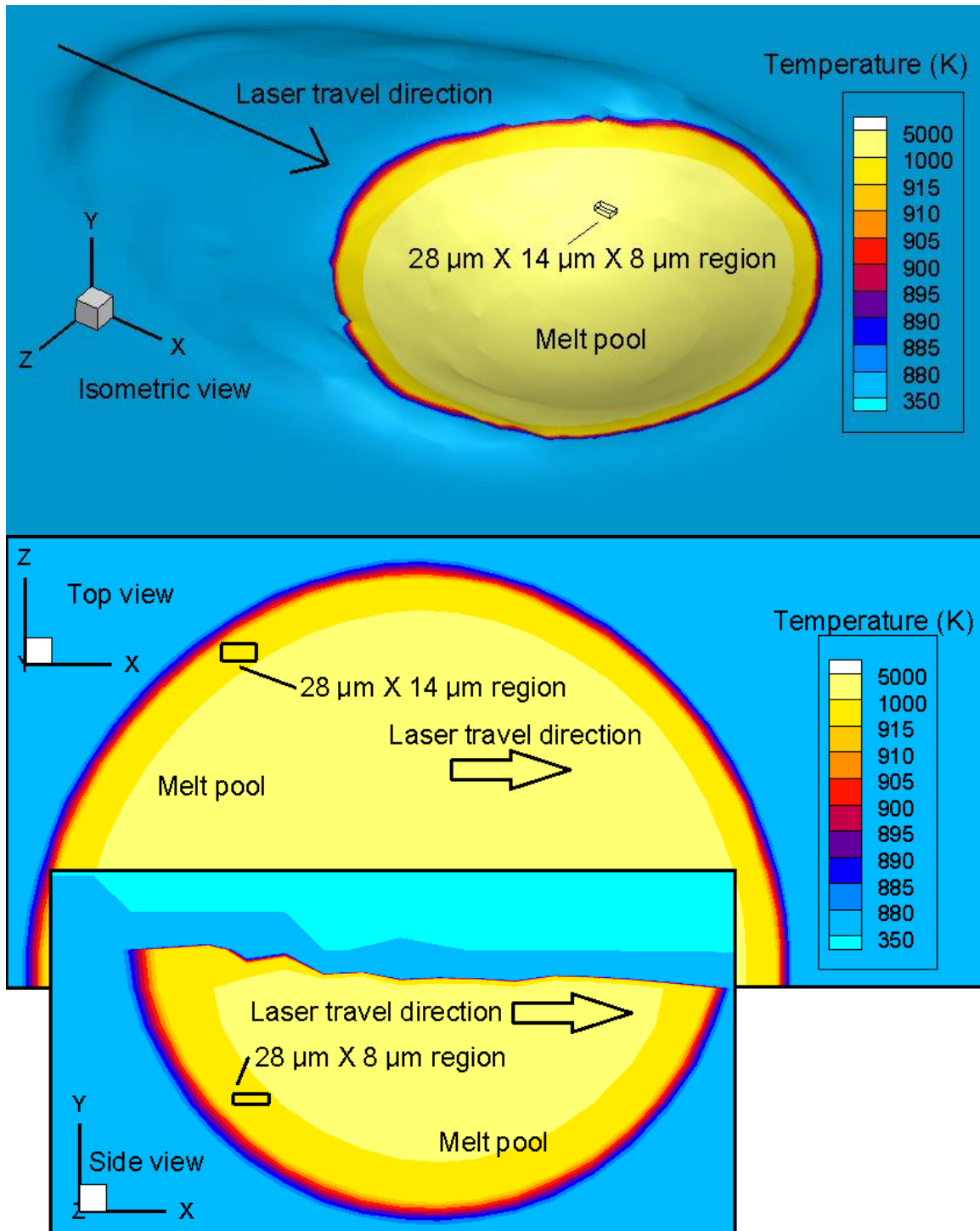
Figure 3.50: Three views (isometric, top, and side) of master temperature field taken from the welding simulation showing the 3D PF model domain. Laser travel is in the x direction.

During the PF simulations, since the mesh sizes are different between the welding and PF models, temperature data are interpolated from the welding model results onto the 3D PF mesh. The temperature file from the welding model is first read into the PF model. At each time step of the PF model, the temperature at each mesh point in the PF domain is interpolated from the welding model data at its current location. As the laser travels along the laser travel direction, the relative position of 3D PF domain with respect to welding model domain changes. As a result, the temperature values inside the 3D PF domain begin to drop below the solidus temperature during solidification. To help illustrate this, the position of the PF domain shown in Figure 3.50 is the initial position of the PF domain where the entire domain is in the melt pool, while the final relative position of the PF domain will be past the edge of the molten pool, well into the mushy zone. This is necessary to allow for solidification. As interpolated from the initial position of the temperature field of the welding model domain with respect to the PF domain, the initial temperature field of the PF domain for all following 2D and 3D simulations is shown in Figure 3.51.

As time advances, the temperatures in the PF domain will decrease, according to the cooling curve at each cell as predicted by the welding model. The temperature field values from the welding model vary between room temperature (300 K) and 1400 K, but the temperatures in the PF domain, as can be seen in Figure 3.51, only vary between 905 K at Point D, and 995 K at Point E—temperatures near the solidus (855 K) and liquidus (925 K) of the Al 6061 alloy. The strongest thermal gradient within this domain is in the general direction of Point D to Point E. To help illustrate the cooling rates experienced within the PF domain, the temperature curves of four points A, B, C, and D from Figure 3.51 were tracked during the welding model simulation as shown in Figure 3.52. Only the solidification range of temperature was chosen for the PF

domain, as indicated in Figure 3.52. The cooling rates inside the PF domain are approximately

15,000 K/sec between liquidus and solidus temperatures.
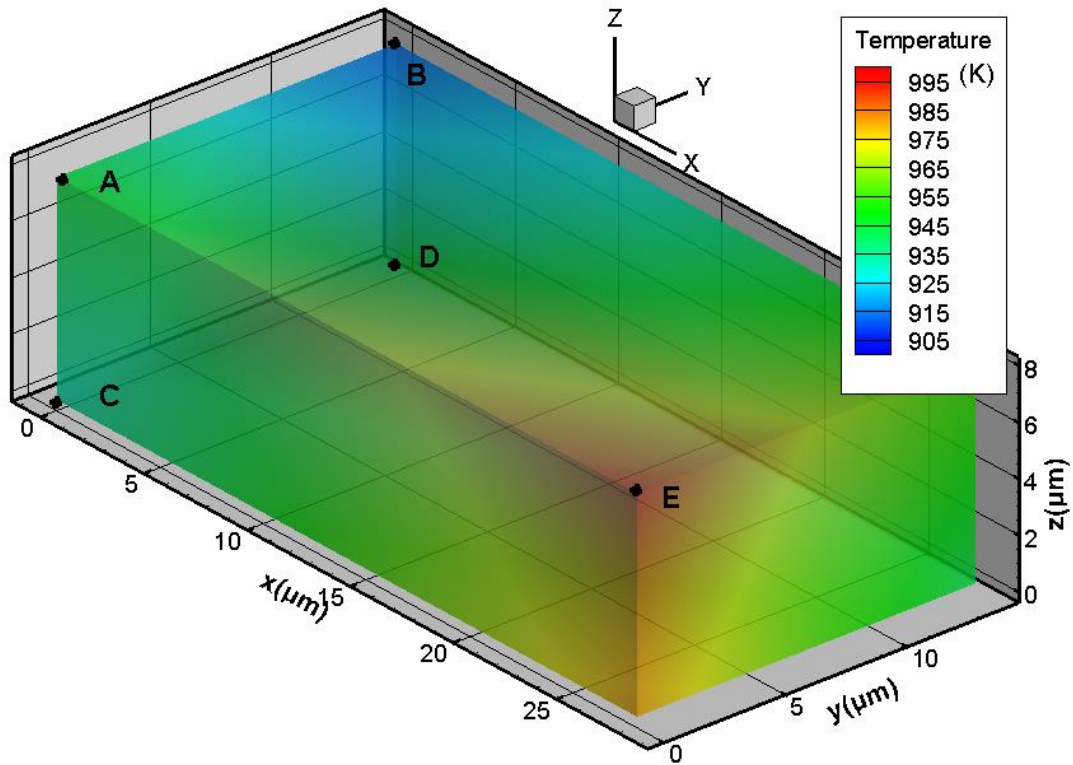
Figure 3.51: Initial temperature field for all remaining 2D and 3D simulations of the PF model interpolated from welding model results. Temperature gradient is in the direction pointing from D to E.
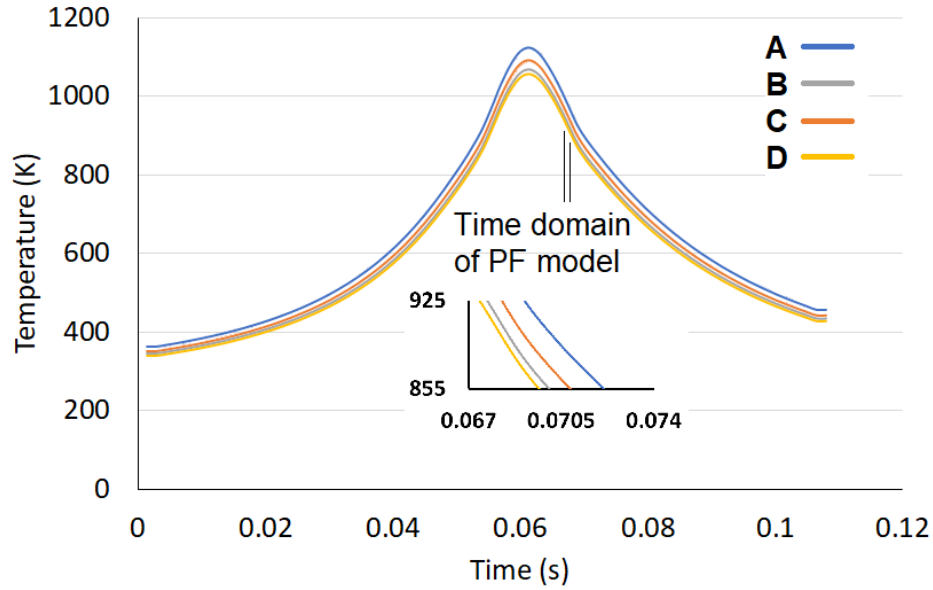
Figure 3.52: Temperature profiles of points A, B, C, and D from Figure 3.51. The indicated portion represents the time domain and the temperature extremes of the PF domain during the PF simulation.

3.3.2 3D Phase Field Simulation and Results

A 3D PF simulation was run using the temperature data from the welding model and the PF domain as shown in Figure 3.50. The uniform mesh consisted of 392,558,400 cubic cells of size 0.02 µm. The uniform time step was set at 1.0×10^{-8} s. In total, 0.0051 seconds of simulation time were calculated (510,000 time steps), requiring 60 days of computation time on 20 2.6 GHz processors.

A progression of images illustrating the advancement of the dendrites and the development of the solute concentration field is shown in Figure 3.53, where images (a) through (f) show the dendrite growth at the indicated times. Figure 3.53(a) shows the initial dendrite seed field where randomly oriented seeds are placed randomly along the back two boundaries of the PF domain. From Figure 3.53(b) it is clear that some of the dendrite seeds near the back bottom corner of the

PF domain have grown substantially during the first 0.00012 seconds, while most of the dendrite seeds have melted due to the unfavorable thermodynamic conditions for solidification. As time progresses and the temperature continues to decrease, the solid portion continues to grow and branch into additional dendrite arms as shown by Figure 3.53(c) through Figure 3.53(f). It is clear from Figure 3.53 and Figure 3.54 that the dendrites are growing parallel to the temperature gradient (perpendicular to the isotherms). At the solid/liquid interface of each dendrite arm during solidification, much of the Mg_2Si solute dissolved in the aluminum melt is rejected from the solid dendrite arm into the liquid of the melt. As more Mg_2Si solute is rejected into the melt, the concentration of the solute in the liquid aluminum increases, creating a concentration gradient close to the solid/liquid interface along each dendrite arm. In the melt, the solute in higher concentration areas will naturally diffuse into lower concentration areas. The rejected solute near the tips of the growing dendrites will easily diffuse into the low concentration melt, but the rejected solute near the roots of the dendrites does not have access to a low concentration region and thus the solute accumulates until the concentration is too high for favorable solidification conditions of the primary phase. For Al 6061 alloy, these high concentration regions between the dendrites will be the last to solidify as a secondary phase (mostly Mg_2Si). This PF model does not consider solidification of secondary phases and so it was decided that the final frame of the simulation would occur when the entire domain consisted of dendrites with interstitial higher concentration solute, as shown in Figure 3.54. At this point in the solidification process, the dendrite arms will expand slightly as temperature drops rapidly and rejected solute increases the concentration of Mg_2Si in the interstitial melt. When the thermodynamic conditions for solidification are met for the secondary phases (primarily Mg_2Si), they will start to nucleate and solidify in the interstitial regions between the main dendrite arms of solid Al. However, the

overall shape of the microstructure will change very little after the point illustrated in Figure 3.54. Dendrite shapes and secondary dendrite arm spacing (SDAS) will not be strongly affected during solidification of secondary phases.
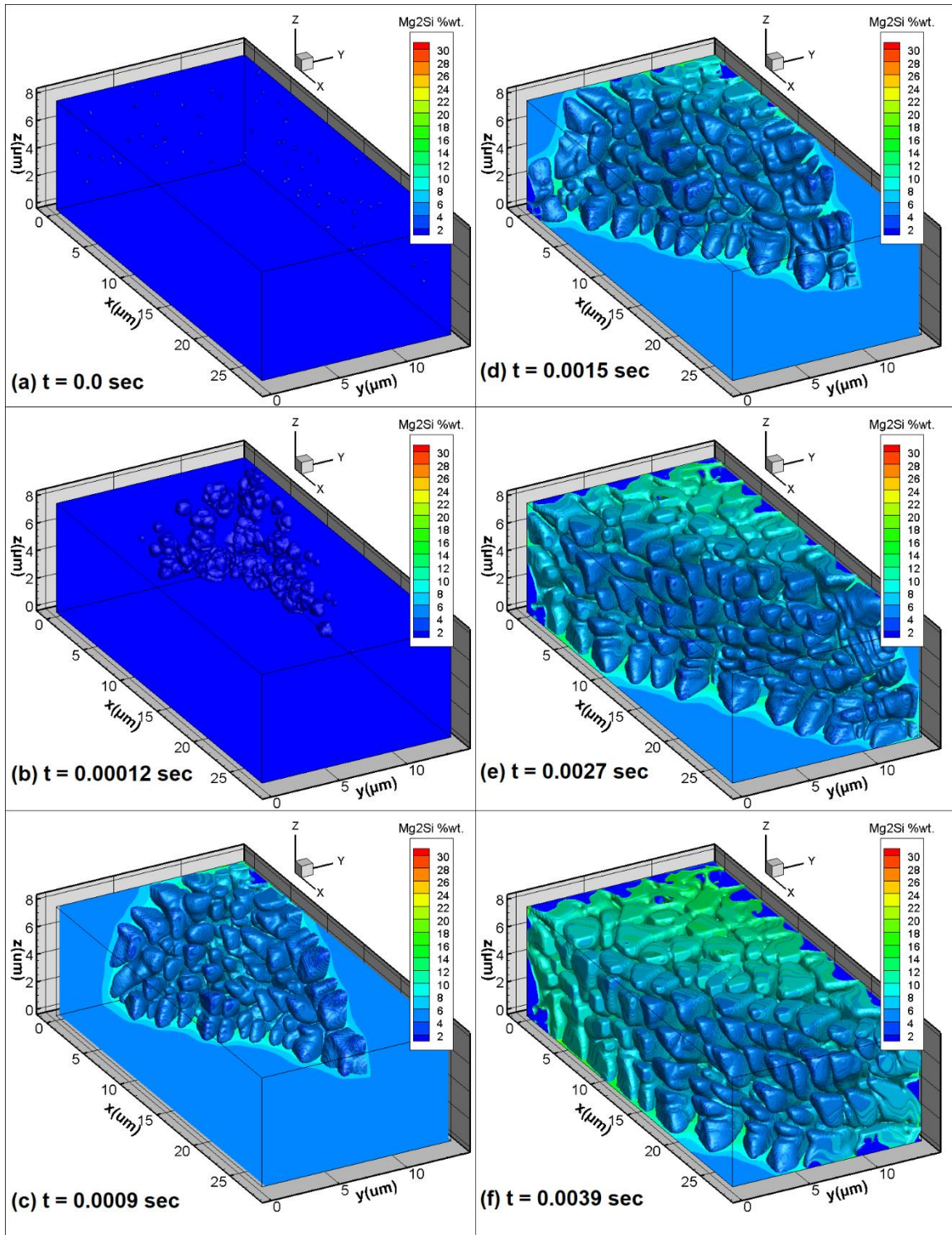
Figure 3.53: 3D PF model results showing progression of dendrite growth during solidification.
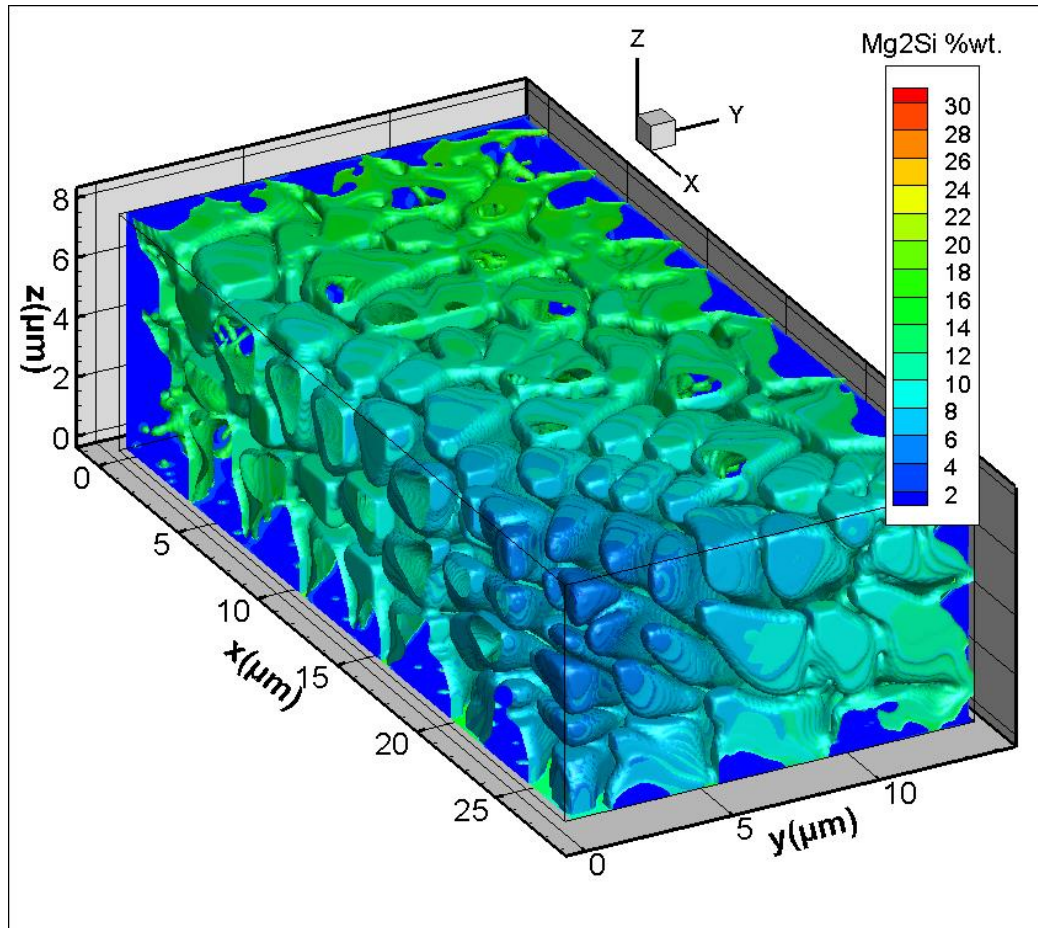
Figure 3.54: Completed 3D PF result after 60 days of computation on 20 processors.

During the solidification process, all dendrites are growing toward the strongest temperature and concentration gradients. In essence, each dendrite is competing with its neighbors for the lowest solute concentrations and temperatures. However, if a certain dendrite's crystallographic orientation is aligned with the concentration and temperature gradients, it will have a distinct advantage and will mechanically block the growth of a neighboring dendrite with a less favorable crystallographic orientation. As can be seen in the progression of images in Figure 3.53, this phenomenon, known as mechanical blocking or competitive growth, helps determine the primary dendrite spacing in columnar growth.

3.3.3   3D vs. 2D Simulations

Although 3D simulation results are superior to 2D results, 3D experimental results are not always available for use in validating 3D simulation results. Serial sectioning (Wojnar, 1998) is a time consuming and expensive process, and although the technology of 3D X-ray micro-tomography (Daudin et al., 2017) is approaching the resolution required for imaging the size of dendrites found in fast-cooling industrial processes, it is still an expensive means of microstructure analysis. Historically, microstructure analysis (sectioning, polishing, and etching of material samples) has been based on 2D images. Thus, to validate a 3D PF model, it may be best to compare a 2D cross-section of a 3D simulation result with an actual 2D micrograph from an experimental sample.

To make the comparison, two types of 2D PF predictive images were prepared via PF model simulations for comparison with three 2D micrographs: 2D cross-sections taken from the 3D PF simulation result and 2D PF simulation results performed at the same locations within the weld domain as the 2D cross-sections. Similar densities and locations of randomly oriented initial seeds of the 3D simulation were also used in the 2D simulations. The three cross-sectional locations where these analyses were performed within the 3D PF model domain (an X plane, a Z plane, and an oblique plane) are indicated in Figure 3.55. The 2D simulation results and 2D cross-sections from the 3D simulation results are compared in Figure 3.56.
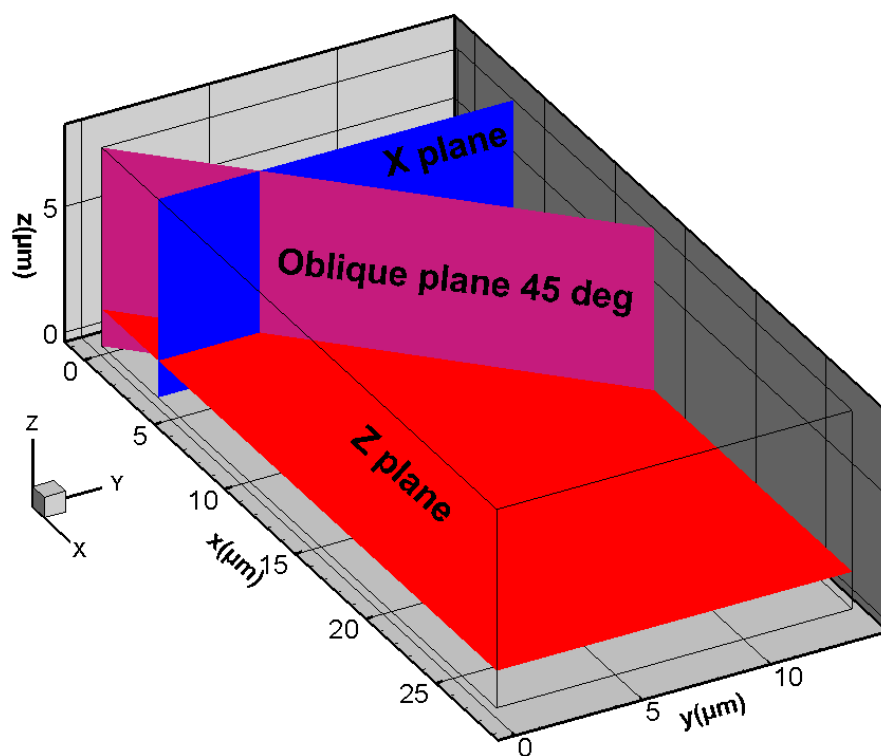
Figure 3.55: Locations of the three cross-sectional planes (X plane at X = 4.0 µm, Z plane at Z = 1.5 µm, and oblique plane) within the 3D PF domain used in the 2D micrograph comparisons.
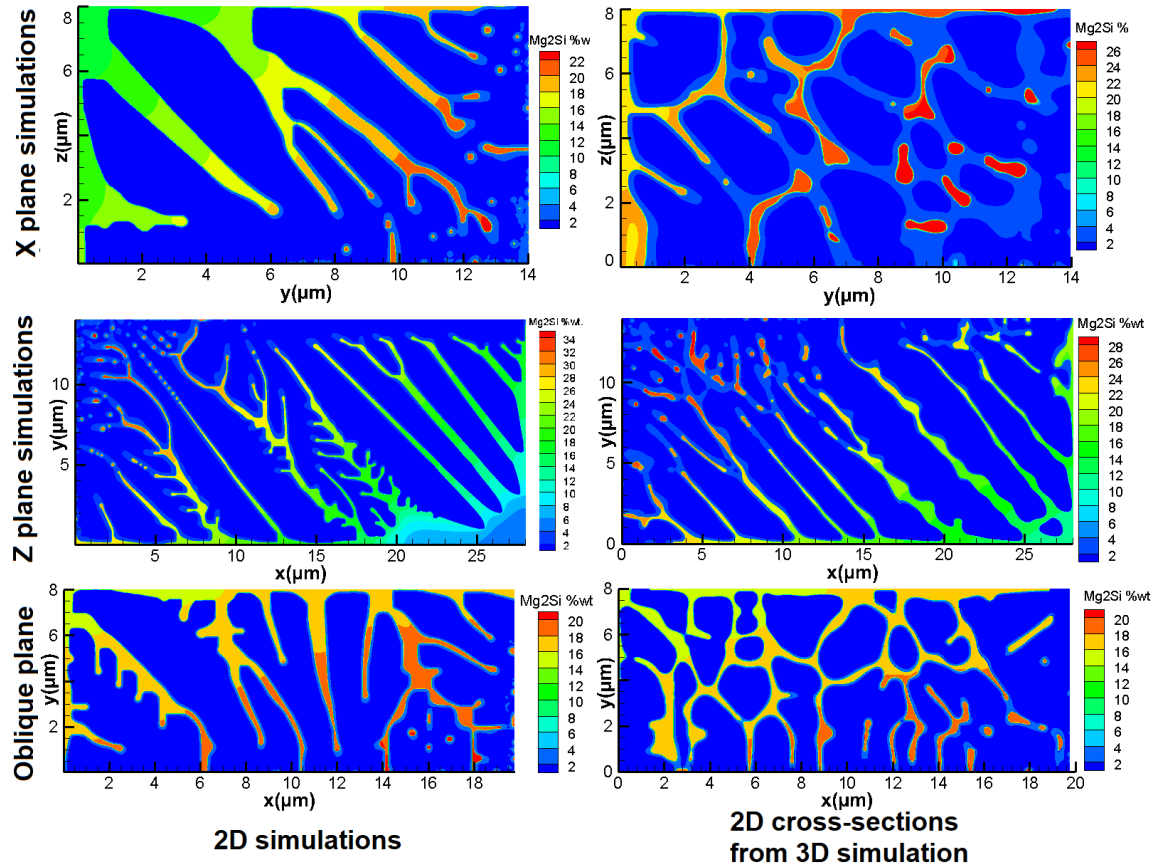
Figure 3.56: Comparison between 2D PF simulations and 2D cross-sections of 3D PF simjlations performed on the 3 planes illustrated in Figure 3.55.

There are obvious similarities and differences between the 2D cross-sections of the 3D simulation and the 2D simulations. For example, the directional growth of the dendrites within the planes is the same and the sizes of the dendrites are similar, as are the locations of the trapped high-concentration solute pools. However, the 2D cross-sections represent individual planes of a 3D field of dendrites and the growth and micro-segregation mechanisms are quite different between 2D and 3D, resulting in different concentration values across the 2D surface. For the 3D cross-sections, the solute can diffuse in the liquid throughout the entire 3D domain as illustrated in Figure 3.53. As the solute diffuses toward the hotter side of the 3D domain, the solid/liquid interface will continue to advance and reject additional solute into the liquid, thereby increasing

the solute concentration throughout the given cross-section of Figure 3.56. However, the solute in the 2D simulations of Figure 3.56 can only diffuse within the given plane. Solute becomes trapped more easily and the solid/liquid interface is inhibited from advancing as much as the interface of the 3D simulation. This leads to less solidification and less overall solute rejection into the liquid. Thus, the concentration fields are drastically different between the 3D cross-section results and the 2D simulation results. While the 28 µm × 14 µm × 8 µm 3D PF simulation required approximately 60 days of computation on 20 processors, the small 2D simulations (on 20 processors) required 20 minutes for the X plane 14 µm × 8 µm domain, 75 minutes for the Z plane 28 µm × 14 µm domain, and 30 minutes for the oblique 20 µm × 8 µm domain.

Both the X plane results, and the Z plane results in Figure 3.56 occur on planes within the 3D domain that have somewhat strong temperature gradients. As mentioned in Section 3.3.1, the strongest gradient within the 3D domain is shown in Figure 3.51 from point D to E, and the weakest temperature gradient is, of course, perpendicular to the strongest temperature gradient, or parallel to the isotherms. Within a 3D domain, simulated 3D dendrites will grow parallel to the temperature gradient. Within a 2D plane of the 3D domain, simulated 2D dendrites can only grow within that plane. If the plane is relatively parallel to the temperature gradient, a 2D PF simulation will reasonably approximate the 2D cross section of a 3D PF simulation, as shown in the X plane and Z plane images of Figure 3.56. However, on a plane that is closely perpendicular to the temperature gradient, a 2D PF simulation will give a poor approximation of the 2D cross-section of a 3D PF simulation, as shown in the bottom images of Figure 3.56.

When the temperature gradient is relatively perpendicular to a given 2D plane, the 3D dendrites growing in the region will grow perpendicular to that plane and the 2D cross-section of the

dendrites will appear as circles and blobs, as can be seen the lower right image of Figure 3.56, rather than branched dendrites. However, a 2D PF simulation performed in this plane can only simulate dendrite growth within the plane resulting in branched dendrites that follow the relatively weak temperature gradient, as shown in the lower left image of Figure 3.56. This illustrates a strong difference between 2D simulation results and 2D cross-sections of 3D simulation results. Although the 2D and 2D cross-section results of the X plane and Z plane images in Figure 3.56 are arguably similar, the 2D and 2D cross-section results of the oblique plane images (lower left and lower right, respectively, in Figure 3.56) are not similar.

The actual 2D micrographs of the X plane and the comparison with the X plane PF results are shown in Figure 3.57 while the Z plane micrograph and simulation results are shown in Figure 3.58. It can be seen in Figure 3.57 and Figure 3.58 that the dendrite spacing and orientation agree well in both the X plane and Z plane cross-sectional views. In comparing the 2D cross-sections of the 3D simulation results with the 2D simulation results, it is clear that the 2D cross-sections of the 3D simulation better represent the actual microstructure over the 2D simulation results. The 2D simulation results show continuous dendrites within the simulation plane, while the 2D cross-section images of the 3D simulation results show the cross-sections of 3D dendrite arms which have grown parallel to the temperature gradient of the 3D domain.
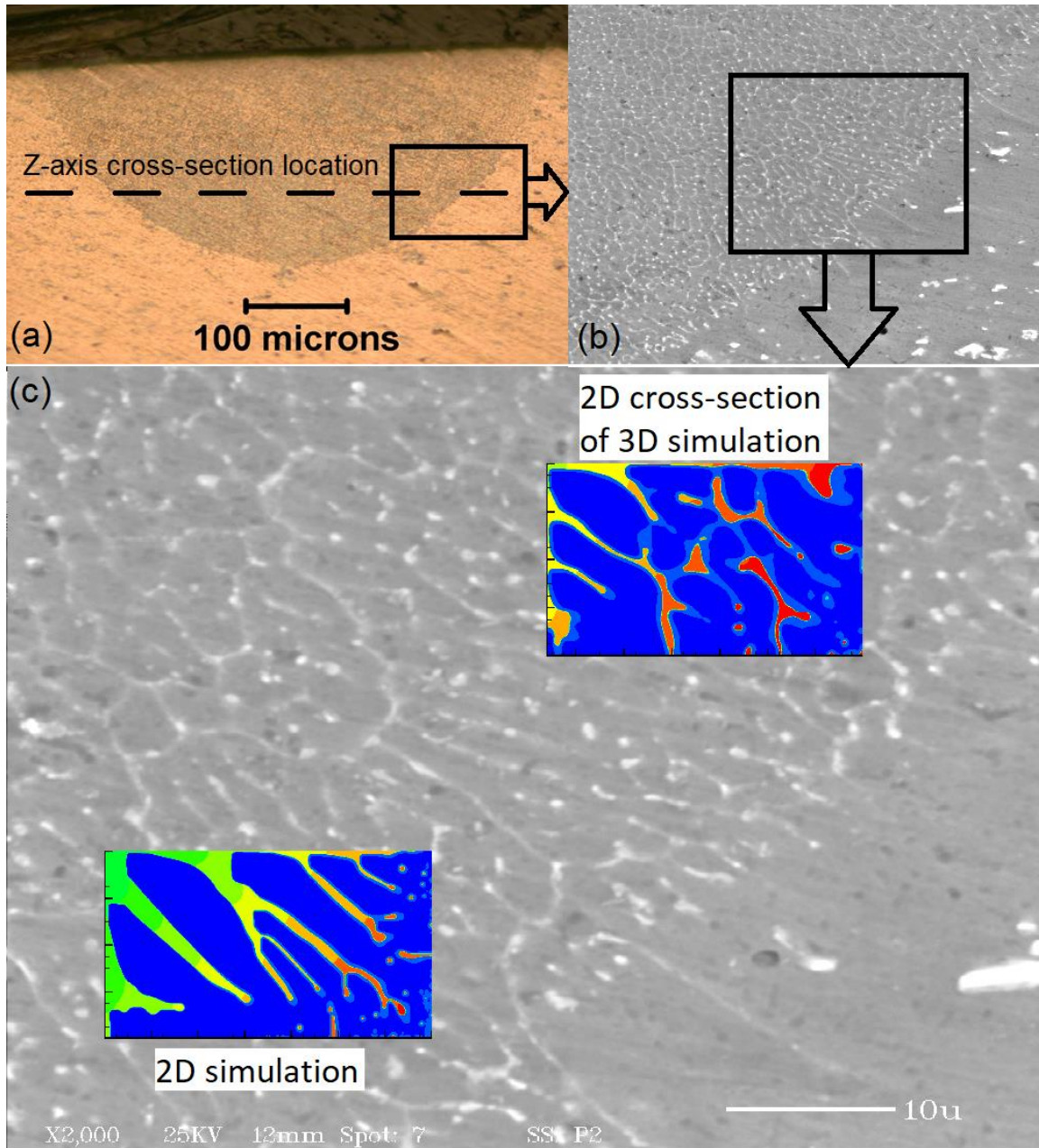
Figure 3.57: X plane 2D cross-section (x-axis) from experimental weld. Dotted line in (a) shows location of X-Y plane cross-section of Figure 3.58. Box in (a) shows detailed region of SEM image (b). Box in (b) shows detailed region of SEM image (c). PF predicted images in (c) show comparison of dendrite arm sizing and orientation with the at-scale 2D cross-section of the 3D PF simulation and the 2D PF simulation (Figure 3.56).
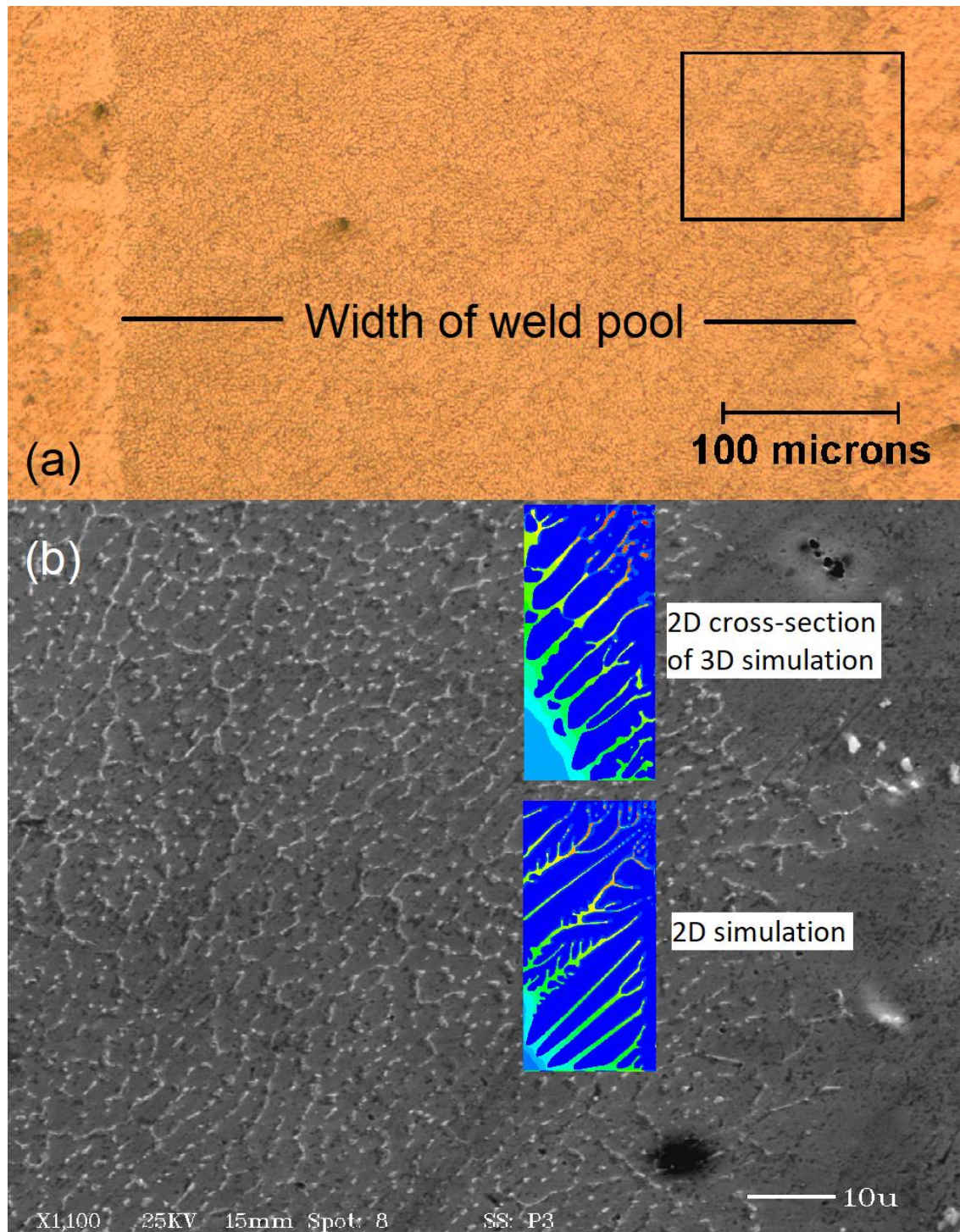
Figure 3.58: Z plane 2D cross-section (z-axis) from experimental weld. The cross-sectional plane location is illustrated by the dotted line in Figure 3.57. Box in (a) shows detailed region of SEM image (b). PF predicted images in (b) show comparison of dendrite arm sizing and orientation with the at-scale 2D cross-section of the 3D simulation and the 2D simulation (Figure 3.56).
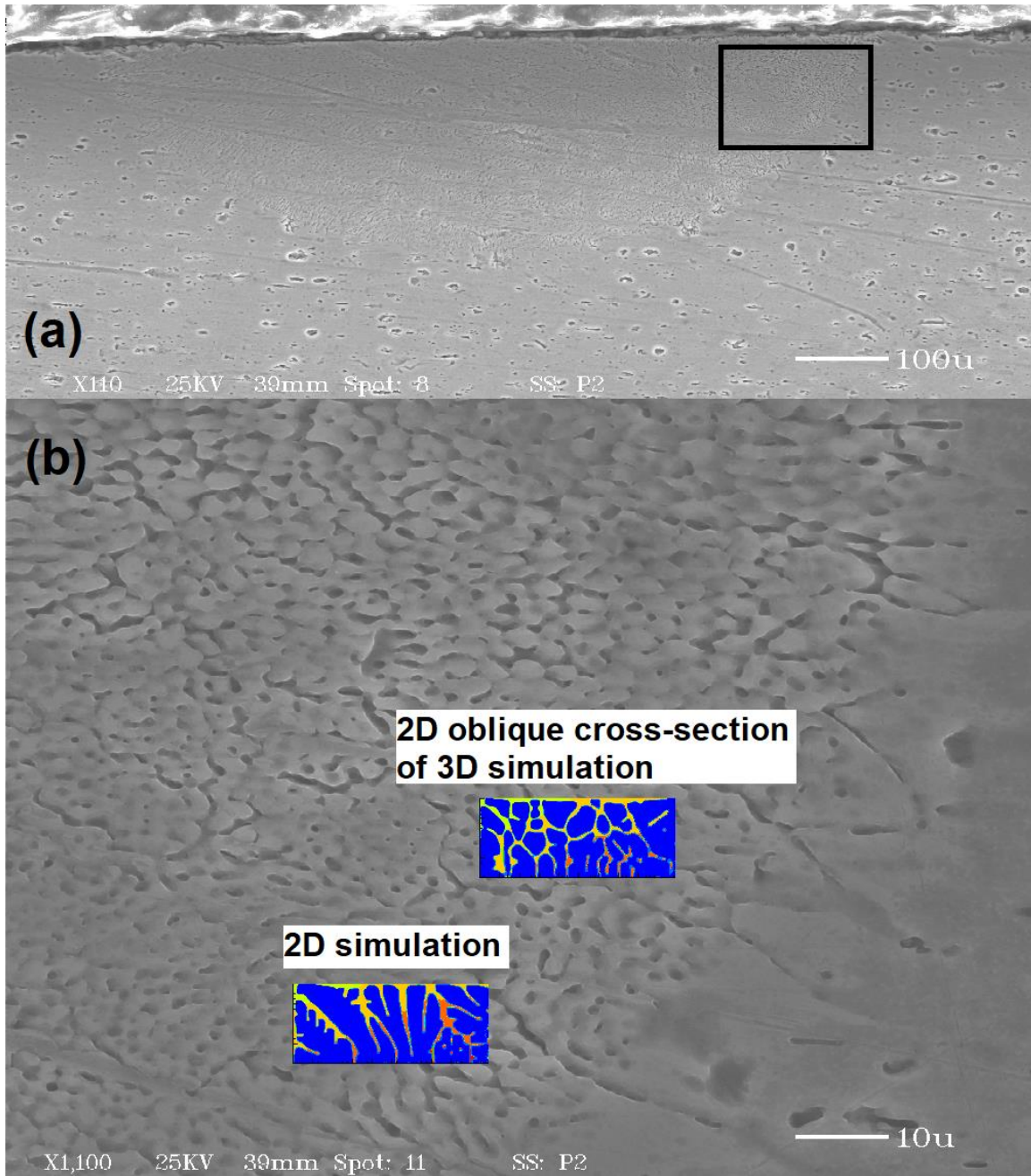
Figure 3.59: Oblique plane 2D cross-section from experimental weld. Box in (a) shows detailed region of SEM image (b). PF predicted images in (b) show comparison of dendrite arm sizing and orientation with the at-scale 2D cross-section of the 3D simulation and the 2D simulation (Figure 3.56).

A more pronounced comparison between 2D and 3D simulation vs. micrograph is shown in Figure 3.59 where the analysis plane (illustrated as "Oblique plane 45 deg" in Figure 3.55) is closely perpendicular to the temperature gradient. The two oblique plane analysis results in Figure 3.56 are both compared with a micrograph of the oblique plane. It can be seen from Figure 3.59 that the 2D cross-section of the 3D simulation is a much more accurate prediction of the actual microstructure than the 2D simulation. Because dendrite growth is a 3D phenomenon, 3D PF analysis will always be more accurate than 2D PF analysis. However, the differences between 2D and 3D analysis are even more pronounced when the analysis plane is not aligned with the temperature gradient and dendrite growth direction.

Despite the advantages of 3D PF analysis, this higher accuracy comes at a significantly higher computational cost: 60 days for a 28 µm × 14 µm × 8 µm 3D simulation to solidify for 0.0051 seconds vs. about an hour and a half for three separate 2D simulations of 28 µm × 14 µm, 14 µm × 8 µm, and 19.6 µm × 8 µm. The choice between a computationally expensive 3D PF simulation and a less accurate 2D PF simulation depends on the desired level of accuracy and the layout of the thermal field. A 2D PF simulation will quickly predict overall morphology, dendrite growth direction within a given plane, approximate SDAS values, and solute concentration extremes. However, a 3D simulation is required to predict intricate morphology, precise dendrite growth direction within a transient 3D field, exact SDAS values, and detailed concentration profiles, especially when the temperature field is complex and non-ideal. At a significant computational cost, the 3D PF model is a far superior tool for predicting dendrite growth during real-world manufacturing processes.

4. SUMMARY, CONCLUSIONS, AND FUTURE WORK

4.1 Summary

In this thesis, the state-of-the-art has been established in Section 1.2. Although much work has been done with numerical models for predicting microstructure during laser-based manufacturing processes, there is a lack of models that address large 2D and 3D domains on the same scale as a molten pool. Additionally, considering the strong impact of residual stress on material properties, few studies have been presented predicting residual stresses based on thermal cycles and phase transformations.

In Section 2, the development and validation of numerical models for addressing these issues is presented including solid-state phase transformation in steels that considers heating, cooling, tempering, melting, and solidification; residual stress that considers thermal strains and phase transformation-induced strains; and microstructure development models for predicting dendrite growth in multi-component alloy solidification for large 2D domains and small 3D domains.

The numerical models presented in Section 2 are applied to laser-based manufacturing processes and some industrial examples in Section 3.

4.2 Conclusions

4.2.1 Laser Hardening

In Section 3.1, a predictive model for calculating residual stresses in a laser hardened steel workpiece has been presented and experimentally verified. A finite volume 3D transient solid-state phase transformation model, which calculates the temperature history and phase change history, was used to simulate the heat transfer and corresponding phase transformation in a

50x50x18 mm AISI 4140 steel block, while taking into account appropriate boundary conditions, latent heat of solid-state phase transformation, carbon diffusion in austenite homogenization, and cooling effects. The final hardness field was then calculated using the resulting microstructure. The hardness and case depth of the experimental workpiece agreed with the model's results. The thermal history and phase fraction history were then used in a finite element residual stress model that takes into account thermal strains and phase transformation effects of volumetric dilatation and transformation-induced plasticity. The model predicted high compressive stresses throughout the hardened martensitic region, surrounded by a region of tensile stresses, and finally a stress-free region. The compressive stress in the hardened region is mainly due to volumetric dilatation of the local material transforming into martensite. The magnitude of the residual stress in the hardened region of the experimental workpiece was measured using X-ray diffraction, which agreed with the results predicted by the model.

4.2.2   Laser Deposition

In Section 3.2, optimal operating parameters were experimentally determined for multi-track and multi-layer laser direct deposition (LDD) of H13 tool steel. These operating parameters were then used for the remanufacture and repair of two industrial tooling components. Microstructure analysis of the deposited material revealed an average grain size of 28 µm and a secondary dendrite arm spacing of 1.86 µm. Hardness measurements returned a value of up to 690 Vickers. Ultimate tensile strength (UTS) of the deposited material was measured at an average 2072 MPa, between 15% and 30% stronger than published UTS values of commercial grade H13 steel.

The CA-PF model was used to simulate the dendrite growth of the multi-track and multi-layer LDD process. Using the CALPHAD method, the material was modeled as a ternary alloy consisting of Fe, 5.0 wt.% Cr and 1.5 wt.% Mo. The simulated deposition of multiple tracks and

layers showed that the dendrite growth direction and scale across an entire weld pool (430 µm × 300 µm) matched very well with experimental results. In addition to microstructure simulation, the model also predicted that during the deposition of a single track, the resultant phase is nearly all martensite due to the rapid cooling typical of laser-based additive processes. However, after multiple neighboring deposition tracks caused high- and low-level heating cycles to affect the target track, the previously formed martensite was considerably tempered to softer phases, resulting in a reduction down to 80% martensite phase fraction and a reduction in hardness of 150 HV.

A finite element model was built and utilized to predict the phase transformation kinetics and residual stresses of the multi-track multi-layer LDD. Predicted variation of hardness across deposition tracks matched well with measured values. For a two-layer simulation, predicted strong compressive stresses of -400 MPa at a depth of 0.5 mm and strong tensile stress of +400 MPa at a depth of 1.0 mm were confirmed by measurement using XRD. Small variations in compressive stresses along the top surface across of the deposited tracks were also predicted.

4.2.3   Laser Welding

In Section 3.3, the 2D and 3D PF models have been used to illustrate the failings of 2D PF simulations when used to predict dendrite growth and microstructure development in isothermal conditions and during laser welding processes. From the results of isothermal solidification of an Al-4wt.%Cu alloy, it is clear that 3D simulations (which account for 3D diffusion) result in different morphology, faster dendrite growth, and a smaller secondary dendrite arm spacing than 2D simulation results.

By linking the PF models with a comprehensive, multi-physics laser welding model, the models were also used to simulate dendrite growth and microstructure development during laser welding of Al 6061 alloy. By comparing the 2D results and the 2D cross-sections of the 3D results with micrographs from an experimental work piece, it was shown that the 3D cross-section results match much closer to the actual experimental micrograph than the 2D simulation results and they are a better prediction of dendrite growth and solidification microstructure than the 2D simulation results, especially when the temperature gradient is closely perpendicular to the analysis plane. However, the computational cost of the 3D results (60 days of computation on 20 processors for a 28 µm×14µm×8 µm domain solidifying for 0.0051 seconds) were significantly more expensive than the 2D simulation cost on the same 20 processors (75 minutes for a 28 µm ×14 µm domain, 20 minutes for a 14 µm×8 µm domain, and 30 minutes for a 19.6 µm×8 µm domain for the same solidification time).

Despite the significant computational advantage of 2D PF simulations over 3D simulations, it is important to understand the fundamental differences in diffusion, solute concentration field, growth velocity, primary and secondary dendrite arm spacing, and overall morphology between 2D and 3D simulations and the effects of 2D analysis plane and temperature gradient alignment.

4.3 Future Work

To continue the work of predictive dendrite growth, the next step should be to expand the CAPF model into 3D. Once the 3D CA framework is finished, several possible PF formulations can be tested, and the resulting 3D dendrites compared with a 3D dendrite from the 3D PF model. The 2D CAPF model, as discussed in Section 2.3.2, uses a 1D PF model formulated in polar coordinates to provide data to the 2D CA model. The reason a polar coordinate formulation is

used is because any point along the solid/liquid interface of a 2D dendrite can be locally approximated as 1D growth of a curved interface, no matter whether the curvature is negative or positive.

For a 3D CA model, a 1D PF model in polar coordinates may not be sufficient. As shown in Figure 4.1, at least 5 types of 3D surface curvature can be classified on the surface of a 3D dendrite: tip, ridge, valley, saddle, and bowl. Each type of surface geometry has distinct characteristics and complex surface curvature that cannot be represented by a single scalar.
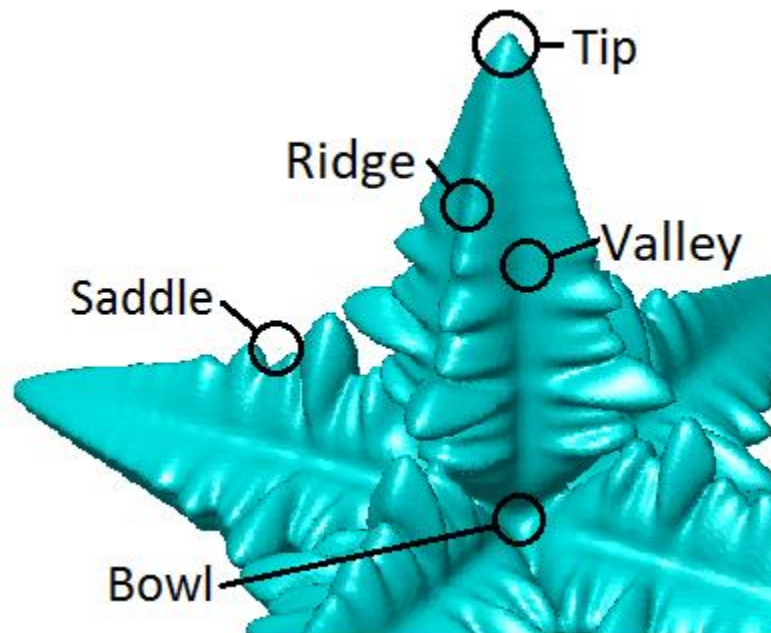
Figure 4.1: 3D dendrite showing complex surface with different types of local curvature.

- Tip: Positive curvature in all directions

- Ridge: Negligible curvature along the edge direction, positive curvature orthogonal to the edge

- Valley: Negligible curvature along the trough direction, negative curvature orthogonal to the trough

- Saddle: Positive curvature in one plane, and negative curvature in an intersecting plane

- Bowl: Negative curvature in all directions

In order to provide accurate growth kinetics to a 3D CA framework for all of these cases, the PF model must be able to describe the 3D surface curvature at any point along the interface. A 3D PF model can provide this information for each of these geometries, but the computational cost would be very high. However, a careful selection of 1D PF formulations in various coordinate systems may be able to accurately provide the necessary growth kinetics with a reasonable computational cost.

For the case of growth at a tip or bowl where all tangential directions have a similar value for curvature (either positive or negative), a 1D spherical coordinate system formulation can be used to solve the PF equations. For the edge and trough cases, where one tangential direction is nearly flat, a 1D polar coordinate system could be used since the local geometry can be approximated as a cylinder. However, for the saddle case and anywhere else where the curvature cannot be described with a single scalar value, the 1D approximation is not so simple.

For every point on a 3D dendrite surface, two planes can be used to describe the local curvature. These planes must contain the principal curvatures (the two greatest absolute value curvatures) of the surface locally. The planes need not be orthogonal, but in many instances, they will be approximately orthogonal. A summary of the types of surfaces, the corresponding curvatures of their principal planes, and some possible approaches for solving the PF equations is shown in

Table 4.1. The graph in Figure 4.2 shows graphically the comparison of the two principal

curvatures.

Table 4.1: Types of 3D surfaces and possible PF formulations.

Surface type	Plane 1 curvature	Plane 2 curvature		PF formulation
Tip	+	+	similar values	1D spherical
Bowl	-	-	similar values	1D spherical
Ridge	+	≈ 0		1D cylindrical
Valley	-	≈ 0		1D cylindrical
Saddle	+	-		Average of curvatures of
Other			dissimilar values	principal planes
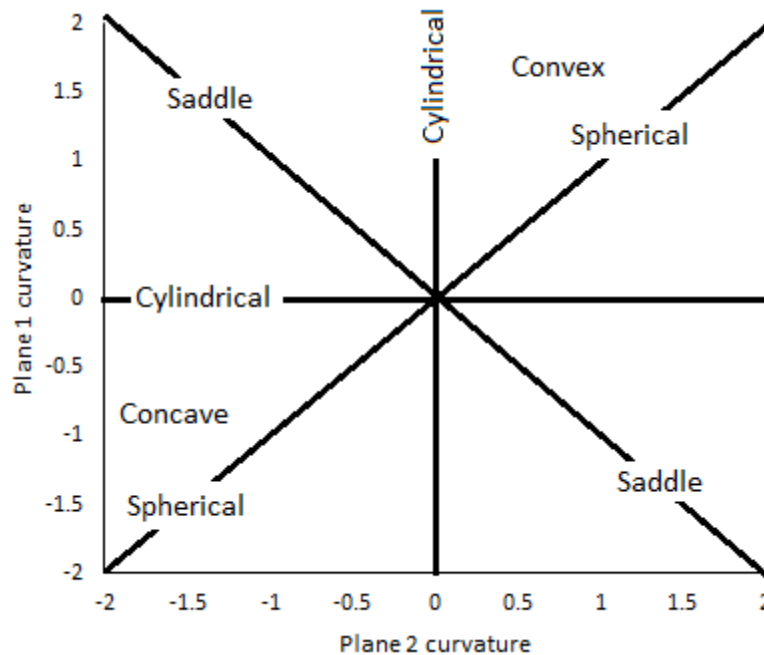
Figure 4.2: Principal curvatures and the type of local surface.

Perhaps the simplest approach for approximating the PF domain is by simply finding the

principal curvatures and using their sum as the curvature in a 1D spherical system. For two

positive or negative principal curvatures, the result would be a strong positive or negative

curvature approximating a tip or bowl, respectively. If one curvature is approximately zero, the result would approximate a ridge or valley. For a saddle point, both curvatures would be approximately equal and opposite in value and the sum would thereby approximate a plane rather than a saddle.

REFERENCES

Adams, S.B., Butler, O.R., 1999. Manufacturing the future: A history of Western Electric. Cambridge University Press.

Alimardani, M., Toyserkani, E., Huissoon, J.P., 2007. A 3D dynamic numerical approach for temperature and thermal stress distributions in multilayer laser solid freeform fabrication process. Opt. Lasers Eng. 45, 1115–1130.

Ao, X., Xia, H., Liu, J., He, Q., 2020. Simulations of microstructure coupling with moving molten pool by selective laser melting using a cellular automaton. Mater. Des. 185, 108230.

Ashby, M.F., Easterling, K.E., 1984. The transformation hardening of steel surfaces by laser beams: I. Hypo-eutectoid steels. Acta Metall. 32, 1935–1948.

Bailey, N.S., Hong, K.-M., Shin, Y.C., 2020. Comparative assessment of dendrite growth and microstructure predictions during laser welding of Al 6061 via 2D and 3D phase field models. Comput. Mater. Sci. 172, 109291.

Bailey, N.S., Tan, W., Shin, Y.C., 2009. Predictive modeling and experimental results for residual stresses in laser hardening of AISI 4140 steel by a high power diode laser. Surf. Coatings Technol. 203, 2003–2012.

Beltran-Sanchez, L., Stefanescu, D.M., 2003. Growth of solutal dendrites: a cellular automaton model and its quantitative capabilities. Metall. Mater. Trans. A 34, 367–382.

Benedyk, J.C., 2008. High Performance Alloys Database, H13.

Berghoff, M., Nestler, B., 2015. Phase field crystal modeling of ternary solidification microstructures. Comput. Condens. Matter 4, 46–58.

Boettinger, W.J., Warren, J.A., Beckermann, C., Karma, A., 2002. Phase-field simulation of solidification. Mater. Res. 32, 163.

Böttger, B., Eiken, J., Steinbach, I., 2006. Phase field simulation of equiaxed solidification in technical alloys. Acta Mater. 54, 2697–2704.

Brückner, F., Lepski, D., Beyer, E., 2007. Modeling the influence of process parameters and additional heat sources on residual stresses in laser cladding. J. Therm. spray Technol. 16, 355–373.

Caginalp, G., 1989. Stefan and Hele-Shaw type models as asymptotic limits of the phase-field equations. Phys. Rev. A 39, 5887.

Caginalp, G., Xie, W., 1993. Phase-field and sharp-interface alloy models. Phys. Rev. E 48, 1897.

Cerny, I., Fürbacher, I., Linhart, V., 1998. Influence of laser hardening and resulting microstructure on fatigue properties of carbon steels. J. Mater. Eng. Perform. 7, 361–366.

Cha, P.-R., Yeon, D.-H., Yoon, J.-K., 2001. A phase field model for isothermal solidification of multicomponent alloys. Acta Mater. 49, 3295–3307.

Cha, P.-R., Yeon, D.-H., Yoon, J.-K., 2005. Phase-field model for multicomponent alloy solidification. J. Cryst. Growth 274, 281–293.

Chen, C.C., Tsai, Y.L., Lan, C.W., 2009. Adaptive phase field simulation of dendritic crystal growth in a forced flow: 2D vs 3D morphologies. Int. J. Heat Mass Transf. 52, 1158–1166.

Chen, L.-Q., 2002. Phase-field models for microstructure evolution. Annu. Rev. Mater. Res. 32, 113–140.

Chen, R., Xu, Q., Liu, B., 2015. Cellular automaton simulation of three-dimensional dendrite growth in Al-7Si-Mg ternary aluminum alloys. Comput. Mater. Sci. 105, 90–100.

Cho, J.-H., Na, S.-J., 2006. Implementation of real-time multiple reflection and Fresnel absorption of laser beam in keyhole. J. Phys. D. Appl. Phys. 39, 5372.

Costa, L., Vilar, R., Reti, T., Deus, A.M., 2005. Rapid tooling by laser powder deposition: Process simulation using finite element analysis. Acta Mater. 53, 3987–3999.

Das, S., Upadhya, G., Chandra, U., 1992. Prediction of Macro- and Micro-Residual Stress in Quenching Using Phase Transformation Kinetics. Quenching Distortion Control 229–234.

Daudin, R., Terzi, S., Lhuissier, P., Tamayo, J., Scheel, M., Babu, N.H., Eskin, D.G., Salvo, L., 2017. Particle-induced morphological modification of Al alloy equiaxed dendrites revealed by sub-second in situ microtomography. Acta Mater. 125, 303–310.

Davis, M., Kapadia, P., Dowden, J., Steen, W.M., Courtney, C.H.G., 1986. Heat hardening of metal surfaces with a scanning laser beam. J. Phys. D. Appl. Phys. 19, 1981.

Denis, S., Archambault, P., Aubry, C., Mey, A., Louin, J.C., Simon, A., 1999. Modelling of phase transformation kinetics in steels and coupling with heat treatment residual stress predictions. Le J. Phys. IV 9, Pr9--323.

Dong, H.B., Lee, P.D., 2005. Simulation of the columnar-to-equiaxed transition in directionally solidified Al--Cu alloys. Acta Mater. 53, 659–668.

Eiken, J., 2010. Phase-field simulation of microstructure formation in technical magnesium alloys. Int. J. Mater. Res. 101, 503–509.

Fabbro, R., Chouf, K., 2000. Keyhole modeling during laser welding. J. Appl. Phys. 87, 4075–4083.

Farahmand, P., Kovacevic, R., 2014. An experimental--numerical investigation of heat distribution and stress field in single-and multi-track laser cladding by a high-power direct diode laser. Opt. Laser Technol. 63, 154–168.

Feng, W.M., Yu, P., Hu, S.Y., Liu, Z.-K., Du, Q., Chen, L.-Q., 2006. Spectral implementation of an adaptive moving mesh method for phase-field equations. J. Comput. Phys. 220, 498–510.

Flemings, M.C., 1974. Solidification processing. Metall. Trans. 5, 2121–2134.

George, W.L., Warren, J.A., 2002. A parallel 3D dendritic growth simulator using the phase-field method. J. Comput. Phys. 177, 264–283.

Gong, T.Z., Chen, Y., Li, D.Z., Cao, Y.F., Fu, P.X., 2019. Quantitative comparison of dendritic growth under forced flow between 2D and 3D phase-field simulation. Int. J. Heat Mass Transf. 135, 262–273.

Grafe, U., Böttger, B., Tiaden, J., Fries, S.G., 2000. Coupling of multicomponent thermodynamic databases to a phase field model: application to solidification and solid state transformations of superalloys. Scr. Mater. 42, 1179–1186.

Gránásy, L., Pusztai, T., Warren, J.A., 2004. Modelling polycrystalline solidification using phase field theory. J. Phys. Condens. Matter 16, R1205.

Grigor'yants, A.G., Safonov, A.N., Maiorov, V.S., Baskov, A.F., Ivashov, G.P., 1987. istribution of residual stresses on the surface of steels hardened with a continuous CO2-laser. Met. Sci. Heat Treat. 29, 691–694.

Gu, C., Ridgeway, C.D., Luo, A.A., 2019. Examination of dendritic growth during solidification of ternary alloys via a novel quantitative 3D cellular automaton model. Metall. Mater. Trans. B 50, 123–135.

Guo, Z., Zhou, J., Yin, Y., Zhang, D., Ji, X., Shen, X., 2017. Multi-scale coupling simulation in directional solidification of superalloy based on cellular automaton-finite difference method. China Foundry 14, 398–404.

He, X., Fuerschbach, P.W., DebRoy, T., 2003. Heat transfer and fluid flow during laser spot welding of 304 stainless steel. J. Phys. D. Appl. Phys. 36, 1388.

He, X., Yu, G., Mazumder, J., 2009. Temperature and composition profile during double-track laser cladding of H13 tool steel. J. Phys. D. Appl. Phys. 43, 015502.

Inoue, T., 2002. Metallo-Thermo-Mechanics-Application to Quenching. Handb. Residual Stress Deform. Steel 296–311.

Jacot, A., Rappaz, M., 1999. A combined model for the description of austenitization, homogenization and grain growth in hypoeutectoid Fe--C steels during heating. Acta Mater. 47, 1645–1651.

Jin, L., 2001. Simulation of Quenching and Temperaing of Steels. Purdue University.

Jung, M., Lee, S.-J., Lee, Y.-K., 2009. Microstructural and dilatational changes during tempering and tempering kinetics in martensitic medium-carbon steel. Metall. Mater. Trans. A 40, 551–559.

Kamara, a. M., Marimuthu, S., Li, L., 2011. A Numerical Investigation into Residual Stress Characteristics in Laser Deposited Multiple Layer Waspaloy Parts. J. Manuf. Sci. Eng. 133, 031013.

Kao, A., Krastins, I., Alexandrakis, M., Shevchenko, N., Eckert, S., Pericleous, K., 2019. A parallel cellular automata Lattice Boltzmann Method for convection-driven solidification. JOM 71, 48–58.

Karma, A., 2001. Phase-field formulation for quantitative modeling of alloy solidification. Phys. Rev. Lett. 87, 115701.

Katinas, C., Shang, W., Shin, Y.C., Chen, J., 2018. Modeling Particle Spray and Capture Efficiency for Direct Laser Deposition Using a Four Nozzle Powder Injection System. J. Manuf. Sci. Eng. 140, 41014.

Kaufman, L., Bernstein, H., 1970. Computer calculation of phase diagrams. With special reference to refractory metals.

Kessler, D.A., Koplik, J., Levine, H., 1988. Pattern selection in fingered growth phenomena. Adv. Phys. 37, 255–339.

Ki, H., Mohanty, P.S., Mazumder, J., 2001. Modelling of high-density laser-material interaction using fast level set method. J. Phys. D. Appl. Phys. 34, 364.

Kim, S.G., 2007. A phase-field model with antitrapping current for multicomponent alloys with arbitrary thermodynamic properties. Acta Mater. 55, 4391–4399.

Kim, S.G., Kim, W.T., Suzuki, T., 1999. Phase-field model for binary alloys. Phys. Rev. e 60, 7186.

Kobayashi, H., Ode, M., Kim, S.G., Kim, W.T., Suzuki, T., 2003. Phase-field model for solidification of ternary alloys coupled with thermodynamic database. Scr. Mater. 48, 689–694.

Koepf, J.A., Gotterbarm, M.R., Markl, M., Körner, C., 2018. 3D multi-layer grain structure simulation of powder bed fusion additive manufacturing. Acta Mater. 152, 119–126.

Komanduri, R., Hou, Z.B., 2001. Thermal analysis of the laser surface transformation hardening process. Int. J. Heat Mass Transf. 44, 2845–2862.

Komanduri, R., Hou, Z.B., 2004. Thermal analysis of laser surface transformation hardening: optimization of process parameters. Int. J. Mach. Tools Manuf. 44, 991–1008.

Kou, S., 1987. Welding metallurgy. New York.

Kou, S., 2003. Welding metallurgy. New Jersey, USA 431–446.

Kou, S., Sun, D.K., Le, Y.P., 1983. A fundamental study of laser transformation hardening. Metall. Trans. A 14, 643–653.

Krane, M.J.M., Johnson, D.R., Raghavan, S., 2009. The development of a cellular automaton-finite volume model for dendritic growth. Appl. Math. Model. 33, 2234–2247.

Kundin, J., Ramazani, A., Prahl, U., Haase, C., 2019. Microstructure Evolution of Binary and Multicomponent Manganese Steels During Selective Laser Melting: Phase-Field Modeling and Experimental Validation. Metall. Mater. Trans. A 50, 2022–2040.

Kundin, J., Rezende, J.L.L., Emmerich, H., 2014. Phase-field modeling of the coarsening in multi-component systems. Metall. Mater. Trans. A 45, 1068–1084.

Kurz, W., Fisher, D., 1998. Fundamentals of solidification, fourth ed. Enfield Publishing & Distribution Company, Enfield, NH.

Kurz, W., Fisher, D.J., 1986. Fundamentals of solidification. Trans Tech Publ. Ltd, Trans Tech House, 4711, Aedermannsdorf, Switzerland, 1986. 244.

Kurz, W., Giovanola, B., Trivedi, R., 1986. Theory of microstructural development during rapid solidification. Acta Metall. 34, 823–830.

Labudovic, M., Hu, D., Kovacevic, R., 2003. A three dimensional model for direct laser metal powder deposition and rapid prototyping. J. Mater. Sci. 38, 35–49.

Lacarac, Smith, McMahon, Tierney, 2002. Non-Dimensional Approach for Estimation of Residual Stresses During Cooling in Steel, in: Proceedings of the 1st International Surface Engineering Congress. Columbus, OH, p. 578.

Lakhkar, R.S., Shin, Y.C., Krane, M.J.M., 2008. Predictive modeling of multi-track laser hardening of AISI 4140 steel. Mater. Sci. Eng. A 480, 209–217.

Leung, M., 2001. Phase-change heat transfer in laser transformation hardening by moving Gaussian rectangular heat source. J. Phys. D. Appl. Phys. 34, 3434.

Leung, M.K.H., Man, H.C., Yu, J.K., 2007. Theoretical and experimental studies on laser transformation hardening of steel by customized beam. Int. J. Heat Mass Transf. 50, 4600–4606.

Li, Q., Wang, Y., Zhang, H.W., Xie, S.S., Huang, G.J., 2013. Numerical simulation of microstructure and solutal microsegregation formation of ternary alloys during solidification process. Ironmak. Steelmak.

Lin, Y., McHugh, K.M., Zhou, Y., Lavernia, E.J., 2007. Modeling the spray forming of H13 steel tooling. Metall. Mater. Trans. A 38, 1632–1637.

Lipton, J., Glicksman, M.E., Kurz, W., 1984. Dendritic growth into undercooled alloy metals. Mater. Sci. Eng. 65, 57–63.

Lipton, J., Kurz, W., Trivedi, R., 1987. Rapid dendrite growth in undercooled alloys. Acta Metall. 35, 957–964.

Long, W.-Y., Chun, X., Bo-Wen, X., Li-Gao, F., 2008. Phase-field simulation of dendritic growth in a binary alloy with thermodynamics data. Chinese Phys. B 17, 1078.

Lusquinos, F., Conde, J.C., Bonss, S., Riveiro, A., Quintero, F., Comesana, R., Pou, J., 2007. Theoretical and experimental analysis of high power diode laser (HPDL) hardening of AISI 1045 steel. Appl. Surf. Sci. 254, 948–954.

Maryland Metrics [WWW Document], 2016.

Michelic, S.C., Thuswaldner, J.M., Bernhard, C., 2010. Polydimensional modelling of dendritic growth and microsegregation in multicomponent alloys. Acta Mater. 58, 2738–2751.

Mioković, T., Schulze, V., Vöhringer, O., Löhe, D., 2007. Influence of cyclic temperature changes on the microstructure of AISI 4140 after laser surface hardening. Acta Mater. 55, 589–599.

Natsume, Y., Ohsasa, K., 2006. Prediction of casting structure in aluminum-base multi-component alloys using heterogeneous nucleation parameter. ISIJ Int. 46, 896–902.

Nie, P., Ojo, O.A., Li, Z., 2014. Numerical modeling of microstructure evolution during laser additive manufacturing of a nickel-based superalloy. Acta Mater. 77, 85–95.

Oddy, A.S., Goldak, J.A., McDill, J.M.J., 1989. Transformation effects in the 3D finite element analysis of welds, in: Proceedings of the Second International Conference on Trends in Welding Research. pp. 15–19.

Ode, M., Kim, S.G., Suzuki, T., 2001a. Mathematical Modeling of Iron and Steel Making Processes. Recent Advances in the Phase-field Model for Solidification. ISIJ Int. 41, 1076–1082.

Ode, M., Kim, S.G., Suzuki, T., 2001b. Recent advances in the phase-field model for solidification. ISIJ Int. 41, 1076–1082.

Ode, M., Lee, J.S., Kim, S.G., Kim, W.T., Suzuki, T., 2000. Phase-field Model for Solidification of Ternary Alloys. ISIJ Int. 40, 870–876.

Ohmura, E., INOUE, K., Haruta, K., 1989. Computer simulation on structural changes of hypoeutectoid steel in laser transformation hardening process. JSME Int. journal. Ser. 1, Solid Mech. strength Mater. 32, 45–53.

Okhotnikov, O.G., 2012. Fiber lasers. John Wiley & Sons.

Pan, S., Zhu, M., 2010. A three-dimensional sharp interface model for the quantitative simulation of solutal dendritic growth. Acta Mater. 58, 340–352.

Pang, S., Chen, L., Zhou, J., Yin, Y., Chen, T., 2010. A three-dimensional sharp interface model for self-consistent keyhole and weld pool dynamics in deep penetration laser welding. J. Phys. D. Appl. Phys. 44, 25301.

Patwa, R., Shin, Y.C., 2007. Predictive modeling of laser hardening of AISI5150H steels. Int. J. Mach. Tools Manuf. 47, 307–320.

Pavlyk, V., Dilthey, U., 2003. Simulation of weld solidification microstructure and its coupling to the macroscopic heat and fluid flow modelling. Model. Simul. Mater. Sci. Eng. 12, S33.

Peng, R., Ericsson, T., 1998. Residual stress distributions in laser transformation hardened steels. Scand. J. Metall. 27, 223–232.

Provatas, N., Goldenfeld, N., Dantzig, J., 1998. Efficient computation of dendritic microstructures using adaptive mesh refinement. Phys. Rev. Lett. 80, 3308.

Provatas, N., Greenwood, M., Athreya, B., Goldenfeld, N., Dantzig, J., 2005. Multiscale modeling of solidification: phase-field methods to adaptive mesh refinement. Int. J. Mod. Phys. B 19, 4525–4565.

Qin, R.S., Wallach, E.R., Thomson, R.C., 2005. A phase-field model for the solidification of multicomponent and multiphase alloys. J. Cryst. Growth 279, 163–169.

Raghavan, S., 2005. A Numerical Model For Dendritic Growth In Binary Alloys. Purdue University.

Rai, R., Roy, G.G., DebRoy, T., 2007. A computationally efficient model of convective heat transfer and solidification characteristics during keyhole mode laser welding. J. Appl. Phys. 101, 54909.

Santhanakrishnan, S., Kong, F., Kovacevic, R., 2011. An experimentally based thermo-kinetic hardening model for high power direct diode laser cladding. J. Mater. Process. Technol. 211, 1247–1259.

Shin, Y.C., Bailey, N., Katinas, C., Tan, W., 2018. Predictive modeling capabilities from incident powder and laser to mechanical properties for laser directed energy deposition. Comput. Mech. 61, 617–636.

Şimşir, C., Gür, C.H., 2008. A FEM based framework for simulation of thermal treatments: Application to steel quenching. Comput. Mater. Sci. 44, 588–600.

Skvarenina, S., Shin, Y.C., 2006. Predictive modeling and experimental results for laser hardening of AISI 1536 steel with complex geometric features by a high power diode laser. Surf. Coatings Technol. 201, 2256–2269.

Solina, A., de Sanctis, M., Paganini, L., Coppa, P., 1986. Residual stresses induced by localized laser hardening treatments on steels and cast iron. J. Heat Treat. 4, 272–280.

Stefanescu, D.M., 2010. Science and engineering of casting solidification, second ed. Springer.

Suzuki, T., Ode, M., Kim, S.G., Kim, W.T., 2002. Phase-field model of dendritic growth. J. Cryst. Growth 237, 125–131.

Svenungsson, J., Choquet, I., Kaplan, A.F.H., 2015. Laser welding process--a review of keyhole welding modelling. Phys. Procedia 78, 182–191.

Takaki, T., Ohno, M., Shimokawabe, T., Aoki, T., 2014. Two-dimensional phase-field simulations of dendrite competitive growth during the directional solidification of a binary alloy bicrystal. Acta Mater. 81, 272–283.

Tan, Wenda, Bailey, N.S., Shin, Y.C., 2011a. A novel integrated model combining Cellular Automata and Phase Field methods for microstructure evolution during solidification of multi-component and multi-phase alloys. Comput. Mater. Sci. 50, 2573–2585.

Tan, W., Bailey, N.S., Shin, Y.C., 2012. Numerical Modeling of Transport Phenomena and Dendritic Growth in Laser Spot Conduction Welding of 304 Stainless Steel. J. Manuf. Sci. Eng. 134, 041010.

Tan, W., Bailey, N.S., Shin, Y.C., 2013. Investigation of keyhole plume and molten pool based on a three-dimensional dynamic model with sharp interface formulation. J. Phys. D. Appl. Phys. 46. https://doi.org/10.1088/0022-3727/46/5/055501

Tan, Wenda, Bailey, N.S., Shin, Y.C., 2013. Investigation of keyhole plume and molten pool based on a three-dimensional dynamic model with sharp interface formulation. J. Phys. D. Appl. Phys. 46, 55501.

Tan, W., Shin, Y.C., 2015. Multi-scale modeling of solidification and microstructure development in laser keyhole welding process for austenitic stainless steel. Comput. Mater. Sci. 98, 446–458. https://doi.org/10.1016/j.commatsci.2014.10.063

Tan, Wenda, Wen, S., Bailey, N., Shin, Y.C., 2011b. Multiscale Modeling of Transport Phenomena and Dendritic Growth in Laser Cladding Processes. Metall. Mater. Trans. B 42, 1306–1318.

Tan, W., Wen, S., Bailey, N., Shin, Y.C., 2011. Multiscale modeling of transport phenomena and dendritic growth in laser cladding processes. Metall. Mater. Trans. B Process Metall. Mater. Process. Sci. 42. https://doi.org/10.1007/s11663-011-9545-y

Tani, G., Orazi, L., Fortunato, A., 2008. Prediction of hypo eutectoid steel softening due to tempering phenomena in laser surface hardening. CIRP Ann. Technol. 57, 209–212.

Tani, G., Orazi, L., Fortunato, A., Campana, G., Cuccolini, G., 2007. Laser hardening process simulation for mechanical parts, in: Lasers and Applications in Science and Engineering. p. 645404.

Tobar, M.J., Álvarez, C., Amado, J.M., Ramil, A., Saavedra, E., Yáñez, A., 2006. Laser transformation hardening of a tool steel: Simulation-based parameter optimization and experimental results. Surf. Coatings Technol. 200, 6362–6367.

Tsai, Y.L., Chen, C.C., Lan, C.W., 2010. Three-dimensional adaptive phase field modeling of directional solidification of a binary alloy: 2D--3D transitions. Int. J. Heat Mass Transf. 53, 2272–2283.

Wang, L., Felicelli, S.D., Pratt, P., 2008. Residual stresses in LENS-deposited AISI 410 stainless steel plates. Mater. Sci. Eng. A 496, 234–241.

Wang, W., Lee, P.D., Mclean, M., 2003. A model of solidification microstructures in nickel-based superalloys: predicting primary dendrite spacing selection. Acta Mater. 51, 2971–2987.

Wang, W., Luo, S., Zhu, M., 2016a. Numerical Simulation of Three-Dimensional Dendritic Growth of Alloy: Part I: Model Development and Test. Metall. Mater. Trans. A 47, 1339–1354.

Wang, W., Luo, S., Zhu, M., 2016b. Numerical Simulation of Three-Dimensional Dendritic Growth of Alloy: Part II: Model Application to Fe-0.82 WtPctC Alloy. Metall. Mater. Trans. A 47, 1355–1366.

Wei, H.L., Elmer, J.W., DebRoy, T., 2017. Three-dimensional modeling of grain structure evolution during welding of an aluminum alloy. Acta Mater. 126, 413–425.

Wen, S., Shin, Y.C., 2010. Modeling of transport phenomena during the coaxial laser direct deposition process. J. Appl. Phys. 108.

Wen, S., Shin, Y.C., 2011. Comprehensive predictive modeling and parametric analysis of multitrack direct laser deposition processes. J. Laser Appl. 23, 22003.

Wen, S., Shin, Y.C., 2013. Comprehensive predictive modeling and parametric analysis of multitrack direct laser deposition processes Comprehensive predictive modeling and parametric analysis of multitrack direct laser deposition processes. ASM Int. 022003, 1–7.

Wojnar, L., 1998. Image analysis: applications in materials engineering. Crc Press.

Yang, Y.-S., Na, S.-J., 1991. Effect of transformation plasticity on residual stress fields in laser surface hardening treatment. J. heat Treat. 9, 49–56.

Yu, F., Wei, Y., Ji, Y., Chen, L.-Q., 2018. Phase field modeling of solidification microstructure evolution during welding. J. Mater. Process. Technol. 255, 285–293.

Yuan, L., Lee, P.D., 2010. Dendritic solidification under natural and forced convection in binary alloys: 2D versus 3D simulation. Model. Simul. Mater. Sci. Eng. 18, 55008.

Zhan, H., Wang, Y., Li, C., Han, T., Han, B., Zhao, W., 2009. Computational and experimental study of a melt-hardened zone on a roller modified by wide-band laser treatment. Opt. Laser Technol. 41, 251–257.

Zhang, A., Meng, S., Guo, Z., Du, J., Wang, Q., Xiong, S., 2019. Dendritic Growth Under Natural and Forced Convection in Al-Cu Alloys: From Equiaxed to Columnar Dendrites and from 2D to 3D Phase-Field Simulations. Metall. Mater. Trans. B 1–13.

Zhang, J., Fan, Z., Wang, Y.Q., Zhou, B.L., 2001. Equilibrium pseudobinary Al--Mg2Si phase diagram. Mater. Sci. Technol. 17, 494–496.

Zhang, L., Danilova, E. V., Steinbach, I., Medvedev, D., Galenko, P.K., 2013. Diffuse-interface modeling of solute trapping in rapid solidification: Predictions of the hyperbolic phase-field model and parabolic model with finite interface dissipation. Acta Mater. 61, 4155–4168.

Zhao, J.Z., Mesplont, C., Cooman, B.C. De, 2001. Kinetics of Phase Transformations in Steels: A New Method for Analysing Dilatometric Results. ISIJ Int. 41, 492–497.

Zhao, J.Z., Mesplont, C., De Cooman, B.C., 2002. Quantitative analysis of the dilatation during an isothermal decomposition of austenites. Mater. Sci. Eng. A 332, 110–116.

Zheng, W.J., Dong, Z.B., Wei, Y.H., Song, K.J., Guo, J.L., Wang, Y., 2014. Phase field investigation of dendrite growth in the welding pool of aluminum alloy 2A14 under transient conditions. Comput. Mater. Sci. 82, 525–530.

Zhu, M., Pan, S., Sun, D., Zhao, H., 2010. Numerical simulation of microstructure evolution during alloy solidification by using cellular automaton method. ISIJ Int. 50, 1851–1858.

Zhu, M.F., Hong, C.P., 2002. A Three Dimensional Modified Cellular Automaton Model for the Prediction of Solidification Microstructures. ISIJ Int. 42, 520–526.

Zhu, M.F., Stefanescu, D.M., 2007. Virtual front tracking model for the quantitative modeling of dendritic growth in solidification of alloys. Acta Mater. 55, 1741–1755.

Zinovieva, O., Zinoviev, A., Ploshikhin, V., 2018. Three-dimensional modeling of the microstructure evolution during metal additive manufacturing. Comput. Mater. Sci. 141, 207–220.

PUBLICATIONS

Bailey, N.S., Hong, K.-M., Shin, Y.C., 2020. Comparative assessment of dendrite growth and microstructure predictions during laser welding of Al 6061 via 2D and 3D phase field models. Comput. Mater. Sci. 172, 109291.

Bailey, N.S., Katinas, C., Shin, Y.C., 2017. Laser direct deposition of AISI H13 tool steel powder with numerical modeling of solid phase transformation, hardness, and residual stresses. J. Mater. Process. Technol. 247, 223–233.

Bailey, N.S., Shin, Y.C., 2009. Optimization of laser hardening processes for industrial parts with complex geometry via predictive modeling, in: Proc. 2009 ASME Int. Manuf. Sci. & Eng. Conf., MSEC2009, 647–656.

Bailey, N.S., Tan, W., Shin, Y.C., 2015. A parametric study on laser welding of magnesium alloy AZ31 by a fiber laser. J. Manuf. Sci. Eng. 137.

Bailey, N.S., Tan, W., Shin, Y.C., 2009. Predictive modeling and experimental results for residual stresses in laser hardening of AISI 4140 steel by a high power diode laser. Surf. Coatings Technol. 203, 2003–2012.

Shin, Y.C., Bailey, N., Katinas, C., Tan, W., 2018. Predictive modeling capabilities from incident powder and laser to mechanical properties for laser directed energy deposition. Comput. Mech. 61, 617–636.

Tan, W., Bailey, N.S., Shin, Y.C., 2013. Investigation of keyhole plume and molten pool based on a three-dimensional dynamic model with sharp interface formulation. J. Phys. D. Appl. Phys. 46, 55501.

Tan, W., Bailey, N.S., Shin, Y.C., 2012. Numerical Modeling of Transport Phenomena and Dendritic Growth in Laser Spot Conduction Welding of 304 Stainless Steel. J. Manuf. Sci. Eng. 134, 41010.

Tan, W., Bailey, N.S., Shin, Y.C., 2011a. A novel integrated model combining Cellular Automata and Phase Field methods for microstructure evolution during solidification of multi-component and multi-phase alloys. Comput. Mater. Sci. 50, 2573–2585.

Tan, W., Wen, S., Bailey, N., Shin, Y.C., 2011. Multiscale Modeling of Transport Phenomena and Dendritic Growth in Laser Cladding Processes. Metall. Mater. Trans. B 42, 1306–1318.